

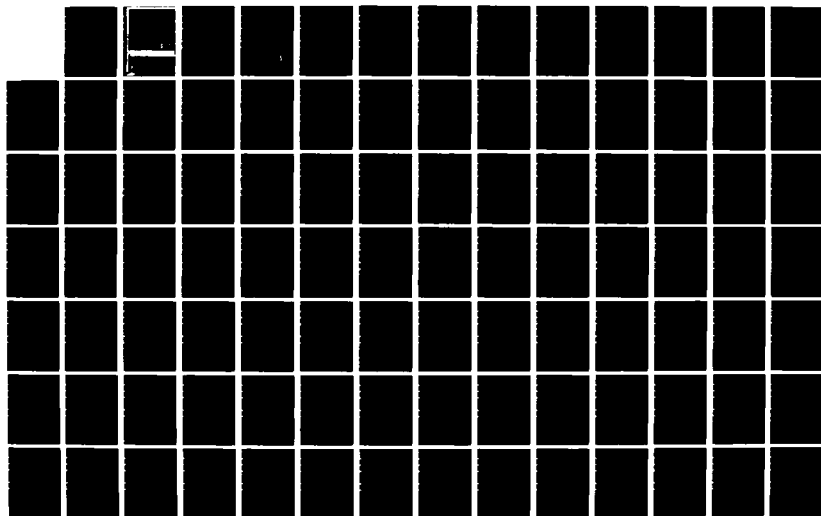
AD-A148 589

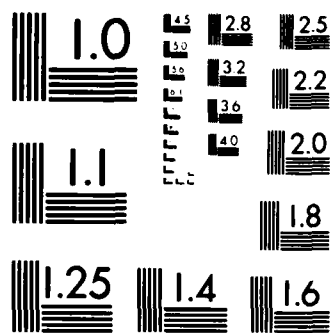
DETAILED OCEANIC CRUSTAL MODELING(U) CALIFORNIA INST OF 1/2
TECH PASADENA SEISMOLOGICAL LAB D V HELMBERGER
07 NOV 84 N00014-76-C-1070

UNCLASSIFIED

F/G 8/10

NL





MICROCOPY RESOLUTION TEST CHART
NATIONAL BUREAU OF STANDARDS 1963-A

AD-A148 589

FINAL TECHNICAL REPORT

1 February 1981 - 31 May 1984

DETAILED OCEANIC CRUSTAL MODELING

Contract No. N00014-76-C-1070

DTIC
ELECTE
DEC 14 1984
S A

CALIFORNIA INSTITUTE OF TECHNOLOGY

FINAL TECHNICAL REPORT

1 February 1981 - 31 May 1984

DETAILED OCEANIC CRUSTAL MODELING

Contract No. N00014-76-C-1070

1

FINAL TECHNICAL REPORT

1 February 1981 - 31 May 1984

Name of Contractor California Institute of Technology

Contract No: N00014-76-C-1070

Effective Date of Contract: February 1, 1981

Contract Expiration Date: May 31, 1984

Total Amount of Contract: \$240,000

Title of Work: Detailed Oceanic Crustal Modeling

Program Director: J. M. McKisic
Program Director of Ocean Acoustics Program
Scientific Office, Code 4250 A
Office of Naval Research
Arlington, VA 22217

(202) 696-4204

Principal Investigator: Donald V. Helmberger
(818) 356-6998

This document has been approved
for public release and sale; its
distribution is unlimited.

Seismological Laboratory
Division of Geological and Planetary Sciences
California Institute of Technology
Pasadena, CA 91125

DTIC
S ELE
DEC 14 1984
A

TABLE OF CONTENTS

I. Summary.....	1
II. Long Period Wave Propagation in Laterally Varying Structure.....	2
III. Upper Mantle Shear Structure Beneath the Northwest Atlantic Ocean.....	39
IV. Applications of the Transmitted Kirchhoff- Helmholtz Method to Transmitted Body Waves and Possible Structural Effects at NTS.....	82

Accession For	
NTIS GRA&I	<input checked="" type="checkbox"/>
DTIC TAB	<input type="checkbox"/>
Unannounced	<input type="checkbox"/>
Justification	<input type="checkbox"/>
<i>Letter C. J. F.</i>	
By	
Distribution/	
Availability Codes	
Dist	Avail and/or Special
<i>A</i>	



I. Summary

The research performed under this contract can be divided into 3 main topics: changes in existing methods, Cagniard de-Hoop and WKBJ, which enable construction of synthetics for mixed path situations; use of long period SH waves with source in the Northwest Atlantic and receivers on the northeast coast of North America to derive an oceanic upper mantle shear velocity model; and a technique based on evaluating the Kirchhoff-Helmholtz integral for predicting the effect of near source or near receiver structure complexity on far field p waves.

In Section II we assess the fact that recent models of upper mantle structure based on long period body waves (WWSSN) suggest large horizontal gradients, especially in shear velocities. Some changes in existing methods are required to construct synthetics for mixed path situations. This is accomplished by allowing locally dipping structure and making some modifications to generalized ray theory. Local ray parameters are expressed in terms of a global reference which allows a de-Hoop contour to be constructed for each generalized ray with the usual application of the Cagniard de-Hoop technique. Several useful approximations of ray expansions and WKBJ theory are presented. Comparisons of the synthetics produced by these two basic techniques with known solutions demonstrates their reliability and limitations.

In Section III, we have modeled the SH motion from earthquakes in the northwest Atlantic ocean to derive an oceanic upper mantle shear velocity model. The signals were recorded on long-period WWSSN and Canadian network stations on the east coast of North America. This data indicates a fast (4.75 km/sec) lid of about 100 km thickness in the older western Atlantic. Given the lid structure, the waveforms and traveltimes from the more distant data put tight constraints on the shear velocities at greater depths. The velocity below 200 km was found to be indistinguishable from a model of the East Pacific Rise (Grand and Helmberger, 1983) found using the same technique. We find the Canadian shield to be faster than both the old northwestern Atlantic and the young East Pacific Rise to about 400 km depth. No variations below 400 km are necessary to explain the data.

In Section IV, we extend the Kirchhoff-Helmholtz integral method to calculate acoustic potentials which transmit through three dimensional warped boundaries. We specify the potentials on an arbitrary surface with Snell's law and plane-wave transmission coefficients and numerically integrate their contributions at a receiver via the scalar integral representation theorem. The method is appropriate for modeling precritical transmitted potentials. Results from test models compare well with optical solutions for transmissions through a flat interface.

II. Long Period Wave Propagation in Laterally Varying Structure

Donald V. Helmberger, Gladys Engen and Steve Grand

ABSTRACT

Recent models of upper mantle structure based on long period body waves (WWSSN) suggest large horizontal gradients, especially in shear velocities. Some changes in existing methods are required to construct synthetics for mixed path situations. This is accomplished by allowing locally dipping structure and making some modifications to generalized ray theory. Local ray parameters are expressed in terms of a global reference which allows a deHoop contour to be constructed for each generalized ray with the usual application of the Cagniard-deHoop technique. Several useful approximations of ray expansions and WKBJ theory are presented. Comparisons of the synthetics produced by these two basic techniques with known solutions demonstrates their reliability and limitations.

1. Introduction

Considerable progress has been made recently in speeding-up the synthesizing of seismograms with the introduction of WKBJ and Gaussian beam methods, see Chapman (1976) and Cerveny et al. (1983). These methods have proven highly useful in generalizations to laterally varying structure, especially at high frequency, see for example Frazer and Phinney (1980). However, in the construction of longer periods (long period WWSSN seismograms) we many times are interested in more complete solutions, since the beginning portion of surface waves become important, see Grand and Helmberger (1984b). A complete set of ray parameter contributions is required to construct seismograms in this

situation. In particular, one needs to consider ray paths leaving the source horizontally, a case where the WKB method breaks down. We can avoid this problem by applying a mixture of generalized ray theory, GRT, and WKB or Disk rays as defined by Wiggins (1976).

A simple example of this procedure is given in Fig. 1 where we show schematically how to construct the step response for a smooth velocity model approximated by a stack of homogeneous layers. We suppose that a velocity model can be chosen such that the step response remains a step at all receiver positions. The simulation of this step can be achieved by summing the response from three energy paths; namely, the direct, the reflected from just below the source or reference plane, and the diving WKB contribution. All three paths contain a product of the transmission coefficients above the source. The WKB path includes the transmission coefficients across the reference plane, taken as the interface below the source. We have included a diagram of the $\Theta(t)$ vs. p curve in Fig. 1 for reference as it clearly shows that the diving path contributes little except at the larger distances. At the nearest distance, position 1, the direct ray dominates. The reflected path contributes some as critical angle is approached. At still larger distances, position 3, a head wave along the bottom of the reference interface develops followed by the critically reflected pulse. Note that the WKB path turns on at the start of the headwave. At large ranges, the WKB path becomes increasingly dominant. Note the interesting interaction of the reflected plus the direct rays where the high frequency energy turns around first. This frequency dependent behavior forces the use of Airy functions or some higher order expansion near the turning point. In practice, this step simulated by summing these three energy paths does not quite generate a step as we discuss next.

In testing the accuracy of the above procedure it is quite useful to generate the step response for models for which the answer is known. Thus, we begin with a homogeneous fluid whole space with a point source excitation yielding a step response at all positions with $1/(\text{distance})$ decay. We next impose a spherical coordinate system with many thin shells of constant velocity. Applying the classical earth-flattening approximation we obtain a model with a smooth velocity increase in depth, see Helmberger (1973). The synthetics generated in Fig. 2 are from such a model with the exact step responses indicated by the dotted lines in the bottom panel. This panel also displays the response after summing the complete set of generalized rays; direct plus rays reflected upward from all the interfaces below the source. Chapman (1976) showed that the sum of these rays should approach a step for the diving energy portion of the response as the layer thicknesses approach zero. However, the amplitude will be $(\pi/3)$ larger than the exact answer because of the neglect of multiple ray interactions with the discrete layering. The GRT response at the largest distance shows the most roughness for times near the direct arrival when the interaction with the reflection from just below the source is the most severe. Similar complexity occurs with the hybrid method except that the diving energy is smoother with WKBJ. Short period synthetics generated from these step responses become quite dirty and simple geometric ray theory yields cleaner results. However, for long period studies the advantage of being able to include the radiation pattern appropriate for earthquake sources, or shear dislocations, far outweighs the disadvantage of the noise generated by the hybrid method. For example, consider the SH-radiation from a dip-slip event where the up-going radiation has opposite polarity from the down-going energy, see Helmberger (1973). In short, the sum as displayed in Fig. 2 becomes more interesting when the direct ray trace has opposite sign from the other two.

We could probably improve the response at the time the three energy paths interface the most vigorously by including a few more GR's and/or by lowering the reference boundary for the WKBJ contribution. However, we are particularly interested in more realistic earth models with a crust-over-mantle structure where the moho or low velocity zone serve as natural reference boundaries. Thus, we propose using GR's to compute the start of the Love waves, and WKBJ to generate the responses returning from deeper structure. This approach proved effective in studying the structure and evolution of the lithosphere for an old oceanic plate, Grand and Helmberger (1984b). It would be advantageous to treat the obvious lateral variation encountered in such studies. Although the real world is truly three dimensional in nature, some useful progress can be made by examining profiles of data along paths of symmetry where two-dimensional idealizations are appropriate. We will address such models in this paper.

Our strategy is similar to Wiggins (1976) in that we will use a combination of GRT and DRT to generate synthetics and justify the latter by demonstrated accuracy.

Review of Ray interactions with nonplanar structure

Boundary value problems involving complicated geometry have a long rather unrewarding history; thus, we will jump directly to approximate solutions and test their validity against finite-difference calculations and other more well known results. Before addressing the dipping layer problem it is instructive to examine the flat-layered case and emphasize the geometric interpretation of generalized ray theory. This proves particularly useful for constructing generalizations to more complicated situations since the most progress in understanding these problems is at high frequency. Both line and point sources will be

discussed since the former is easier to understand theoretically but the latter is necessary for studying the Earth.

Line source and Planar Model

The solution of the scalar wave equation assuming line source excitation for generalized rays as given by Gilbert and Knopoff (1961) is

$$\Phi_L(r, z, t) = H(t - t_0) / (t^2 - t_0^2)^{1/2} \quad (1)$$

where $t_0 = R / \alpha$, $R^2 = z^2 + r^2$, and α = velocity.

Φ_L is defined as the displacement potential with the index L used to remind ourselves of the line excitation. A high frequency approximation of (1) is

$$\Phi_L \propto H(t - t_0) / (t - t_0)^{1/2} \sqrt{R} \quad (2)$$

and the motion decays with distance as the \sqrt{R} . The solution to the interface problem setup displayed in Fig. 3a is

$$\Phi_L(r, z, t) = \text{Im} \left(\frac{1}{\eta_1} \frac{dp}{dt} T(p) \right) \quad (3)$$

where

$$t = p(d_1 + d_2) + h_1 \eta_1 + h_2 \eta_2 \quad (4)$$

$$\eta_i = \left(\frac{1}{\alpha_i^2} - p^2 \right)^{1/2}$$

$T(p)$ = Transmission coefficient

The symbol (Im) indicates the imaginary part of the complex product of the functions of ray parameter, see Helmberger (1983) for example. The ray parameter appropriate for the direct arrival path, p_0 , can be obtained by

$$\frac{dt}{dp}(p_o) = 0, \text{ and } d_1 - \frac{h_1 p_o}{\eta_1} = d_2 - \frac{h_2 p_o}{\eta_2} \quad (5)$$

But with

$$p_o = \frac{\sin \theta_1}{\alpha_1} = \frac{\sin \theta_2}{\alpha_2} \quad (6)$$

and, therefore,

$$\eta_1 = \frac{\cos \theta_1}{\alpha_1}, \eta_2 = \frac{\cos \theta_2}{\alpha_2}$$

we see that the ray goes from the source to the receiver. And

$$t_o = \left[\frac{\sin \theta_1}{\alpha_1} d_1 + \frac{\cos \theta_1}{\alpha_1} h_1 \right] + \left[\frac{\sin \theta_2}{\alpha_2} d_2 + \frac{\cos \theta_2}{\alpha_2} h_2 \right] \quad (7)$$

$$t_o = R_1 / \alpha_1 + R_2 / \alpha_2$$

For times greater than t_o , we must solve t for complex p such that the imaginary parts of $p d_1$ and $\eta_1 h_1$ cancel, etc.

The behavior near p_o can be approximated by noting that

$$t = t_o + \frac{dt}{dp}(p - p_o) + \frac{d^2 t}{dp^2}(p - p_o)^2 / 2$$

and solving for

$$(p - p_o)^2 = 2(t - t_o) / \left(\frac{d^2 t}{dp^2} \right)$$

Thus,

$$\frac{dp}{dt} = (t - t_o)^{-1/2} / \left(2 \frac{d^2 t}{dp^2} \right)^{1/2} \quad (8)$$

Note that from (4)

$$\frac{d^2 t}{dp^2} = \frac{-h_1}{\eta_1^3 \alpha_1^2} - \frac{h_2}{\eta_2^3 \alpha_2^2} \quad (9)$$

It is convenient to condense the various factors containing p_0 into

$$S_L(p_0) \equiv \frac{1}{\left| \frac{d^2 t}{dp^2} \right|^{1/2} \sqrt{\alpha_1} \eta_1} \quad (10)$$

which we call the spreading factor. Thus,

$$S_L = \left[\frac{h_1}{\eta_1 \alpha_1} + \frac{h_2}{\eta_2 \alpha_2} \left(\frac{\eta_1^2 \alpha_1}{\eta_2^2 \alpha_2} \right) \right]^{-1/2} \quad (11)$$

We note that by differentiating Snell's law we obtain

$$\frac{\cos \theta_1}{\alpha_1} d\theta_1 = \frac{\cos \theta_2}{\alpha_2} d\theta_2$$

Substituting this expression into S_L we obtain

$$S_L = \frac{\sqrt{d\theta_1}}{\left[R_1 d\theta_1 + R_2 d\theta_2 \frac{\cos \theta_1}{\cos \theta_2} \right]^{1/2}} \quad (12)$$

If $R_2 = 0$, we obtain the whole space spreading again where $(R_1 d\theta_1)$ is just the width of the ray tube described in Fig. 3a. A correction for the change in direction is required as the tube crosses the interface, namely

$$(\cos \theta_1 / \cos \theta_2)$$

Thus, the denominator of (12) is again the width of the ray tube at the receiver, L_θ in Fig. 3a. Substituting into (3) we obtain

$$\Phi_L \propto S_L H(t-t_0) \text{Re}(T(p_0)) / (t-t_0)^{1/2} \quad (13)$$

where R_0 indicates the real part operator.

Point source and Planar Model

The point source solution for the same problem setup, Fig. 3b, is

$$\phi_p(r, z, t) = \sqrt{\frac{2}{r}} \frac{1}{\pi} \left[\frac{1}{\sqrt{t}} * \text{Im} \left[T(p) \frac{\sqrt{p}}{\eta_1} \frac{dp}{dt} \right] \right] \quad (14)$$

and applying the same first motion approximation we obtain a slightly more complicated spreading factor namely,

$$S_p \approx \sqrt{\frac{p}{r}} \frac{1}{\eta_1} \left| \frac{d^2 t}{dp^2} \right|^{-1/2} \quad (15)$$

$$= \left[\frac{R_1 \sin \theta_1 + R_2 \sin \theta_2}{\sin \theta_1} \right]^{-1/2} S_L \quad (16)$$

and note that by letting $R_2 = 0$ we obtain

$$S_p = 1/R \quad (17)$$

In terms of area, we note that

$$S_p = \left[\frac{\sin \theta_1 d\theta_1 d\phi}{(R_1 \sin \theta_1 d\phi + R_2 \sin \theta_2 d\phi)(R_1 d\theta_1 + R_2 d\theta_2 \frac{\cos \theta_1}{\cos \theta_2})} \right]^{1/2} \quad (18)$$

which can be interpreted as the incremental element of area at the source divided by the projected area at the receiver or simply,

$$S_p = \left[\frac{A_o}{A} \right]^{1/2} \quad (19)$$

Thus, the first motion behavior becomes

$$\begin{aligned}\phi_p(\tau_1 t_1 t) &= \frac{1}{\pi} \left[\frac{1}{\sqrt{t}} * \frac{1}{\sqrt{t-t_0}} \right] S_p \text{Re}(T(p_0)) \\ &= S_p H(t-t_0) \text{Re}(T(p_0))\end{aligned}\quad (20)$$

More complicated solutions to multi-layered models in terms of ray summations will be discussed later.

Locally Dipping Structure

Although GRT for parallel interfaces has been well developed the modifications for nonplanar structure or smoothly varying interfaces has not. Some of the difficulties encountered for the simple wedge problem have been discussed by Hudson (1963). Hong and Helmberger (1977) constructed a solution in terms of generalized rays for this problem and defined a method of ray path construction compatible with the usual Cagniard-de Hoop formalism. We will consider the direct arrival interacting with two dipping interfaces as an example application. The problem setup is displayed in Figure 4a with the response given by

$$\phi_L = \text{Im} \left[T_{12}(p_1) T_{23}(p_2) \frac{1}{\eta_1} \frac{dp}{dt} \right] \quad (21)$$

where p_1 and p_2 are defined by the local ray parameter, namely

$$p_1 = \frac{\sin \theta_1}{\alpha_1}, \quad p_2 = \frac{\sin \theta_2}{\alpha_2}$$

and are no longer equal. However,

$$\frac{\sin \theta_1}{\alpha_1} = \frac{\sin \theta_2}{\alpha_2}$$

where

$$\Theta_2' = \Theta_2 + \Theta_s$$

with Θ_s defining the change of the slope of interface (1) relative to the previous reference at Θ_1 . Performing the derivatives discussed in the previous section we obtain

$$S_L(p_o) = \frac{\sqrt{d\Theta_1}}{\left[R_1 d\Theta_1 + R_2 d\Theta_2 \frac{\cos\Theta_1}{\cos\Theta_2'} + R_3 d\Theta_3 \frac{\cos\Theta_2 \cos\Theta_1}{\cos\Theta_2' \cos\Theta_2} \right]^{1/2}}$$

which is similar to (12) and has the same interpretation. The travel time is defined by

$$t = \sum_{i=1}^3 (p_i d_i + \eta_i h_i) \quad (22)$$

with the definitions of d_i and h_i given in Fig. 4a as the projection of the geometric path onto the local Cartesian coordinates. The arrival time can be determined as before with

$$\frac{dt}{dp_m} = 0$$

defining

$$p_1 = p_{o_1}, p_2 = p_{o_2},$$

etc. Thus,

$$d_m - h_m \frac{p_m}{\eta_m} = 0 \quad (23)$$

with

$$p_m = \frac{\sin \theta_m}{\alpha_m} \text{ and } \eta_m = \frac{\cos \theta_m}{\alpha_m}$$

and the $\frac{dt}{dp_m} = 0$ condition leads to a ray going from the source to the receiver.

The first-motion approximation becomes

$$\Phi_L \propto \text{Re}(T_{12}(p_{01})T_{23}(p_{02})) \frac{H(t-t_0)}{(t-t_0)^{1/2}} S_L \quad (24)$$

Spreading for the point source solution becomes slightly more complicated than in the flat case, but allowing

$$\sqrt{\frac{\tau}{p}} = \left(\sum_{i=1}^3 \frac{d_i}{p_i} \right)^{1/2} \quad (25)$$

results in S_p defined by

$$S_p = \sqrt{\frac{p}{r}} \frac{1}{\eta_1} \left| \frac{d^2 t}{dp^2} \right|^{-1/2} \quad (26)$$

reducing to

$$= (A_0 / A)^{1/2},$$

at the direct arrival time. The details of this result have been given previously by Hong and Helmberger (1978). Thus, the point source solution for the geometry given in Fig. 4b becomes

$$\Phi_p = \frac{1}{\pi} \left[\frac{1}{\sqrt{t}} * dm \left[\pi(p) \frac{1}{\eta_1} \frac{dp}{dt} \left(\sum \left(\frac{d_i}{p_i} \right) \right)^{-1/2} \right] \right] \quad (27)$$

where

$$I(p) = T_{12}(p_1) T_{23}(p_2)$$

Numerical evaluation of (27) yields the geometric result but, also, retains longer period information since (dp/dt) can be evaluated along the deHoop contour in the usual manner.

Many layers, WKB, and Radiation patterns

Following the results of the previous section, and inserting the radiation pattern for the simple SH motions from a dislocation source, see Helmberger and Malone (1975) the displacements can be written

$$v(r, z, \theta, t) = \frac{M_0}{4\pi\rho_0} \left(\frac{\Delta}{\sin\Delta} \right)^{1/2} \frac{d}{dt} \left[\dot{D}(t) * \sum_{j=1}^2 A_j(\theta, \lambda, \delta) V_j(t) \right] \quad (28)$$

where

$$V_j(t) = \sqrt{\frac{2}{r\pi}} \left[\frac{1}{\sqrt{t}} * \psi_j(t) \right] \quad (29)$$

and

$$\psi_j(t) = \sum_{i=1}^n SH_j(p) \frac{\sqrt{p}}{\eta_\beta} (2p) C_s \frac{dp}{dt} \Pi_i(p) \quad (30)$$

and the summation of n rays is required. The various symbols are defined below:

$v(r, z, \theta, t)$ = displacement on free surface

M_0 = moment

ρ_0 = density

$D(t)$ = dislocation history

$\dot{D}(t)$ = far-field time function

$A_1(\theta, \lambda, \delta) = \cos 2\theta \cos \lambda \sin \delta - 1/2 \sin 2\theta \sin \lambda \sin 2\delta,$

$A_2(\theta, \lambda, \delta) = -\sin \theta \cos \lambda \cos \delta - \cos \theta \sin \lambda \cos 2\delta,$

θ = strike from the end of the fault plane

λ = rake angle

δ = dip angle

r = distance between source and receiver

p = ray parameter

$$\eta = \left(\frac{1}{\beta^2} - p^2 \right)^{1/2}$$

Δ = epicentral distance in radians

$$\left(\frac{\Delta}{\sin \Delta} \right)^{1/2} = \text{correction for earth flattening}$$

β = shear velocity

and where the vertical radiation patterns are given by

$$SH_1 = \frac{1}{\beta^2} ,$$

$$SH_2 = \frac{\varepsilon}{\beta^2} \frac{\eta}{p} , \quad \varepsilon = \begin{matrix} +1 & z > h \\ -1 & z < h \end{matrix}$$

$$\eta = \left(\frac{1}{\beta^2} - p^2 \right)^{1/2}$$

The correction for point source spreading is defined by

$$C_s = \sqrt{\frac{\tau}{p}} \left(\sum \frac{d_i}{p_i} \right)^{-1/2} \quad (31)$$

This solution is similar to the flat case and we can, obviously, construct the diving ray response for a smoothly varying structure by summing the primary rays as discussed in Fig. 2. We can then use this result to check the disk ray solution which can be obtained by replacing (30) by

$$\Psi_j = SH_j(p) \frac{\sqrt{p}}{\eta_\beta(p)} \sum (\delta p / \delta t) \quad (32)$$

where the sum is taken over the $p(t)$ curve as described by Wiggins (1976).

For a simple turning ray problem

$$\left| \frac{\delta p}{\delta t} \right| = \frac{1}{|r - r(p)|} \quad (33)$$

where $r(p)$ is distance reached by a ray defined by p , see Fig. 5. Substituting (33) into (32) and evaluating (29) yields a simple step response, as discussed by Chapman (1976). Essentially, (33) has a simple square-root singularity at $r = r(p)$, and rays that hit the surface near the receiver dominate the behavior. Since p varies along the path, we must define which p to use in the evaluation of (32). The proper choice is the starting p at the source as outlined in the previous section. Note that for the case of an up-going direct ray the two methods can be interpreted in a similar manner. Only one ray is involved in both, and applying the first-motion approximation of (30) yields (32) where the extra (2) is produced by the double valued nature of expression (33). Thus, the application of WKB theory to the locally dipping problem appears to be essentially the same as for the uniform layered problem. We trace the ray through a stack of layers down to the turning region, turn it around analytically, and follow it to the surface obeying Snell's law. The special treatment at the turning point removes the nonlinear ray parameter effects of the homogeneous layered parameterization as is well known. The C_s factor can be assumed to be one for most applications of gentle dipping structure, as discussed in the next section and was omitted from (32).

The approach followed here is similar to that followed by Wiggins (1976) in that the main justification for expression (33) is that it yields results comparable to GRT. A theoretical justification of applying WKB to laterally varying structure is given by Chapman and Drummond (1982).

3. Applications

In this section we will briefly outline possible applications of these approximate solutions to seismological problems. First, the direct or up-going energy problem is discussed when motions in the sloping layers of a sedimentary basin are excited by a line-source. In this form Finite Difference calculations can be used to check the accuracy of the GRT results. Next, the point source excitation of Love waves is considered in the presence of sloping structure followed by models of growing Lithosphere. Finally, we construct synthetics for laterally varying upper mantle models and confirm the usefulness of WKBJ at long periods.

Local seismograms

One of many complexities associated with strong motion seismology is the noticeably long duration of high frequency P-waves observed in sedimentary basins. These waves are generally polarized onto the vertical component due to the strong velocity gradients near the surface. The latter portion of these observed motions are generally depleted at lower frequency. Thus, one might conclude that there are propagational waveguides that preferentially prolong high frequency motions. Non-planar surface layering appears to have this property. This calculation will be done with SH-waves since this type of motion is studied throughout the remainder of this paper, but we would expect that P-waves would behave in a similar manner.

A single low velocity layer which grows with distance between the source and receiver is assumed with a line source of SH motion situated at a depth of 5.5 km. The response build-up as a function of the number of multiples is displayed in Fig. 6. The square-root singularity indicated in expression (13) is apparent for the direct arrival. Note that after one bounce the reflection from

the lower interface becomes complex because of the local ray parameter effect and a head wave and post-critical angle reflection develops. After two bounces, the time separation between the head wave onset and reflection times becomes less and the reflected spike increases in strength. After many bounces the ray can no longer reach critical angle and still fit into the waveguide. Thus, $(R)^n$ becomes small since the reflection coefficient (R) becomes less than one. The drop-off in amplitude of the multiples occurs abruptly at this time on the record.

The corresponding point source response displayed in Fig. 7 can be obtained from expression (29). Neglecting the C_s factor produces a similar response with a slight reduction in later arrivals, roughly 13% for the last arrival. Thus, point source amplitudes can be approximated quite well by scaling line source results by the square-root of the distance factor similar to the flat case. Note that the Cagniard-de Hoop technique proves particularly useful in tracing these rays and evaluating their individual contributions. However, as mentioned earlier, this series of rays does not necessarily converge to the exact solution and some demonstration of accuracy is required. This was attempted earlier by Hong and Helmberger (1976) but not very convincingly. A much more rigorous comparison is presently being conducted by Vidale et al (1984) with respect to using line-source numerics to construct point-source synthetics. Preliminary results of the comparison of the two techniques for this single model is displayed in Fig. 8. The top trace is the broadband result displayed in Fig. 6., with a filtered response in the middle for comparison with finite-difference results on the bottom. The highest frequencies have been removed in this comparison due to computational expense but the existence of strong high frequency multiples is striking. Since the finite-difference calculation can be performed on any arbitrary two-dimensional structure we have extended the thin layer directly above

the source to the left as a flat thin layer avoiding the wedge effect which is obviously omitted in the ray solution. Comparison with and without the wedge and many other complexities involving double-couple solutions constructed by line-to-point source operators are discussed in Vidale et al (1984). We will suppose throughout the remainder of this paper that the generalized ray modifications discussed in the previous section are sufficiently accurate to test the WKBJ synthetics.

Love waves at Regional Distances

Another interesting application of the above technique is in the development of Love waves and the effects of traveling across oceanic-to-continental transitions. This problem was encountered in a recent paper by Grand and Helmberger (1984b) when the so-called G-phase, the name applied to the impulsive Love waves associated with oceanic paths, interferes with mantle arrivals. Apparently, this situation occurs for well developed Lithospheres associated with older plates over-lying slower upper-mantle velocity models. The beginning portions of the G-phase as recorded slightly inland develop longer periods than observed at Island stations. Their period and arrival times are compatible with the model presented in Fig. 9a. A dipping model with arrival times compatible with the flat model is presented in Fig. 9b along with the comparison of step responses given on the right. Note that the first 30 sec of motion are nearly identical. The higher frequency portions of the Love wave become less pronounced in the dipping case but the general appearance is similar to the pure-oceanic case, see Grand and Helmberger (1984b).

It appears that as the Lithosphere ages it gets thicker, for example, see Forsyth (1975). A preliminary model of predicted Love waves for this situation is given in Fig. 10, also included are synthetics for a fast and slow mantle. The long

period nature of the synthetics from the dipping model is similar to the slow model as we might expect. However, there is considerable roughness at the start of the Love waves caused by the mixed paths involving both the crust and lid.

Observationally, we see upper-mantle arrivals starting near these ranges. Thus, the diving energy must be added to these synthetics following the strategy discussed earlier. This can be accomplished by summing GR's or by applying WKBJ.

Upper-mantle models

In this section we investigate effects of lateral variation in upper mantle models, as displayed in Fig. 11. We have chosen a particularly simple case with no low velocity zone to simplify the comparison of GRT with WKBJ synthetics. A further simplification is made by allowing the two models to be connected in a linear fashion as displayed in the middle column.

Following the WKBJ approach we first illuminate the model by tracking a set of rays from the source towards prospective receivers. These rays reach the surface at $r(p)$ in time $T(p)$. The travel time at a particular receiver, r , can be written $t(p) = p r + T(p) - p r(p)$. Note that p changes in each layer but they are all functions of the beginning p . Thus, we can construct the t versus p curves as displayed in Fig. 12 for reversed profiles. The largest ray parameter, p_{max} , is .26 which corresponds to the crustal velocity of 3.9. Next, we perform the numerical derivative $(\delta p / \delta t)$ of these curves. Note that there will be a large truncation phase at the near stations at p_{max} . This can be avoided by including the product of the transmission coefficients, TC's, across the Moho, the reference interface discussed earlier, since $TC(p_{max})$ is small. Thus, the product of the TC's with $(\delta p / \delta t)$ has a relatively smooth behavior. The head wave along the

Moho is added in by including the reflected generalized ray. By performing the convolution indicated in expression (29) we derive step responses from (t vs. p) curves displayed in Fig. 12. These results are shown in Fig. 13. Short period synthetics are included to emphasize the rapid decay of amplitude at the triplication tips. Eliminating the truncation phase discussed here can also be achieved by a modification of the Gaussian beam technique as developed by Madariaga and Papadimitriou (1984).

The synthetics at the smallest ranges are completely controlled by the shallow structure and the local model. Thus, the first arrival from the Fast-to-Slow synthetics have a shorter travel time which causes the triplication from the 400 km discontinuity to arrive later than in the reverse profile.

A more detailed plot of the Slow-to-Fast profile is displayed in Fig. 14 along with the GRT responses for comparison. The synthetics are appropriate for the WSSN long period system. A typical strike-slip source was assumed with a triangular time history of (1, 1, 1 secs) and a $t^* = 3$, see Grand and Helmberger (1984a).

Note that there is a distinct change in the latter portion of the WKB step responses between 17 and 18°. This is caused by omitting the head waves from along the top of the model for distances beyond 17°. However, no apparent change in the synthetics occurs at this range suggesting that the long period drift is outside the pass-band of the operators used in generating these synthetics. The high-frequency spikes so apparent in the GRT step responses are likewise removed by the convolution operators.

The 400 km discontinuity is treated slightly differently in the two methods which leads to some shifts in the triplication position. In GRT, the 400 km discontinuity is generally treated as a sharp jump in velocity since this leads to the best results when compared against reflectivity, see Burdick and Orcutt

(1978). On the other hand, WKB requires a smooth transition, 3 km transition in this particular case, such that the (p vs. t) curve is smooth. Thus, the sharp spikes occurring in the GRT step responses near 14° are precritical angle reflections from the 400 km discontinuity. Similarly, the triplication seems to extend to greater distances in the GRT results. Note that the most severe mismatch occurs near this range. At larger ranges the two methods agree quite well, especially the synthetic waveforms. In fact, the synthetic waveforms agree at all distances with the maximum deviation in amplitude of about 25%. And, since these synthetic waveforms are used to interpret observations which can seldom be modeled as well as the agreement between these two methods, we can consider the WKB modifications successful. For more precision involving sharp boundaries we suggest breaking the p integration into a combination of WKB for the smooth portion of the model and a generalized ray for the reflecting interface, for example see Given (1984).

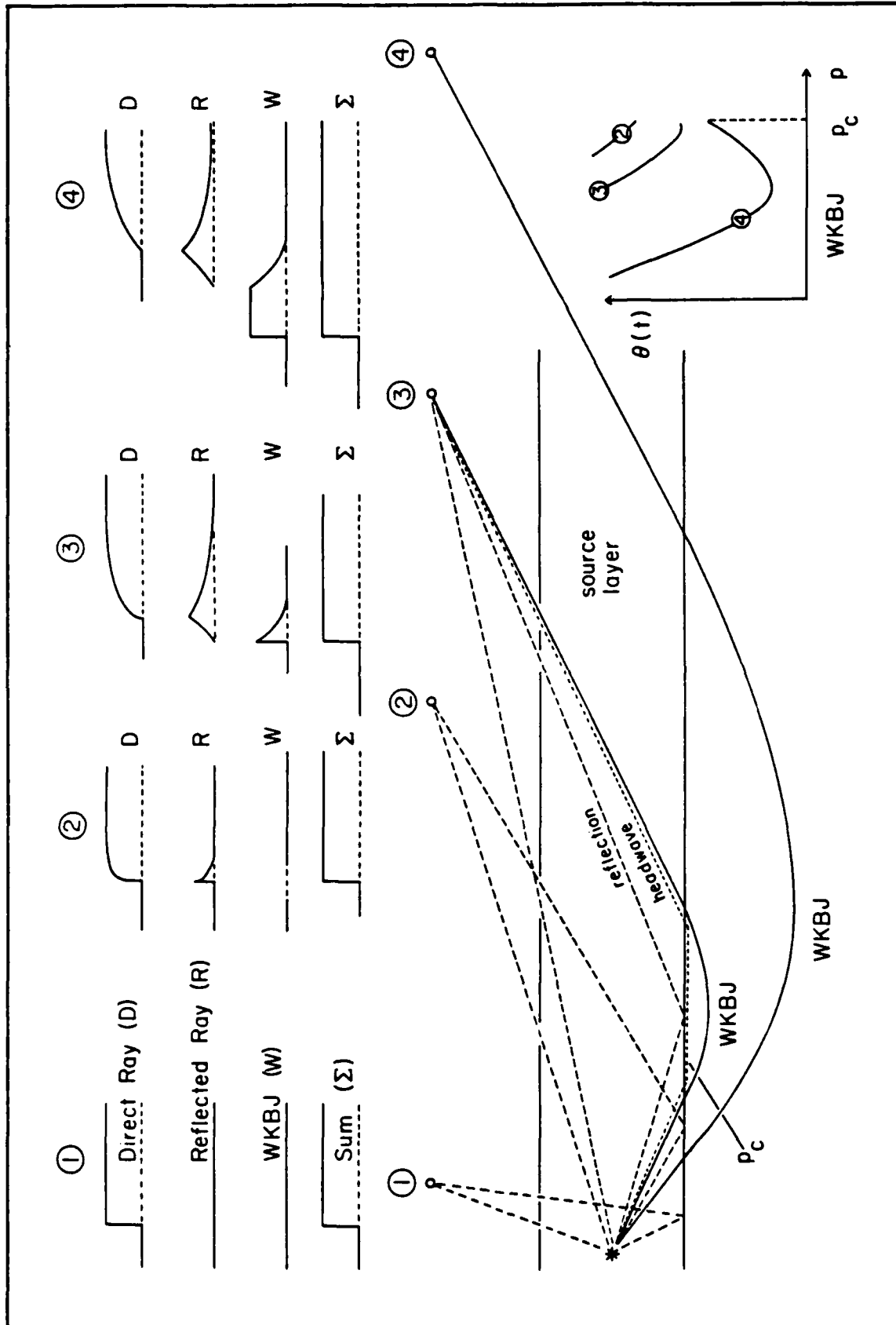
Conclusions

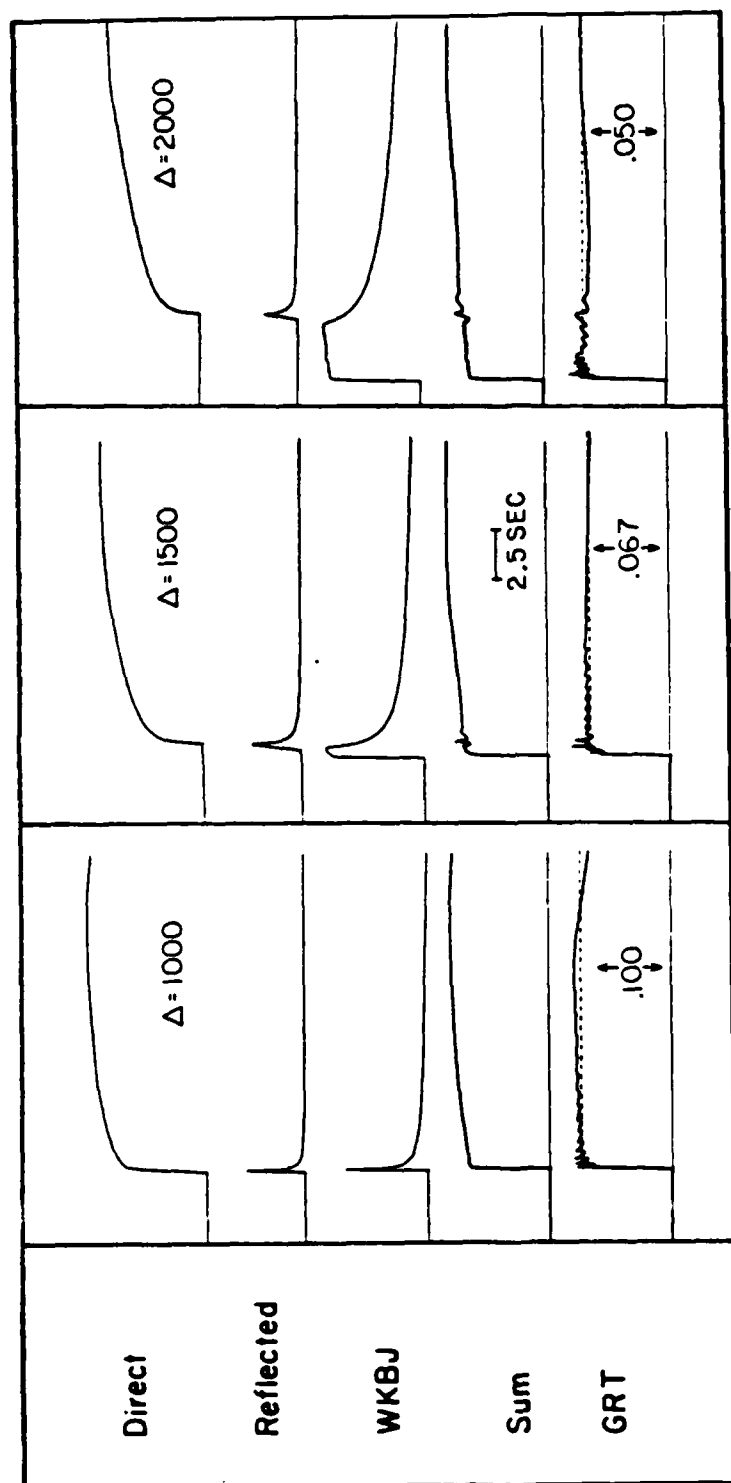
In this paper we presented a hybrid procedure of generating complete seismograms in laterally varying structure by applying a mixture of GRT and DRT. First, we reviewed the modifications of GRT required for dipping structure in terms of local coordinates and ray parameter concepts for line and point source theory. Solutions calculated by this approach not only agree with geometric results, but also agree with longer period motions such as computed with finite-difference methods. Using the correspondence between GRT and DRT, disk ray theory, we can express the latter in relatively simple form, essentially applying a square-root of distance correction to line source spreading. Comparisons between GRT and DRT synthetics of diving energy paths agree reasonably well. Thus, we can construct nearly complete seismograms with a

combination of GRT and DRT with the former used to handle the shallow structure. Some useful demonstrations of the methods are given for crustal and upper-mantle models.

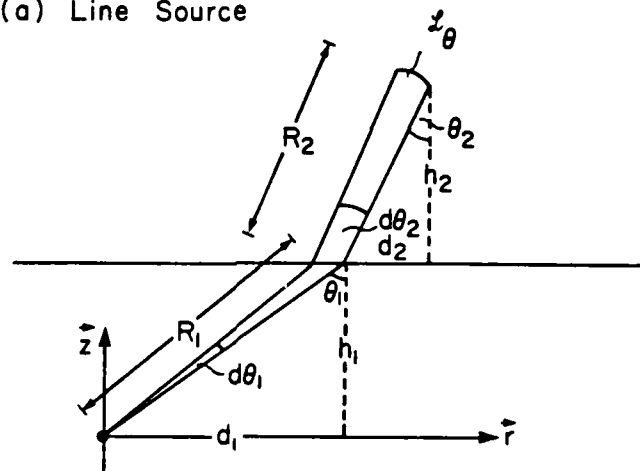
Acknowledgements

This work was supported in part by Office of Naval Research Contract 14-76-C-1070 and by National Science Foundation Grant EAR811-6023. Contribution 4155, Division of Geological and Planetary Sciences, California Institute of Technology, Pasadena, California 91125.

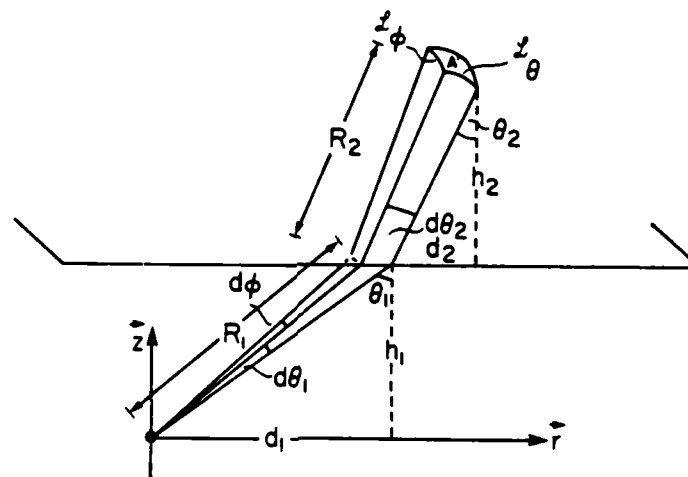




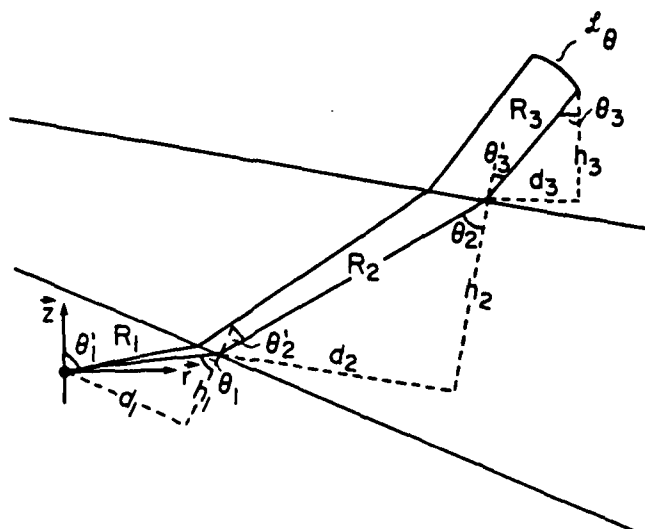
(a) Line Source



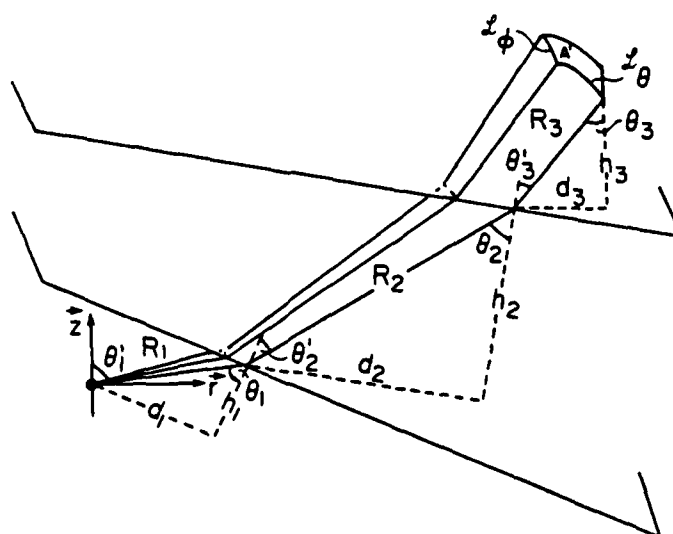
(b) Point Source

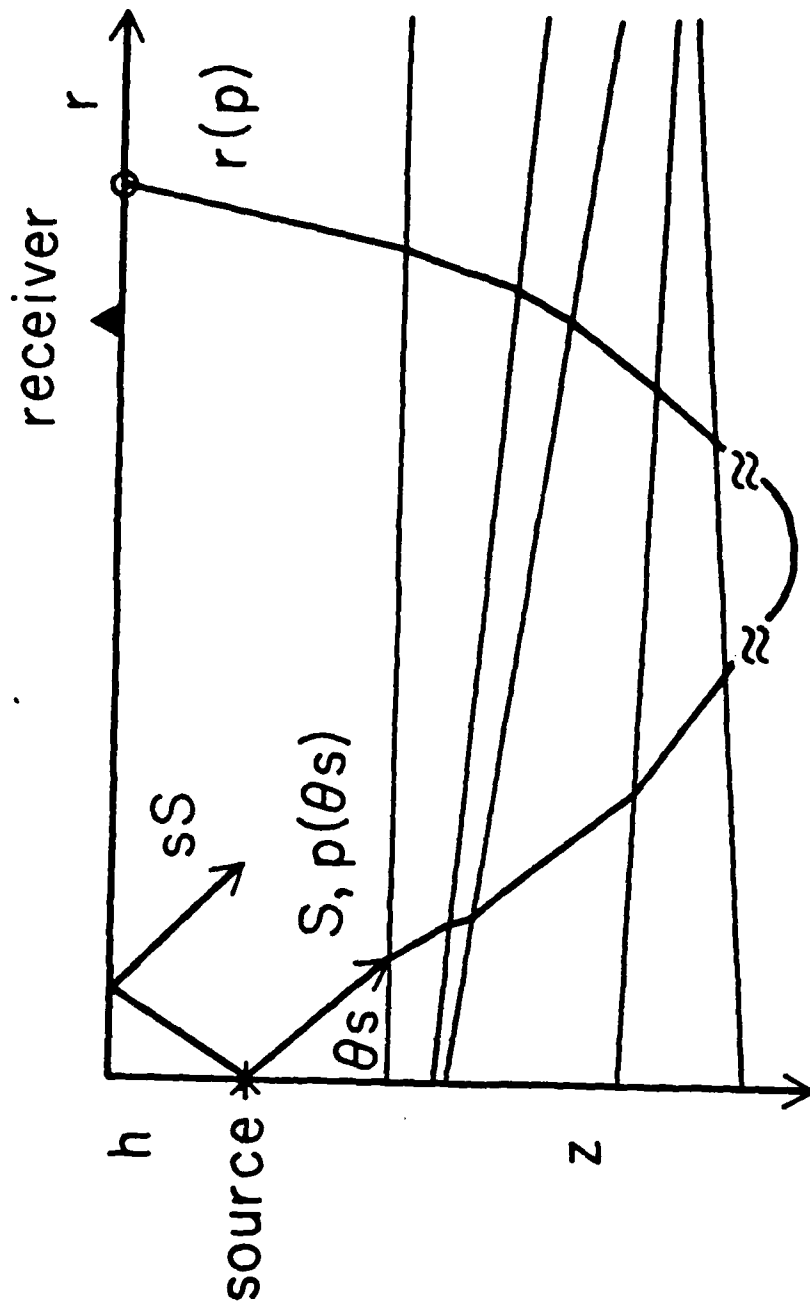


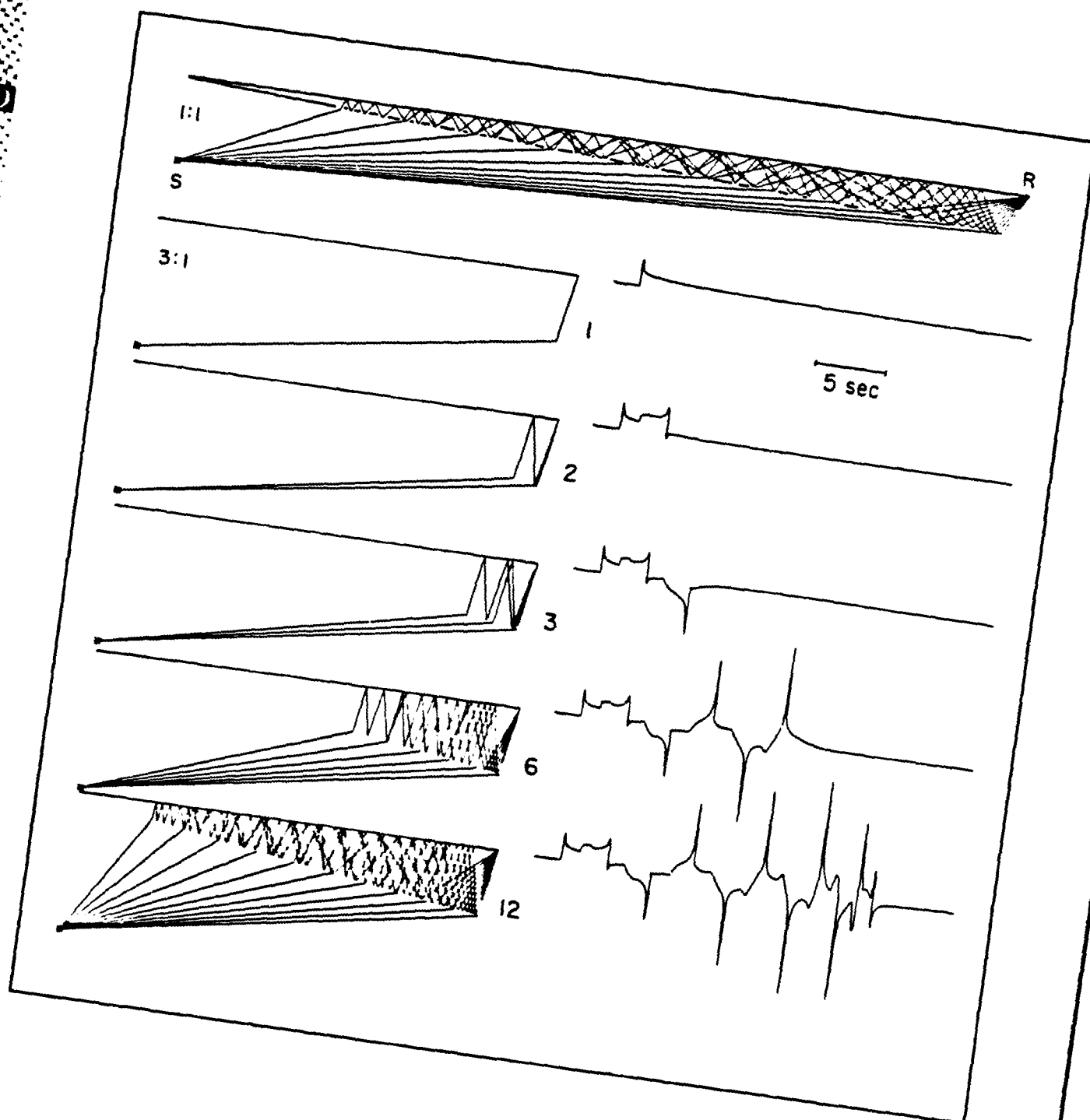
(a) Line Source

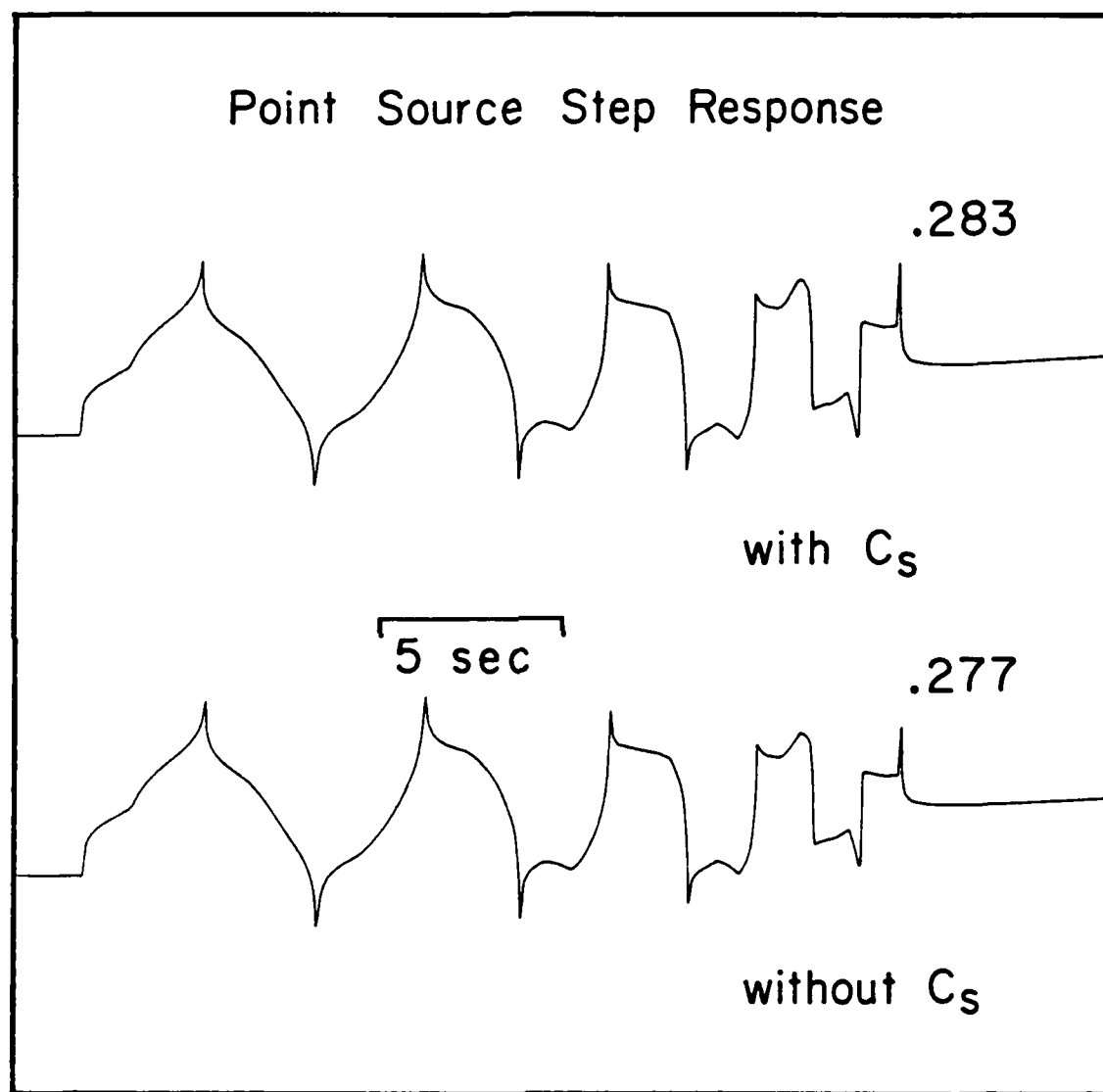


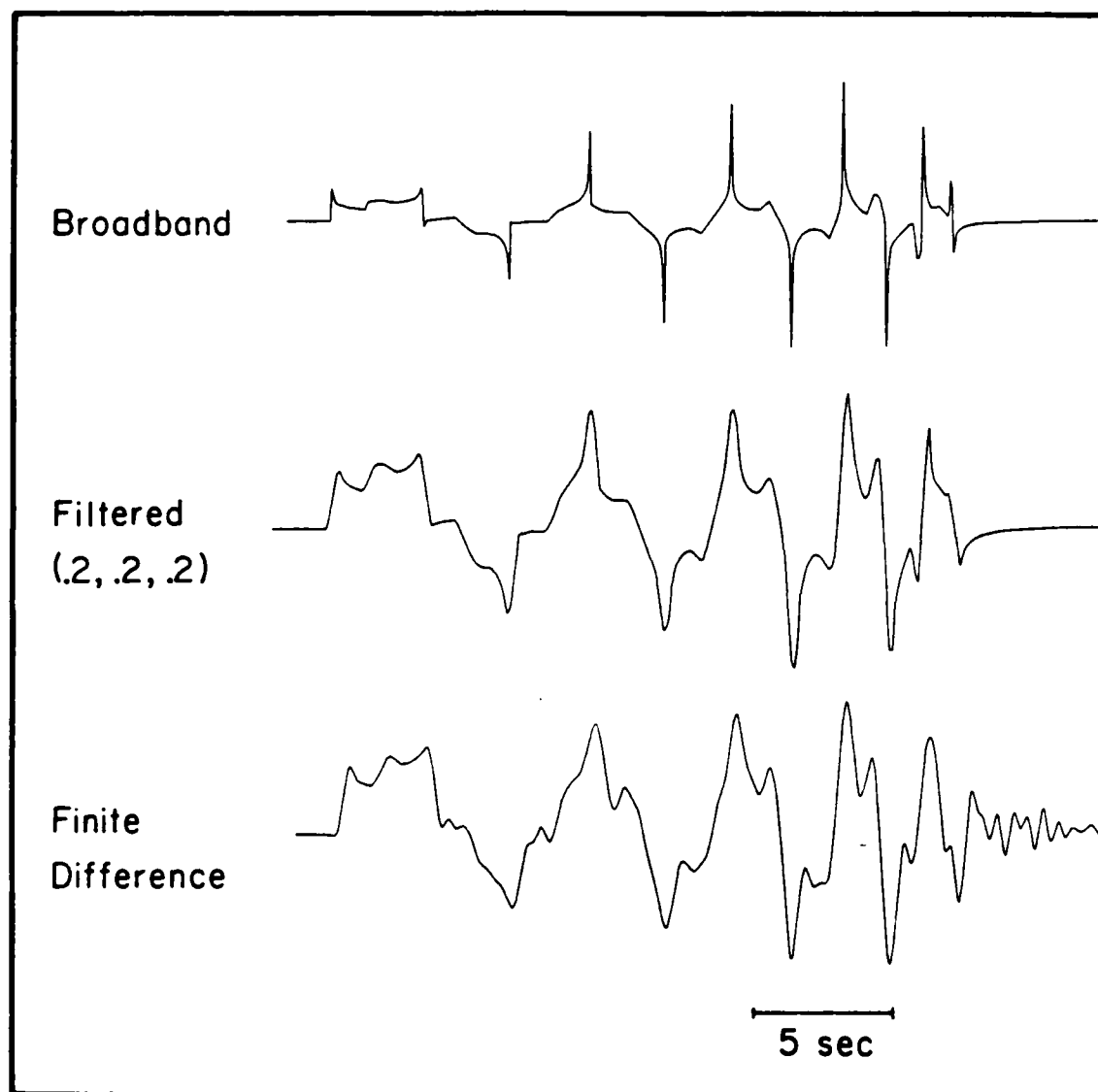
(b) Point Source

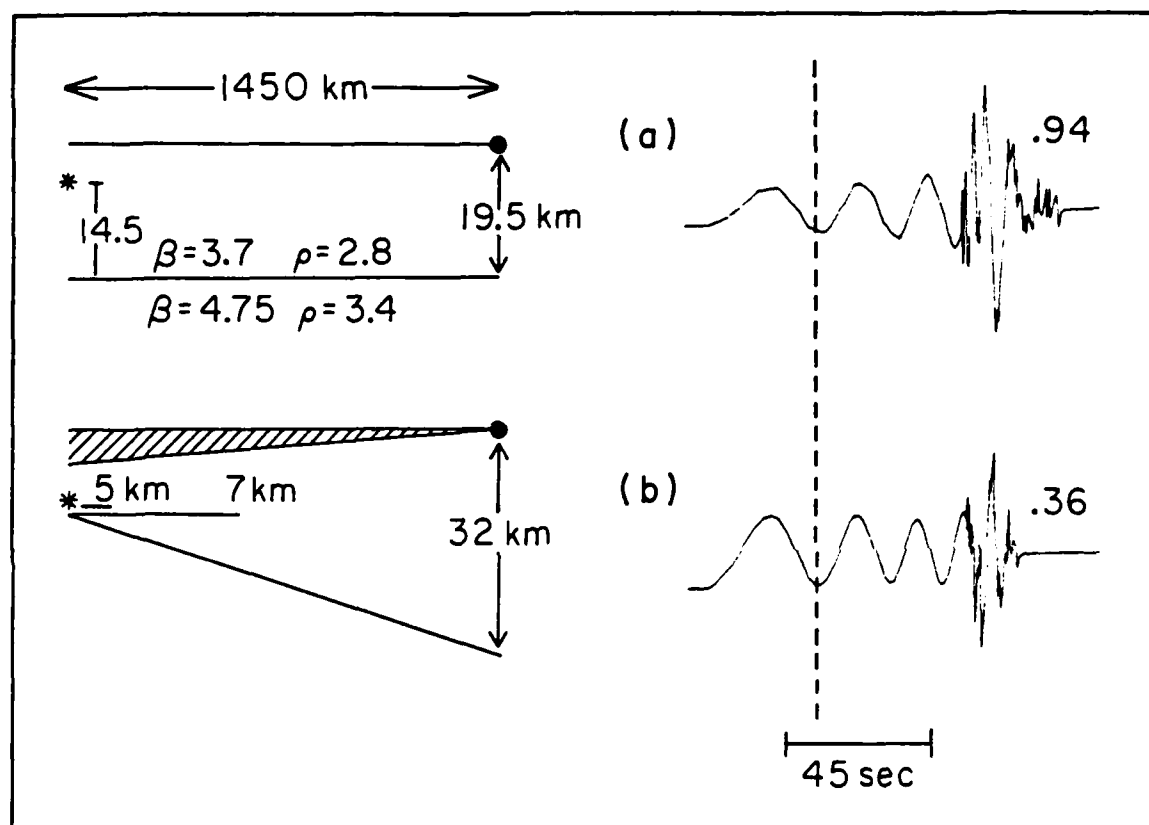


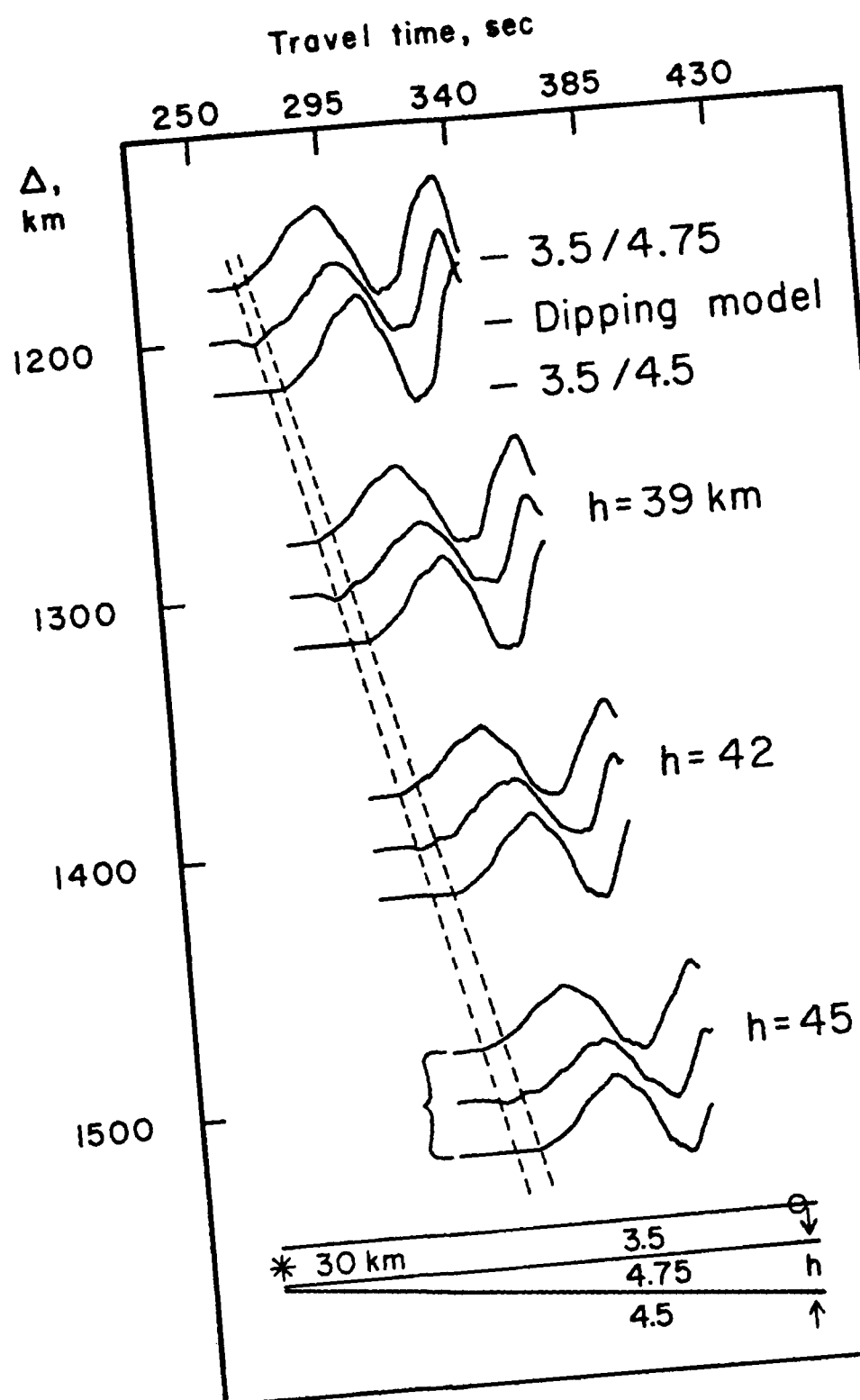


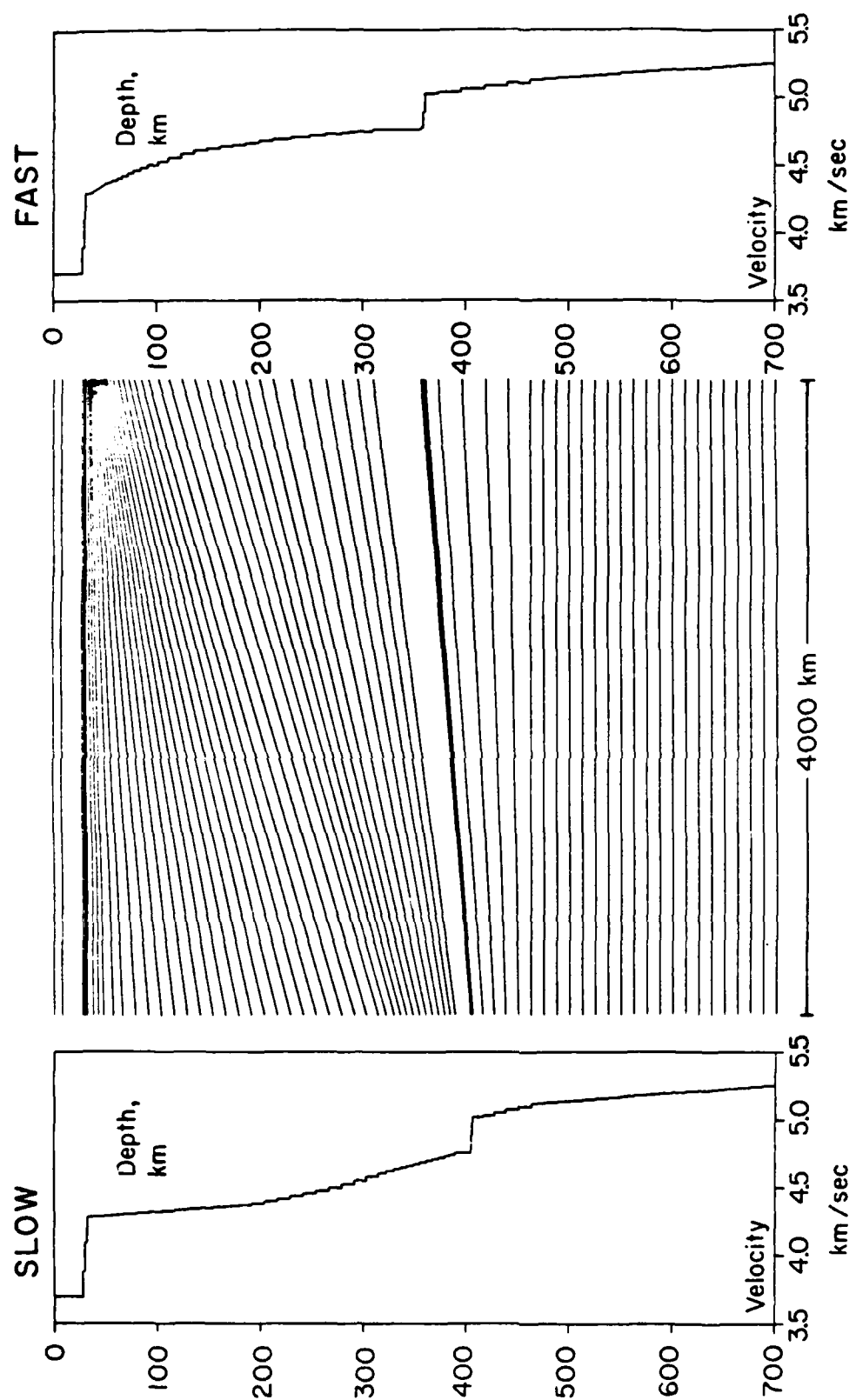




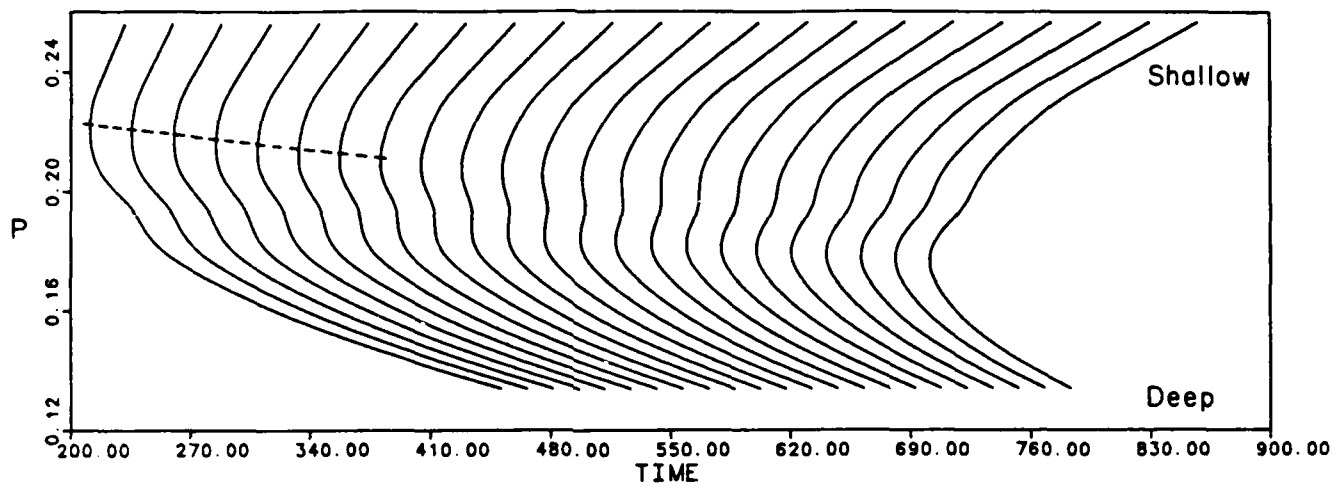




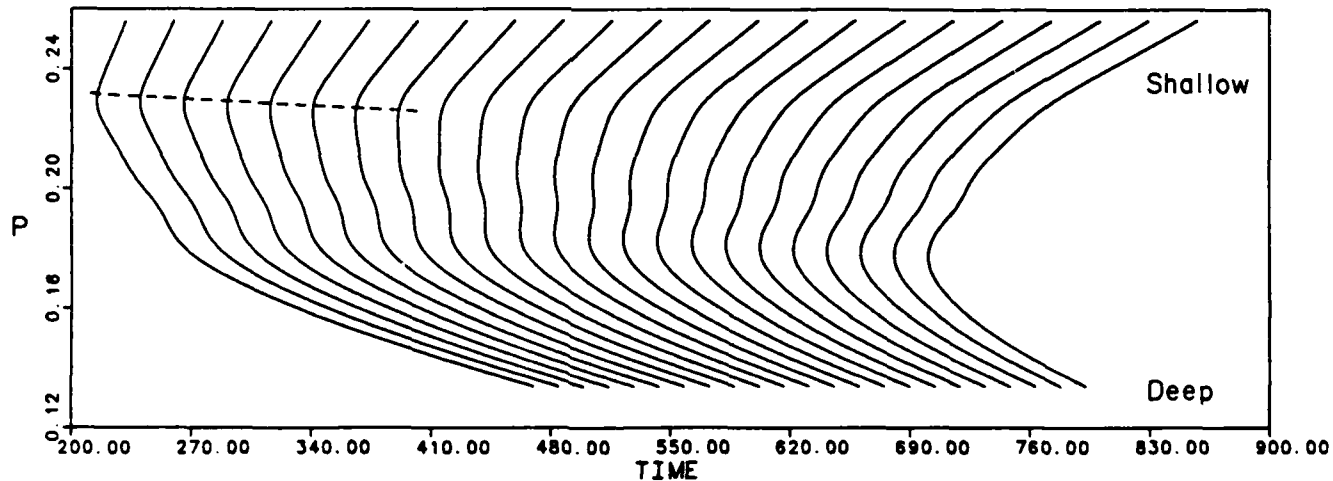


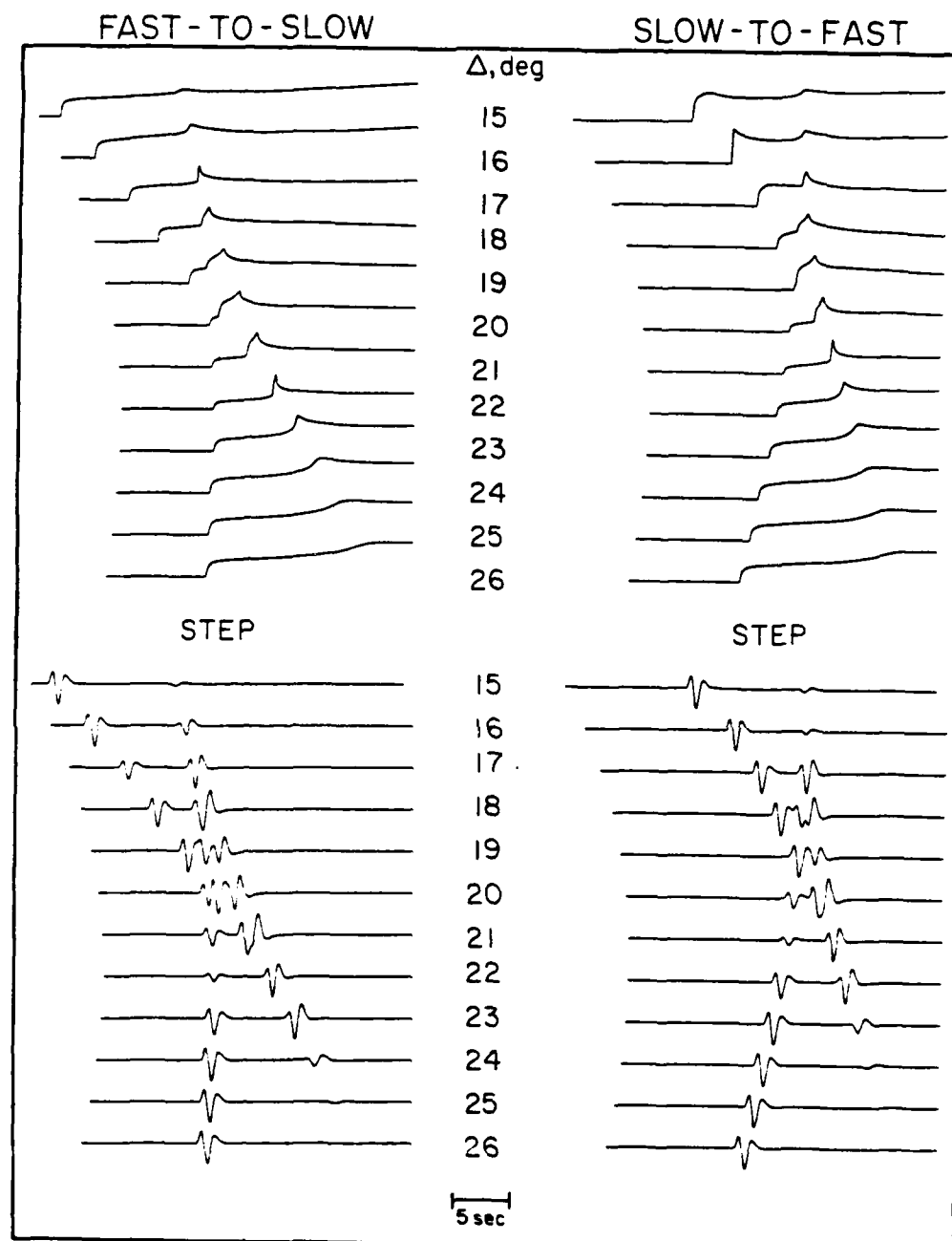


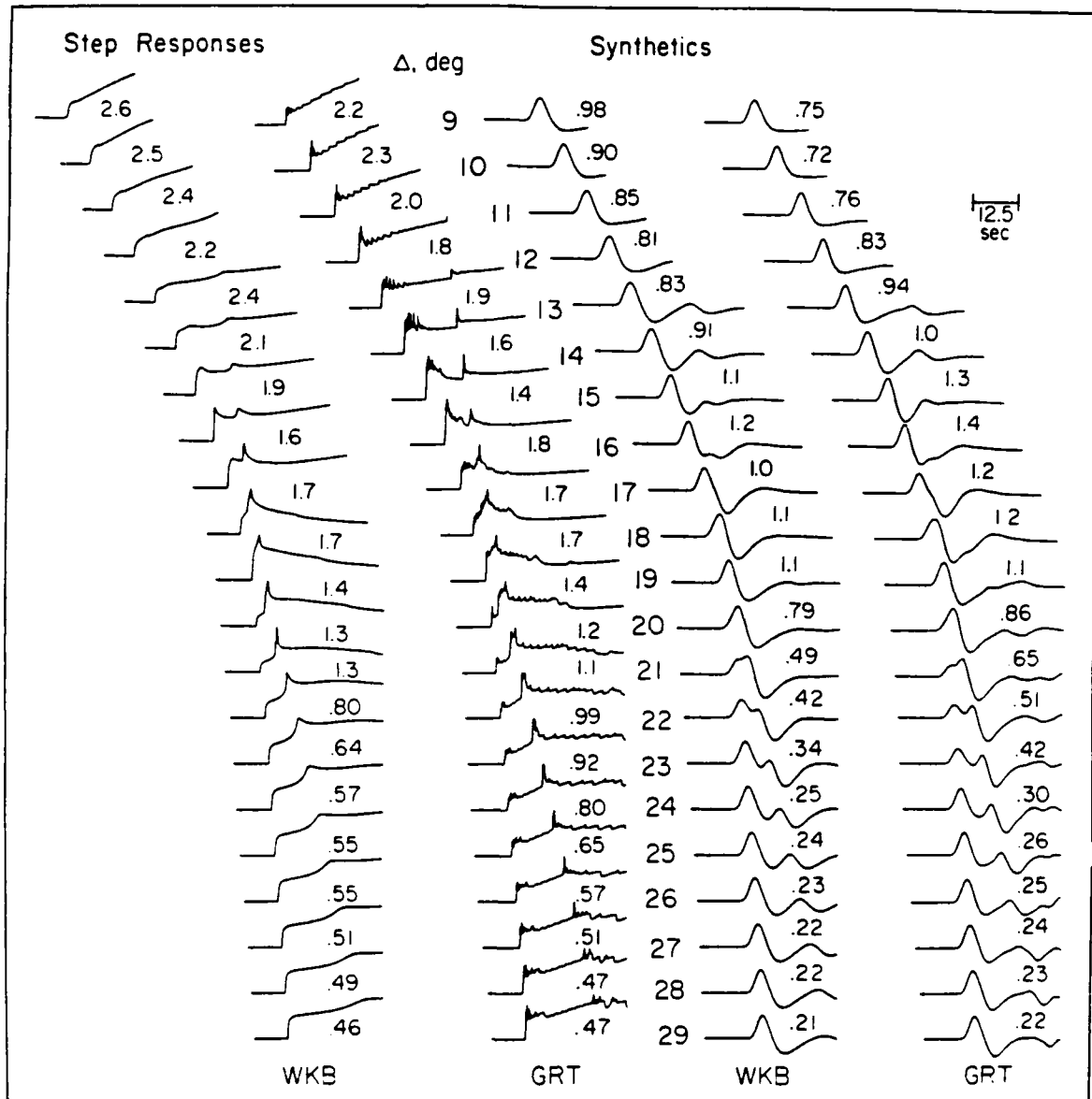
FAST - TO - SLOW



SLOW - TO - FAST







References

- Burdick, L. J., J. A. Orcutt (1979). A comparison of the generalized ray and reflectivity methods of waveform synthesis, *Geophys. J.*, 58, 261.
- Cerveny, V., M. M. Popov and I. Psencik (1982). Computation of seismic wave fields in inhomogeneous media, Gaussian beam approach, *Geophys. J.*, 70, 109-128.
- Chapman, C. H. (1976). A first-motion alternative to geometrical ray theory, *Geophys. Res. Letts.*, 3, 153-156.
- Chapman, C. H. and R. Drummond (1982). Body-wave seismograms in inhomogeneous media using Maslov Asymptotic Theory, *BSSA*, 72, 277-318.
- Forsyth, D. W. (1975). The early structural evolution and anisotropy of the oceanic upper-mantle, *Geophys. J., R. astr. Soc.*, 43, 103-162.
- Frazer, L. N. and R. A. Phinney (1980). The theory of finite frequency synthetic seismograms in inhomogeneous elastic media, *Geophys. J., R. astr. Soc.*, 63, 691-717.
- Gilbert, F. and L. Knopott (1981). The directivity problem for a buried line source, *Geophysics*, 26, 626-634.
- Given, J. (1984). Inversion of body-wave seismograms for upper mantle structure. Ph.D. Thesis, California Institute of Technology, Pasadena, California 91125.
- Grand, S. P. and D. V. Helmberger (1984a). Upper mantle shear structure of North America, *Geophys. J., R. astr. Soc.*, 76, 399-438.
- Grand, S. P. and D. V. Helmberger (1984b). Upper mantle shear structure beneath the northwest Atlantic Ocean, *J. Geoph. Res.*, in press.
- Helmberger, D. V. (1973). Numerical seismograms of long-period body waves from seventeen to forty degrees, *BSSA*, 63, 633-646.
- Helmberger, D. V. (1983). Theory and Application of Synthetic Seismograms. Proceedings of the International School of Physics, Course LXXXV, edited by H. Kanamori and E. Baschi, North Holland press.
- Helmberger, D. and S. Malone (1975). Modeling local earthquakes as shear dislocations in a layered half space, *J. Geoph. Res.*, 80, 4881-4888.
- Hong, T. L. and D. V. Helmberger (1977). Generalized ray theory for dipping structure, *BSSA*, 67, 995-1008.
- Hong, T. L. and D. V. Helmberger (1978). Glorified optics and wave propagation in nonplanar structure, *BSSA*, 68, 1313-1330.
- Hudson, J. A. (1963). SH waves in a wedged-shaped medium, *Geophys. J., R. astr. Soc.*, 7, 517-546.

- Madariaga, R. and P. Papadimitriou (1984). Gaussian Beam Modeling of Upper Mantle Phases, submitted to *Anales Geophysicae*.
- Vidale, J., D. V. Helmberger and R. W. Clayton (1984). Finite-Difference Seismogram for SH-waves, to be submitted to BSSA.
- Wiggins, R. A. (1976). Body wave amplitude calculations, II, *Geophys. J. R. astr. Soc.*, 46, 1-10.

III. Upper Mantle Shear Structure Beneath the Northwest Atlantic

Stephen P. Grand and Donald V. Helmberger

Abstract

We have modeled the SH motion from earthquakes in the northwest Atlantic ocean to derive an oceanic upper mantle shear velocity model. The signals were recorded on long-period WWSSN and Canadian network stations on the east coast of North America. The travel times and waveforms of seismograms, in the distance range 11° to 16° , were used to constrain the lid structure. This data indicates a fast (4.75 km/sec) lid of about 100 km thickness in the older western Atlantic. From 16° to 28° the S waves pass through triplications due to velocity jumps near 400 km and 660 km. The branches from both discontinuities are visible in the S wave data. These arrivals were modeled using synthetic seismograms to obtain accurate travel times. The two triplications are also apparent in SS data from 30° to 50° . The triplication curves derived from the S waves agree with the SS data. Given the lid structure, the waveforms and traveltimes from the more distant data put tight constraints on the shear velocities at greater depths. The velocity below 200 km was found to be indistinguishable from a model of the East Pacific Rise (Grand and Helmberger, 1983) found using the same technique. This is in contrast to the Canadian shield model found in the same paper. We find the Canadian shield to be faster than both the old northwestern Atlantic and the young East Pacific Rise to about 400 km depth. No variations below 400 km are necessary to explain the data.

Introduction

Upper mantle shear velocity has been shown in numerous studies to vary significantly under different tectonic provinces. The sensitivity of shear velocity to temperature makes the study of lateral variation in shear structure an important tool in determining the thermal state of the earth. There has been debate, however, on the depth extent of shear heterogeneity between different tectonic regimes. Jordan (1981) has proposed that old cratons have deep roots, from 400 km to 650 km in depth. This idea is based largely on the differences in time of ScS multiples in different regions (Sipkin and Jordan 1976, 1980). Anderson (1979), on the contrary, states that continental roots extend no deeper than about 150 km to 200 km. Okal and Anderson (1975) and Anderson (1979) claim that the ScS data and surface wave data are incompatible with the 'deep root' hypothesis of Jordan. It will take detailed studies of the upper mantle beneath several cratons and many oceanic areas before generalizations about the deep structure of continents and oceans can be stated with certainty.

Grand and Helmberger (1983), paper 1, studied the upper mantle under North America and part of the East Pacific Rise using S and SS bodywave phases in the distance range 10° to 60° . They showed that using the travel-times and waveforms of S and SS one could constrain the shear structure to 800 km depth with a resolution of about 1% over

100 km. This technique provides better resolution, at depth, than conventional surface wave dispersion studies due to the fact that the wavelengths of energy sampling deeper structure do not increase substantially. In this paper we have studied the western part of the North Atlantic ocean using essentially the same technique of modeling S and SS phases. The area studied has oceanic crust ranging in age from 0 to 150 m.y. (Sclater & Parsons, 1981). Thus we have an opportunity to compare the upper mantle structure of an active ridge, old ocean, tectonic continent and stable craton derived from a single method.

The data from the Atlantic ocean show features very similar to the data from the East Pacific Rise and the Canadian shield. Discontinuities near 400 km and 660 km produce triplication branches which are visible in both the S and SS waves. Using the times from these branches we have derived an average model for the older part of the Atlantic (70 to 150 m.y.) near North America. The model, listed in table 1, and shown in figure 1 with the previously derived models from paper 1, has a high velocity lid about 100 km thick. Below the lid, the velocity decreases to 200 km depth at which depth it has the same velocity as that derived for the East Pacific Rise in paper 1. Below 200 km we find no difference in structure between the old Atlantic and the young East Pacific regions.

Technique

To determine the upper mantle shear velocity beneath the Atlantic, we modeled the SH motion from Atlantic earthquakes recorded on long period WWSSN (World Wide Standard Seismic Network) and CSN (Canadian Seismic Network) stations in eastern North America. The approach is to match the travel times and waveforms of nearin data, using synthetic seismograms, to constrain the shallow structure. As one looks at seismograms at further distances, deeper structure is sampled. Using synthetic seismograms we can analyze what from depth individual arrivals come and thus, adjust the model appropriately when discrepancies between the synthetics and data appear. The starting model was taken as the East Pacific Rise model (TNA) found in paper 1. Changes to it were made from the top downward until the Atlantic data was satisfied. The resolution of this trial and error approach was investigated by Given (1983). He developed a formal inversion for structure, using S wave travel times and waveforms, and applied it to data from the East Pacific Rise and western North America. The resulting model was very similar to TNA, which was derived by a trial and error technique thus we feel confident in the conclusions of our modeling.

The earthquakes used are listed in table 2. Figure 2 shows the locations of the events and stations relative to oceanic crustal age (Jordan 1981). The events were selected on the basis of the quality of

the SH signals from them. The stations used were nearly naturally rotated and thus data with strong SV energy was apparent. Due to the problem of shear-coupled PL interference, discussed in Helmberger & Engen (1974), we rejected any station which had a high SV to SH ratio at the arrival time of S or SS. The events on the Mid-Atlantic Ridge had teleseismic SH waves similar to those from strike-slip earthquakes, thus we assumed the mechanism to be strike-slip for them. Event 1, near Bermuda, was studied by Stewart and Helmberger (1981), and event 2, by Molnar and Sykes (1967). The focal mechanisms of the two events were thrust but they still produced simple SH waves to some stations.

The data fall in the range 11° to 52° and sample ocean of varying age. From 11° to 30° , the S waves travel wholly in the upper mantle and the triplications are obvious in the data. Data at these distances came from events 1 and 2, and, as can be seen on the map, their paths were totally in ocean older than 100 m. y.. Data from 27° to 52° came from the events near the Mid-Atlantic Ridge. We used the SS waveforms and SS-S times at these ranges to determine the structure. SS goes through the same triplication as S at nearer distances as discussed in paper 1. These earthquakes are in much younger ocean than those used for S, however, their midpoints are all within ocean older than 100 m. y.. Using SS-S times should decrease the contamination of the data by the initial propagation through younger structure.

To derive an upper mantle structure which would reproduce the

relatively complicated seismograms used, we constructed synthetic seismograms. Synthetics enable one to model interfering signals and, also, to intuitively understand them. The procedure used to calculate the synthetics is well established. One assumes a seismogram consists of a series of linear operators representing the different factors in a record (Helmberger & Burdick, 1978). We can write a seismogram $Y(t)$ as

$$Y(t) = S(t) * I(t) * A(t) * M(t)$$

where $S(t)$ is the source, $I(t)$ is the instrument response, $A(t)$ is an attenuation operator and $M(t)$ is the Green's function for wave propagation through the mantle.

The source function was constructed by fitting the teleseismic S waveforms. A trapezoidal time function was convolved with an operator representing the S, sS interaction, dependent on focal mechanism (Langston & Helmberger, 1975). The depth and time function are adjusted to fit the teleseismic data. All the events used in this study are shallow and produced simple teleseismic SH waves. The details of the source are not too important as the arrivals we modeled are generally well separated.

The attenuation operator was taken from Futterman (1962) and Carpenter (1965). The amount of attenuation is parameterized by the value of t^* , the travel-time divided by the average Q along the ray path. It is generally believed that Q is lower in the upper few hundred

km than below. For this reason, we attenuated SS arrivals more than S arrivals. A t^* of 4 was used for S and a t^* of 7 for SS waves. These values are rather arbitrary but are fairly close to values computed from published Q models such as PREM (Dzeiwonski & Anderson, 1981). Improvements in Q structure will help the synthetic to data amplitude fits but should not affect the relative timings of different arrivals significantly.

The Green's functions, for upper mantle propagation, were computed using two techniques. Preliminary modeling of the data was done using the WKBJ method of Chapman (1978) and Wiggins (1976). This method is very inexpensive and useful in the modeling process. There are situations, however, where it does a poor job, such as energy from shadow zones and interactions with sharp discontinuities. Therefore, after deriving a model fitting the traveltimes of the most obvious arrivals with the WKBJ synthetics, we used a Cagniard-de Hoop code (Helmberger, 1973) to model, in more detail, our data. Comparisons of synthetics by the two methods are given in paper 1 for two upper mantle models.

The Cagniard-de Hoop synthetic is generated by adding the responses of generalized rays through a stack of homogeneous layers. A limitation of the technique is that for SS, or other multiple bounce phases, a large number of rays are needed to compute the response. At different distances we empirically found which rays were necessary by progressively adding more rays until the synthetics did not change

appreciably. The rays used in different situations will be mentioned in the following. Comparisons of Cagniard-de Hoop with the reflectivity method (Burdick & Orcutt, 1978) have been positive and thus we feel this approach is valid.

Lid Structure

To investigate the upper mantle below 200 km a good estimate of the upper 200 km is necessary since all the data used to look at deeper structure will be contaminated by the more shallow structure. The upper part of the model was found by fitting the traveltimes and waveforms of the SH motion at closein distances (11° to 16°). For a continental structure, at these ranges, there are well separated arrivals from the mantle. Depending on the structure, they can be from above or below the lid. These separate arrivals (S,SS,SSS etc.) were modeled in paper 1 to determine the average shallow structure beneath the Canadian shield and western North America. The reason the arrivals are well separated at these ranges is due to the thick crust above the mantle. Each time a phase comes to the surface it must travel through the much slower crust and, thus, multiple bounce phases, such as SS and SSS, fall rapidly behind the direct arrival S wave. In an oceanic structure the crust is much thinner and thus the separation of multiple bounce arrivals is much

less in time. In figure 3 we illustrate this effect using the Cagniard-de Hoop generalized ray technique. We show the effect of adding successive multi-bounce arrivals for two simple structures. To represent an oceanic structure, we used a 7 km thick layer of velocity 3.7 km/sec over a half-space with velocity 4.75 km/sec. The continental synthetics are for a 30 km layer, of velocity 3.7 km/sec over the same half-space. The rays used are shown to the left of the synthetic step responses. The seismograms are calculated at a distance of 8° . The front of the records are due to multiple bounce head waves while the high frequency later arrivals are reflections. Each multiple bounce ray is very similar in the two structures, however, the difference in crustal thickness changes the time separation of the arrivals and, thus, the interference. This produces the vastly different dispersion in the two structures. The final panel is the response after convolving with a long-period WSSN instrument and a 6 sec trapezoidal time function. Obviously, the oceanic data, at nearin distances, will have a very different appearance than the continental data just due to the crust. Large sets of multiply reflected crustal rays must be used to model oceanic records at upper mantle distances. In terms of modes, this can be understood by the fact that the fundamental Love mode, from 20 to 60 sec travels at mantle velocities and not crustal velocities, as in the continent. This phenomena was pointed out by Thatcher and Brune (1969) in their discussion of the interference of higher mode Love waves with the fundamental at periods less than 60 sec for oceans.

Inspite of the fact that we cannot model nearin data as distinct

mantle arrivals, the waveforms still contain much information. Figure 4 illustrates how we might use data at nearin distances, say 12° . Figure 4a shows the effect of changing crustal thickness. The synthetics were computed summing rays with up to 40 multiples in the crustal layer. A strike-slip source is at 5 km depth. With changing crustal thickness the arrival time of the first downswing stays the same. This is basically headwave energy with only a few free surface reflections. The later swings, in the waveform, change dramatically with crustal thickness differences of only a few kilometers. The signal is higher frequency with thinner crust due to the fact that the later arrivals in the wavetrain have bounced many times in the crust. Changing the crustal thickness changes the time separation of the multiply reflected arrivals and this becomes more important in the back of the waveform where the reflections are more numerous. Changing crustal velocity will have the same effect. A slower crust would be equivalent to a thicker crust.

Figure 4b shows the effect of changing lid velocity but keeping the crust constant. The waveforms are not changed significantly but the absolute travel-time changes by 12 sec with a change in lid velocity from 4.6 km/sec to 4.8 km/sec. In figure 4c we have added a further variation by putting a lower velocity half-space below the lid. In this case, all the crustal reverberations were used along with rays which have reflected from the bottom of the lid up to 4 times. The reflection coefficient at the lid half-space boundary is the opposite sign of that at the crust lid boundary. Thus, for a thin lid, the lid rays cancel

the front of the waveform. The thicker lids have little effect at 12° because the rays arriving at the station from deeper depths are steeper and thus the reflection coefficients are fairly small. The thicker lids will affect the Love wave at further distances.

We approached the data at nearin distances in the following way. First, the crustal thickness was adjusted to match in time the successive peaks and troughs in the wavetrain. The crustal velocity was kept fixed at 3.7 km/sec. Next the lid velocity was modified to match the absolute travel-time of the first downswing. There is some tradeoff here between the lid thickness and the lid velocity. However, as can be seen in figure 4, there is a difference between a high velocity thin lid and a low velocity thicker lid. The separation of the first two downswings is different in the two cases since lid velocity basically shifts the whole waveform but lid thickness controls only the front of the signal. The lid models found in this way are obviously very crude but they should constrain the main features of the very shallow mantle and allow us to investigate deeper structure.

Figure 5 shows the two nearest seismograms used in the study. The later arrivals at BEC were too large to recover. These seismograms both recorded almost pure SH motion with paths totally in ocean older than 100 m. y.. The dispersion of the signal at SJG required a crustal thickness of 9.5 km. This is thicker than normal oceanic crust, though it could be that we used too high a crustal velocity. A low velocity, low Q layer at the surface would decrease the amplitude of the back of

the wavegroup, since the signal there is due to more surface reflections than the front. It would also decrease the average crustal velocity. Officer et al. (1952) report an average 2 km thick sediment layer south of Bermuda from a refraction survey. Another cause of this could be that we used the wrong depth for the source. The source depth for the synthetics is 5 km but the event could be deeper. For the long periods this will have no effect but the shorter periods could be changed slightly. To match the timing of the first arrival a lid velocity of 4.75 km/sec was needed. The separation of the first downswings requires a lid thickness of at least 80 km. At these distances a thicker lid would appear about the same. Primary rays from below the lid are not noticeable.

In figure 6 we show further data at regional distances. These stations are within continents and the transition from oceanic to continental crust has an obvious affect on the waveforms. The overall period of these signals is much longer than the SJG record from the same event. From the previous discussion, this is what one would expect for an increase in crustal thickness. We used a crust of 19.5 km, with the same velocity as before, to model these records. This was found empirically to fit the overall dispersion of the data. How the actual ocean-continent transition affects the Love wave is not clear but since the crustal thickness does not change the arrival time by much, using an average thickness for the crust is probably sufficient. Note that the arrival times are well fit for this data set using the same model as in the previous figure. Since we have fit data in three directions, from

the same event, with the same model, it appears the event was not greatly mislocated, nor is there a large directional anisotropy. The arrows, in the figure, indicate the reflected arrival from the 400 km discontinuity. It can also be seen in the data at about the right time. The data, in the previous figures, constrain the lid to have a high velocity (4.75 km/sec) and a thickness of at least 80 km. The timing of the 400 km reflection indicates the velocities below the lid must be significantly lower than those found in the shield in paper 1. Further evidence for the thick lid will be presented later in relation to the SS data.

Structure below the lid

Figure 7 shows the travel-time curve for the Atlantic model. The previous data basically established the AB branch to 16° , this is energy from the lid. The two seismograms at 16.3° and 16.8° showed an arrival corresponding to the cusp labeled C, a reflection from the 405 km discontinuity. The dashed lines refer to diffracted energy or tunnelled energy through the lid. There are several more seismograms from events 1 and 2 which sample deeper than the lid. Figure 8 shows a small profile to the north of these events. Again, most of the paths are through old ocean but the receivers are on continental crust. In the

synthetics we again used an 'average' crustal thickness of 19.5 km. The crustal arrivals, or Love waves, arrive just after the branch labeled B. Errors in our crustal approximation should not affect the measurements of the mantle arrivals which determine the triplication curve. The mechanism appropriate for event 2 was used in the synthetics. This is inappropriate for the record at SCH from event 1 causing some of the misfit there, though there are obvious arrivals in the record corresponding to those in the synthetic at the right time. With respect to figure 7, we can follow the three branches over several degrees. Branch F is from below the 660 km discontinuity, branch D is a wide angle reflection from the 660 and branch B is the wide angle reflection from the 405 km discontinuity. The model derived from East Pacific Rise data in paper 1, which we used below 200 km, fits the timing of all the branches very well. Differences of 1% over 200 km at any depth range would be noticeable in the relative timings of these phases.

In figure 9, two records from this profile are shown compared to synthetics computed from the Atlantic model and a modified Atlantic model. The modified model is the same as the Atlantic model except from 225 to 400 km depth, where we have substituted the velocities found beneath the Canadian shield at those depths. The SCH synthetics were done using the appropriate source for event 1, also the Love wave was not included as this station is much further inland than the others and the Love wave arrives later. This figure illustrates the sensitivity of the arrival time of branch B to the structure from 200 to 400 km. The arrows indicate the arrival from the 400 km discontinuity in the data

and synthetics. The modified model is too fast by about 5 sec. The velocity could be decreased from 100 to 200 km to compensate for this but the observations of branch C at 16° and in the SS data (shown later) limit the amount one can modify the structure. Note that the 660 triplication is hardly changed at all by the modification.

From this small data set we can conclude several things. With the constraint of a high velocity lid, the velocity from 200 to 400 km must be substantially the same as beneath the East Pacific Rise. Also, the structure below 400 km appears to be identical to both the Canadian shield and the East Pacific Rise.

Observations of SS

Events 3 through 9 are further from the stations than the previous data, but they can still be used for studying the upper mantle. Events 3, 4 and 5, in particular, have paths to east coast stations through ocean mostly older than 100 m. y.. These events produced data in the range 27 to 53° , thus the SS phases from these earthquakes are going through the same triplications as S waves from 13.5 to 26.5° . As discussed in paper 1, SS data in this range can be very useful in modeling the mantle. The S wave bottoms below 800 km where the

structure is fairly well known. The source and receiver structure is the same for both S and SS, thus the S wave serves as a useful absolute time marker for the SS phase which travels through the heterogeneous upper mantle.

Figure 10 illustrates the synthetic construction of seismograms in this range. These seismograms were computed using the Cagniard-de Hoop technique. The first column shows the results of just adding in primary S rays. The triplication branches are labeled on the diagram. The backbranch due to the 660 discontinuity can be followed to near 32° . The 400 backbranch is seen to about 30° but there is a small arrival continuing to greater distances. This more distant phase is not actually from the 400 km discontinuity but is due to rays coming just out of the shadow zone, bottoming near 250 km depth, which travel to large distances because of the high velocity thick lid. If there is a low Q layer below the lid this arrival could be more attenuated. In the second column we have added what we call the Love rays. These are multiples in the lid and crust. For this example, a 19.5 km crust was used, as the following data are all from continental stations. Rays with 25 reflections in the crust and up to 4 reflections from the bottom of the lid were used. One multiple within the lid was also found to be necessary. One can see that this energy drastically changes the appearance of the seismograms near the 400 km backbranch time. As stated before, this arrival does not interfere with upper mantle arrivals in continental areas. Finally, in the third column, we have added SS rays from below the lid. The major effect of these rays is .

seen from 37 to 40°. The SS B branch from the 400 km discontinuity can be seen clearly. Even at 40° it is well behind the Love wave.

The Love wave, at these distances, again provides information on the thickness of the lid. In figure 11 we have computed just the Love rays at a distance of 40°. The crust is fixed at 19.5 km and the lid velocity is 4.75 km/sec, as was found before. We have varied the lid thickness from 50 to 110 km. Again, the rays reflecting from the bottom of the lid are negative relative to those of the crustal rays. The thinner lids have stronger reflections from this boundary and thus there is more destructive interference of the front of the Love wave. Figure 11 shows the response of a WWSS instrument, convolved with a 5 sec trapezoidal time function, to the Love rays. The arrival time of the first large upswing is very sensitive to the lid thickness. The front of the Love wave from 27 to 40° should, then, put constraints on the lid. The other arrivals, at these distances, will constrain the deeper structure.

Figure 12 shows the data in the range discussed above with the same synthetics as were derived in figure 10. The traveltime lines in figure 10 are again reproduced in this figure on the data and synthetics. The stations, listed next to the seismograms recorded by them, are of varying distances from the ocean. We used a 19.5 km thick crust as an approximation to the actually more complicated situation. This thickness seems to satisfy the dispersion of the later part of the Love waves recorded at these stations and should not affect the mantle

arrivals too much. All the arrivals pointed out in the previous discussion of the synthetics can be seen in the data. The arrival time and amplitude decay of the 660 km discontinuity, branch D, is modeled extremely well. The structure near 600 km was derived from a totally different area so that this fit is quite surprising. This indicates that heterogeneity below 400 km from the East Pacific Rise to the Canadian shield to the old northwest Atlantic is extremely small. Velocity differences of 1% from 400 to 600 km would change the synthetics significantly at these ranges.

From 38 to 40° the B branch of the 400 km discontinuity is visible in the data, as an SS arrival. It can be identified by the higher frequency content than the preceding Love wave pulse and its moveout from the S wave. Data beyond 40° confirm our identification of the SS B branch. Note, also, that the timing is consistent with the arrival at 16°, figure 6, which we modeled as the 400 km reflection. The midpoints of these paths are in ocean older than 100 m. y..

The part of this section showing the most variability in the data is indicated by the line labeled B. The arrivals just following this line are due to rays from several depths as was illustrated in figure 10. The front part of this waveform is due to S rays, and crustal multiples of them, coming from below the lid. This arrival is most sensitive to the velocity from 150 to 350 km. The late time of this phase, in the data, indicate low velocities at this depth range. Just following this energy is the start of the Love wave which travels

at near the lid velocity. The time of this wave group indicates a thick fast lid as discussed earlier. This energy, however, varies by several seconds from station to station but in an understandable way. Comparing the records at ATL from events 3 and 9 one can see that the Love pulse is faster from event 3. From the map, in figure 2, it is seen that the path from event 3 is $3/4$ ocean older than 100 m.y. whereas the path from event 9 is only about $1/2$ ocean that old. Past studies, such as that by Mitchel & Yu (1980), have documented the growth in thickness and velocity of the lid with age in the Pacific. We are probably seeing this phenomenon here. Our model is an average of a varying lid in the older Atlantic. Event 3, at ATL, has a faster Love wave than our model predicts indicating the lid is probably even thicker than 100 km in the older ocean, while the paths from these events are probably through a thinner, lower velocity lid. Never the less, a 100 km, 4.75 km/sec lid does a fair job over these paths, as it did for the data at nearin distances.

In figure 13 further SS data is presented from distances beyond 40° . The stations used for this profile are well inland but again the midpoints are within old ocean. The large distances used here and the fact that the stations are so far inland eliminate contamination by the Love wave. At SHA long period Love wave energy is apparent but it is behind the SS wave and does not present a problem. Since the Love wave is not important here, and the SS phase at these distances is dominated by structure well below the lid, we computed the synthetics in this figure using the more efficient WKBJ technique. No Love wave is

computed. In this range SS passes through the same triplications as S from 20 to 26°. The branches from the travel-time curve in figure 7 are labeled on the synthetics and the data. The data at 41 and 43° are reproduced many times from other events and at other stations. At 41° two arrivals are present, the first is from the 400 km discontinuity (branch C), the second from the 660 km discontinuity (branch E). At 43° they are crossing producing a large simple SS wave. Near 46° the back branch of the 400 km discontinuity begins to separate out and can be followed to 53°. The 660 back branch begins to separate from energy below 660 km near 48° and it too can be followed to 53°. This data just confirms the previous conclusions but also illustrates the compatibility of S and SS wave modeling. Many regions which are inaccessible to an S wave upper mantle study can be sampled with SS.

Discussion

The model derived in this study was based on several assumptions. The lid was assumed to be a homogeneous high velocity layer. Structure in the lid is certainly possible but our technique of calculating synthetics prohibited using more than a couple of layers due to the number of rays needed. We have concentrated on fitting long period data, > 20 sec, which should not be too sensitive to the fine structure

of the lid. A high gradient in the lid would necessitate a thicker lid as the shadow would be moved to nearer distances. Thus, our lid is just an approximation to a more complicated structure which could be thicker.

The velocities just below the lid are difficult to determine due to the extensive shadow zone caused by the lid. We used the same structure below 200 km as was found beneath the East Pacific Rise in paper 1, but there is some tradeoff between the velocity from 100 to 200 km and the velocity from 200 to 400 km. On the other hand, decreasing the velocity in the Atlantic model just below the lid to values found beneath the East Pacific Rise would allow only a slight increase in velocity from 200 to 400 km. Models, such as PREM (Dziewonski & Anderson, 1981), with large velocity jumps near 200 km and corresponding low gradients to 400 km can not satisfy our data. The back branch from the 400 km discontinuity is too fast in these models. Thus we feel confident in the conclusion that the shear velocity from 200 to 400 km beneath the old Atlantic is far closer to the velocities beneath the East Pacific Rise than beneath the Canadian shield.

It is interesting to compare our results to other studies of the upper mantle. Sipkin and Jordan (1976,1980) have measured ScS and multiple ScS times, attributing their variations to upper mantle heterogeneity. For the shield model (SNA), with a 35 km thick crust, ScS is 4 sec faster than that predicted by the Jeffreys-Bullen model. The rise model, TNA, is 6.2 seconds slower and the Atlantic model is just about the same as the Jeffreys-Bullen prediction. For the two

oceanic models we used a 9 km crust. The shield model fits the mean of the measurements by Sipkin and Jordan (1976) for Precambrian shields, though they have a 2 sec scatter for those measurements. Their oceanic data fall between -1 and 8 second residuals. These are mostly measurements in the Pacific ocean with varying oceanic age. Our two oceanic models bracket their data fairly well. Thus the two studies seem compatible as far as generalizing our results to similar tectonic provinces on other parts of the earth.

Figure 14 shows the fundamental Rayleigh wave phase velocity dispersion curves for the three models derived using S and SS. Corrections due to analestacity were included assuming that our bodywave models are appropriate for a period of 10 sec. The Q structure was taken from PREM (Dzeiwonski & Anderson, 1981). The P velocity for the shield was taken from Given & Helmberger (1981) and for the East Pacific Rise from Walck (1983). The Atlantic P model is a modified version of Walck's, with a lid corresponding to the shear wave Atlantic model and the same velocities below 200 km. Again a crust of 35 km was used for the shield model and one of 9 km for the two oceanic models. Data from several regional surface wave studies is included on the curves. The Weilandt & Knopoff study (1982) is for a path along the East Pacific Rise and agrees very well with the dispersion predicted by TNA at all periods but the shortest. The longer period study by Kanamori (1970) is for an average ocean and agrees with the long period results for the ATL model. Finally, the Okal study (1978), looked at paths across North America. The measured phase velocities are lower than those predicted

by our shield model but the Okal paths include significant portions of the slower western part of North America. The long period studies agree well with our results. There are 4% differences in phase velocity at 150 sec decreasing to 1.5% differences at 270 sec for the three tectonic regions. At the shorter periods (<120 sec) the agreement with other studies is worse. In particular, the results of Mitchel & Yu (1980) for old ocean are much lower than ours. Similarly, the Brune & Dorman (1963) study of the Canadian shield found lower velocities than our shield model predicted. This could be due to anisotropy, as recently discussed by Anderson & Regan (1983), or actual lower values of Q , than we used, at shallow depths. The Mitchel & Yu study was for the Pacific ocean and could indicate a real difference between the old Atlantic and old Pacific. In conclusion, the long period Rayleigh wave dispersion predicted by our models agrees well with other studies in other areas of the earth, indicating good agreement with our deeper structure. The shorter periods show large variations which could be due to a number of causes.

Conclusion

We have modeled the waveforms and traveltimes of SH wave motion in the older portions of the northwest Atlantic to investigate the upper

mantle. The old Atlantic has a thick high velocity lid beneath which the structure is very similar to that found near the East Pacific Rise in a similar study. Using the same technique, the Canadian shield was found to have significantly higher velocity than both oceanic areas to about 400 km depth. The bottom of the lid does not appear to be the depth at which the craton and oceans become indistinct.

Below 400 km the model derived for the Canadian shield and East Pacific Rise fit the Atlantic data quite well. Thus we feel heterogeneity at these depths is very small throughout North America and its surrounding oceans. The agreement with very long period surface wave studies elsewhere suggest the model below 400 km is a pretty good average for the earth.

Acknowledgements

We would like to thank Cindy Arvensen for helping with the data processing and Luciana Astiz, Bradford Hager and Don Anderson for constructive reviews. This research was supported by NSF grant EAR-8306411 and ONR grant 14-76-C-1070. Contribution 4017, Division of Geological and Planetary Sciences, California Institute of Technology, Pasadena, California.

References

- Anderson, D. L., The deep structure of continents, J. Geophys. Res., 84, 7555-7560, 1979.
- Brune, J. & J. Dorman, Seismic waves and earth structure in the Canadian shield, Bull. Seism. Soc. Am., 53, 167-210, 1963.
- Burdick, L. J. & J. A. Orcutt, A comparison of generalized ray and reflectivity methods of waveform synthesis, Geophys. J. R. astr. Soc., 58, 261-278, 1978.
- Chapman, C. H., A new method for computing synthetic Seismograms, Geophys. J. R. astr. Soc., 54, 481-518, 1978.
- Carpenter, E. W., Absorption of elastic waves - an operator for a constant Q mechanism, A. W. R. E. Rep. 0-43/66, 1966.
- Dzeiwonski, A. M. & D. L. Anderson, Preliminary reference Earth model, Phys. Earth Planet. Inter., 25, 297-356, 1981.
- Futterman, W. I., Dispersive body waves, J. Geophys. Res., 67, 5279-5291, 1962.
- Given, J. W., Inversion of body-wave Seismograms for upper mantle structure, Ph. D. Thesis, California Institute of Technology, Pasadena, 154 pp., 1983.
- Given, J. W. & D. V. Helmberger, Upper mantle structure of northwestern Eurasia, J. Geophys. Res., 85, 7183-7194, 1981.
- Grand, S. P. & D. V. Helmberger, Upper mantle shear structure of North America, submitted to Geophys. J. R. astr. Soc.
- Helmberger, D. V., Numerical Seismograms of long-period body waves from seventeen to forty degrees, Bull. Seism. Soc. Am., 63, 633-646, 1973.
- Helmberger, D. V. & L. J. Burdick, Synthetic Seismograms, Ann. Rev. Earth planet. Sci., 7, 417-442, 1979.
- Helmberger, D. V. & G. R. Engen, Upper mantle shear structure, J. Geophys. Res., 79, 4017-4028, 1974.
- Jordan, T. J., Continents as a chemical boundary layer, Phil. Trans. R. Soc. Lond., 301, 359-373, 1981.

- Jordan, T. J., Global tectonic regionalization for Seismological data analysis, Bull. Seis. Soc. Am., 71, 1131-1141, 1981.
- Kanamori, H., Velocity and Q of mantle waves, Phys. Earth Planet. Inter., 2, 259-275, 1970.
- Langston, C. A. & D. V. Helmberger, A procedure for modelling shallow dislocation sources, Geophys. J. R. astr. Soc., 42, 117-130, 1975.
- Mitchel, B. J. & G. Yu, Surface wave dispersion, regionalized velocity models, and anisotropy of the Pacific crust and upper mantle, Geophys. J. R. astr. Soc., 63, 497-514, 1980.
- Molnar, P. & L. R. Sykes, Tectonics of the Caribbean and Middle American region from Seismicity and focal mechanisms, Bull. Geol. Soc. Am., 80, 1639-1684, 1969.
- Officer, C. B., M. Ewing & P. C. Wuenschel, Seismic refraction measurements in the Atlantic ocean part 4: Bermuda Rise and Nares Basin, Bull. Geol. Soc. Am., 63, 777-808, 1952.
- Okal, E. A., Observed very long-period Rayleigh-wave phase velocities across the Canadian shield, Geophys. J. R. astr. Soc., 53, 663-668, 1978.
- Okal, E. A. & D. L. Anderson, A study of lateral heterogeneities in the upper mantle by multiple ScS travel-time residuals, Geophys. Res. Lett., 2, 313-316, 1975.
- Sclater, J. G. & B. Parsons, Oceans and continents: similarities and differences in the mechanisms of heat loss, J. Geophys. Res., 86, 11,535-11,552, 1981.
- Sipkin, S. A. & T. H. Jordan, Lateral heterogeneity of the upper mantle determined from the travel times of multiple ScS, J. Geophys. Res., 81, 6307-6320, 1976.
- Stewart, G. S. & D. V. Helmberger, The Bermuda earthquake of March 24, 1978: a significant oceanic intraplate event, J. Geophys. Res., 86, 7027-7036, 1981.
- Thatcher W. & J. N. Brune, Higher mode interference and observed anomalous Love wave phase velocities, J. Geophys. Res., 74, 6603-6611, 1969.
- Walck, M. C., The P-wave upper mantle structure beneath an active spreading center: the Gulf of California, submitted to Geophys. J. R. astr. Soc.
- Wielandt, E. & L. Knopoff, Dispersion of very long-period Rayleigh waves along the East Pacific Rise: Evidence for S wave anomalies to 450 km depth, J. Geophys. Res., 87, 8631-8641, 1982.
- Wiggins, R. A., Body wave amplitude calculations-2,

Geophys. J. R. astr. Soc., 46, 1-10, 1976.

Table 1Atlantic Model

<u>Depth, km</u>	<u>Velocity, km/sec</u>	<u>Depth, km</u>	<u>Velocity, km/sec</u>
0.0	3.7	450.0	5.09
9.0	3.7	475.0	5.135
10.0	4.75	500.0	5.19
25.0	4.75	525.0	5.24
50.0	4.75	550.0	5.29
75.0	4.75	575.0	5.345
100.0	4.75	600.0	5.395
125.0	4.54	625.0	5.445
150.0	4.49	659.0	5.50
175.0	4.47	660.0	5.91
200.0	4.46	675.0	5.98
225.0	4.46	700.0	6.05
250.0	4.48	725.0	6.13
275.0	4.51	750.0	6.20
300.0	4.57	775.0	6.22
325.0	4.63	800.0	6.24
350.0	4.68	825.0	6.26
375.0	4.73	850.0	6.275
405.0	4.78	875.0	6.29
406.0	5.00	900.0	6.305
425.0	5.05	925.0	6.32

TABLE 2

<u>Event</u>	<u>Date</u>	<u>Location</u>	<u>Origin Time</u>
1	Mar. 24, 1978	29.9°N 67.3°W	00h 42m 37.7s
2	Nov. 3 ,1966	19.2°N 67.9°W	16h 24m 31.3s
3	Nov. 18, 1970	35.2°N 35.7°W	12h 23m 18.0s
4	May 17, 1964	35.2°N 35.9°W	19h 26m 20.6s
5	Mar. 28, 1976	33.8°N 38.6°W	20h 19m 45.6s
6	Mar. 26, 1980	23.9°N 45.6°W	20h 43m 37.9s
7	Oct. 20, 1972	20.6°N 29.7°W	4h 33m 48.9s
8	Jun. 2, 1965	15.9°N 46.7°W	20h 40m 23.5s
9	Jun. 19, 1970	15.4°N 45.9°W	14h 25m 18.4s

Figure Captions

Figure 1. Velocity model ATL derived in this study compared to profiles of the Canadian shield (SNA) and the tectonic western North America (TNA).

Figure 2. Stations and events used in the study. The age of the oceanic crust in the region is also indicated.

Figure 3. The step responses after summing various sets of rays in two simple structures. The final panel is the response of a long-period WWSSN instrument to the Green's function above it.

Figure 4. Step responses at 12° for various simple models. To the left are the structures used, in the middle, the step response, and to the right the long-period WWSS instrument response with a time function and attenuation. The dashed line indicates the same reference time.

Figure 5. Data and synthetics for two oceanic paths at nearin stations. The timing is absolute. The data is a above the appropriate synthetic.

Figure 6. Data and synthetics for the Bermuda event to continental stations. The 400 km reflection is marked by an arrow. The timing is absolute.

Figure 7. TriPLICATION curve for the Atlantic model. Dashed lines represent diffracted or tunnelled energy.

Figure 8. A short profile of S waves in the old Atlantic with a synthetic profile to the right. The triPLICATION branches corresponding to figure 7 are indicated.

Figure 9. A comparison of the fits of the Atlantic model to data with a modified Atlantic model. The modified model has shield velocities from 200 km to 400 km and this changes the 400 km back-branch significantly as indicated by the arrows.

Figure 10. The construction of synthetic seismograms from 26° to 40° . The first column shows the effect of just the S rays, the middle has crustal and lid multiples added and the right column has deeper SS rays added. The triPLICATION branches are in reference to figure 7.

Figure 11. A sensitivity study on the effect of lid thickness on the front of the fundamental Love wave. Just lid and crustal multiples are computed for various lid thicknesses.

Figure 12. Data and synthetic comparison from 26° to 40° . The synthetics are from figure 10, several triPLICATION branches from figure 7 are indicated.

Figure 13. Data and synthetic comparison from 41° to 53° . The SS

phase is passing through the triplications as indicated by the travel-time lines. The first arrival S wave is a useful time marker.

Figure 14. Fundamental Rayleigh wave dispersion curves appropriate for the Atlantic model from this study, the shield, and tectonic models found in paper 1 are compared with data obtained from the literature.

⁷²
Fig. 1

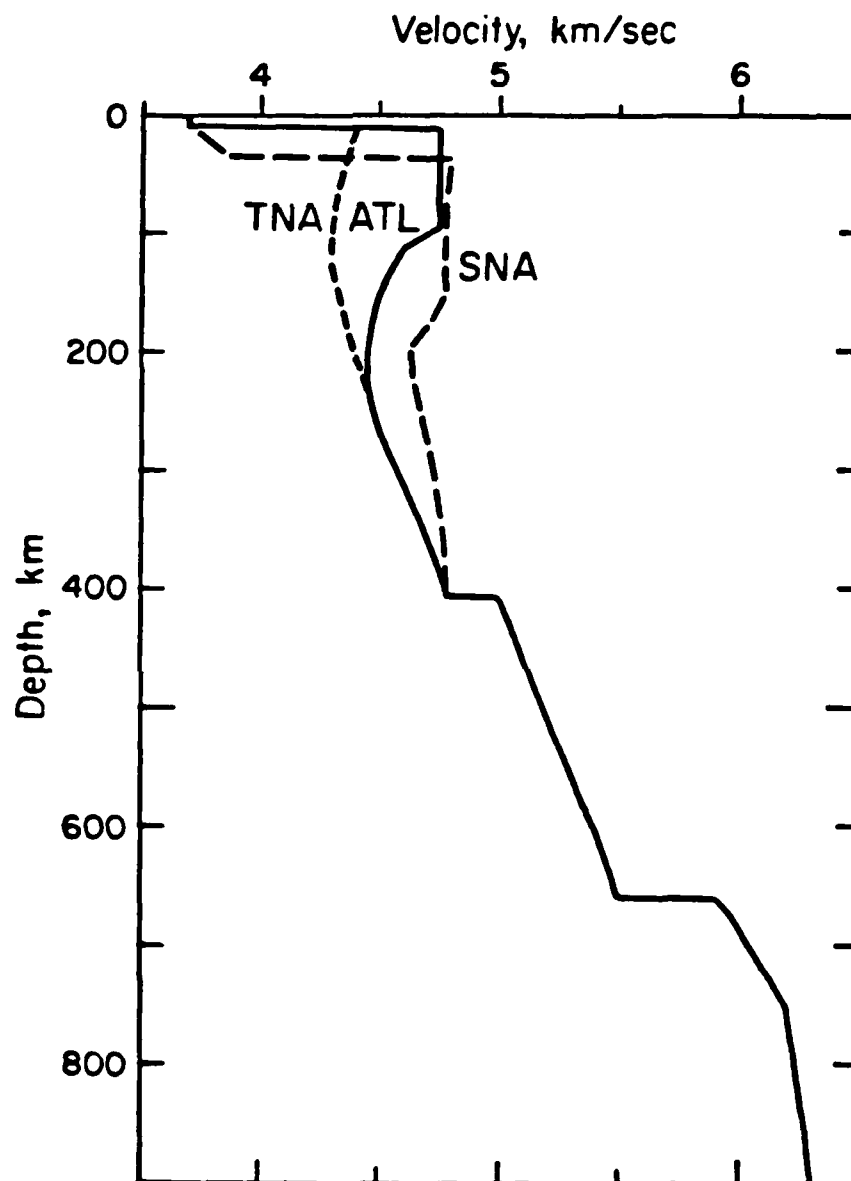


Fig. 73.2

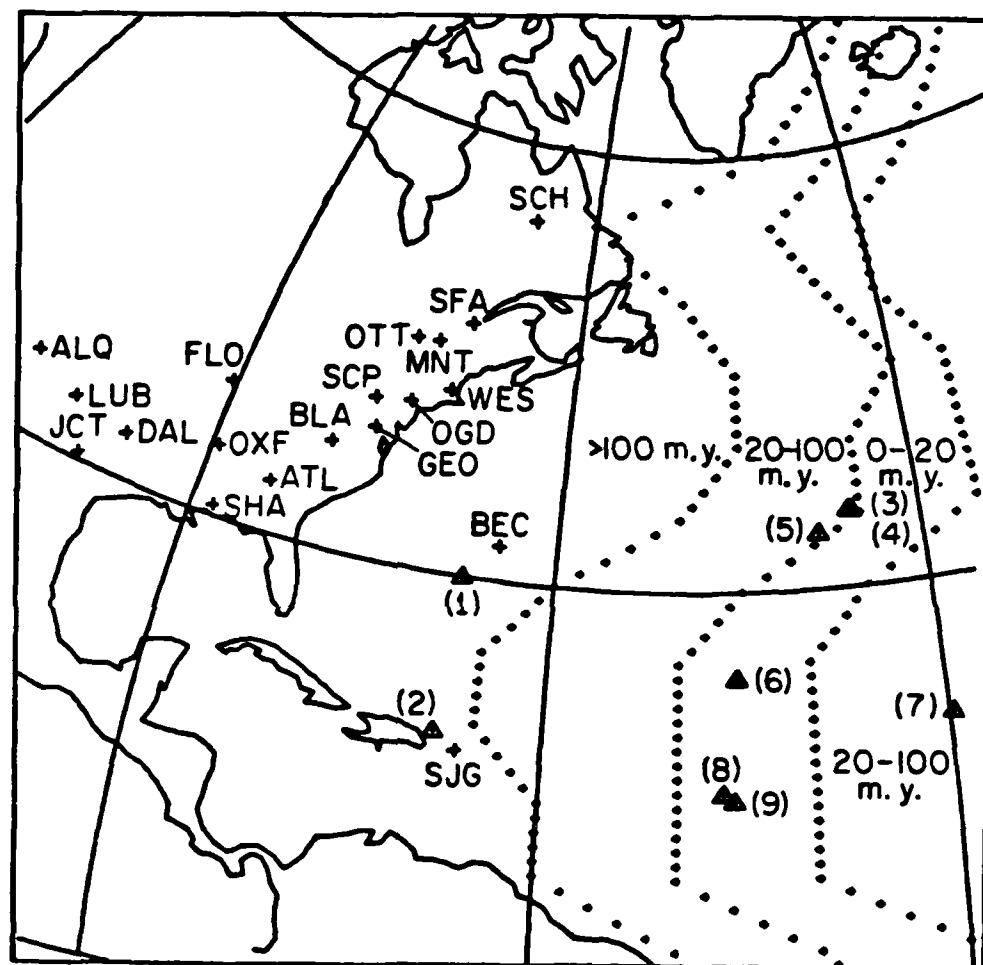


Fig. 3

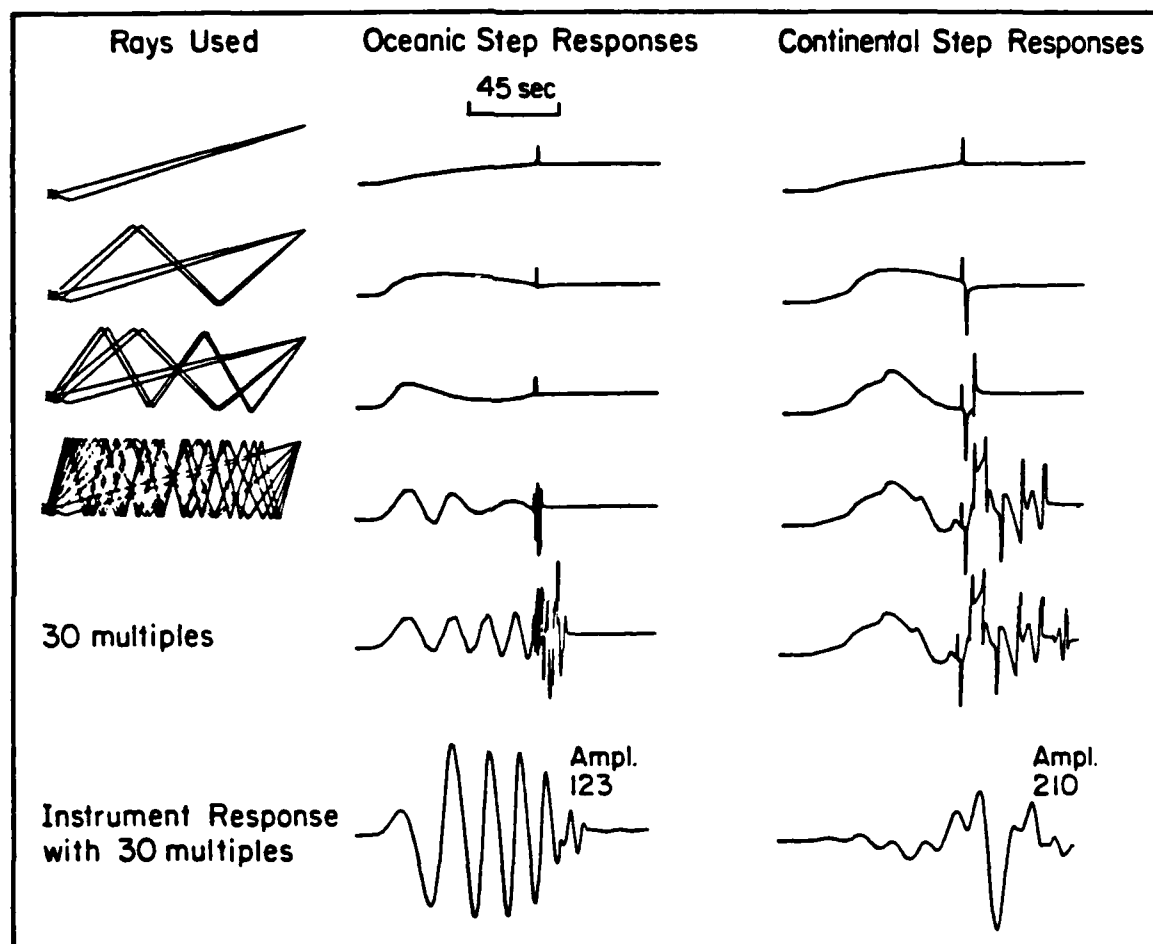


Fig. 4C

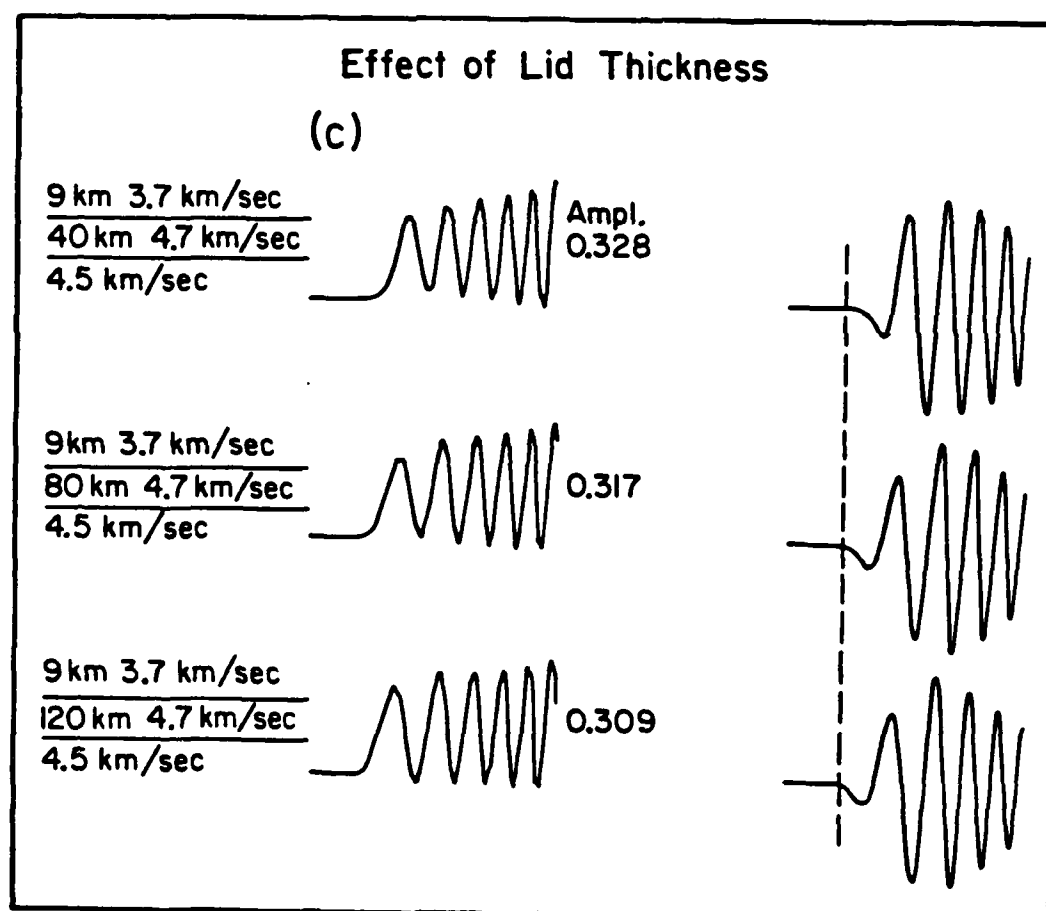


Fig. 5

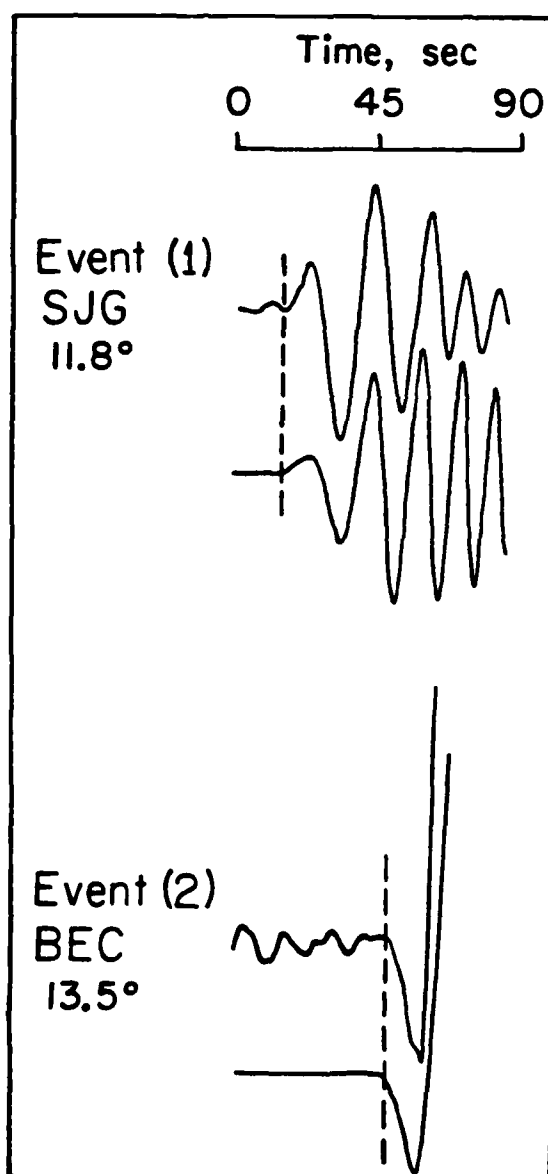


Fig. 6

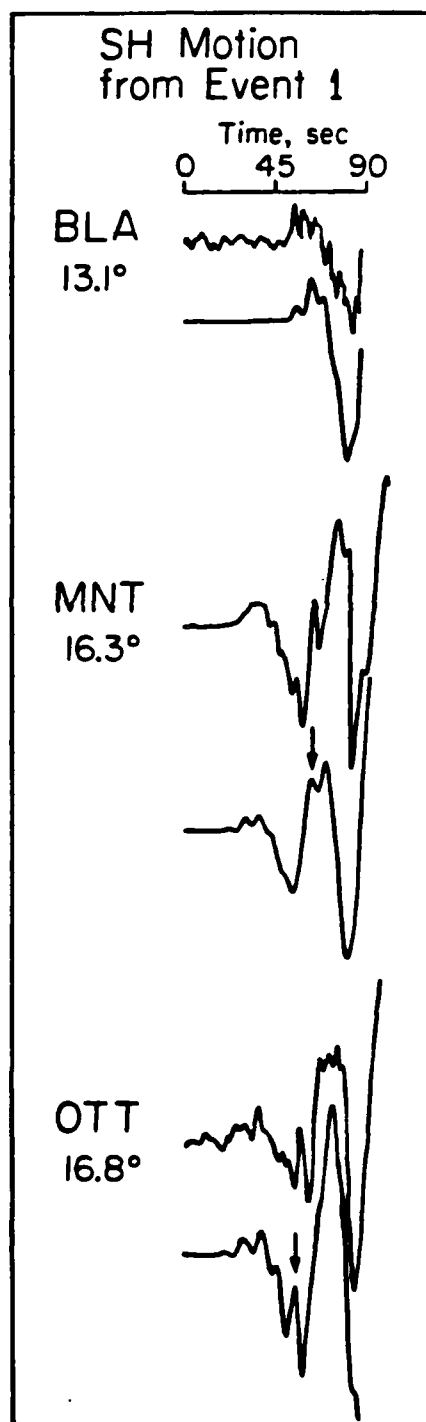


Fig. 7

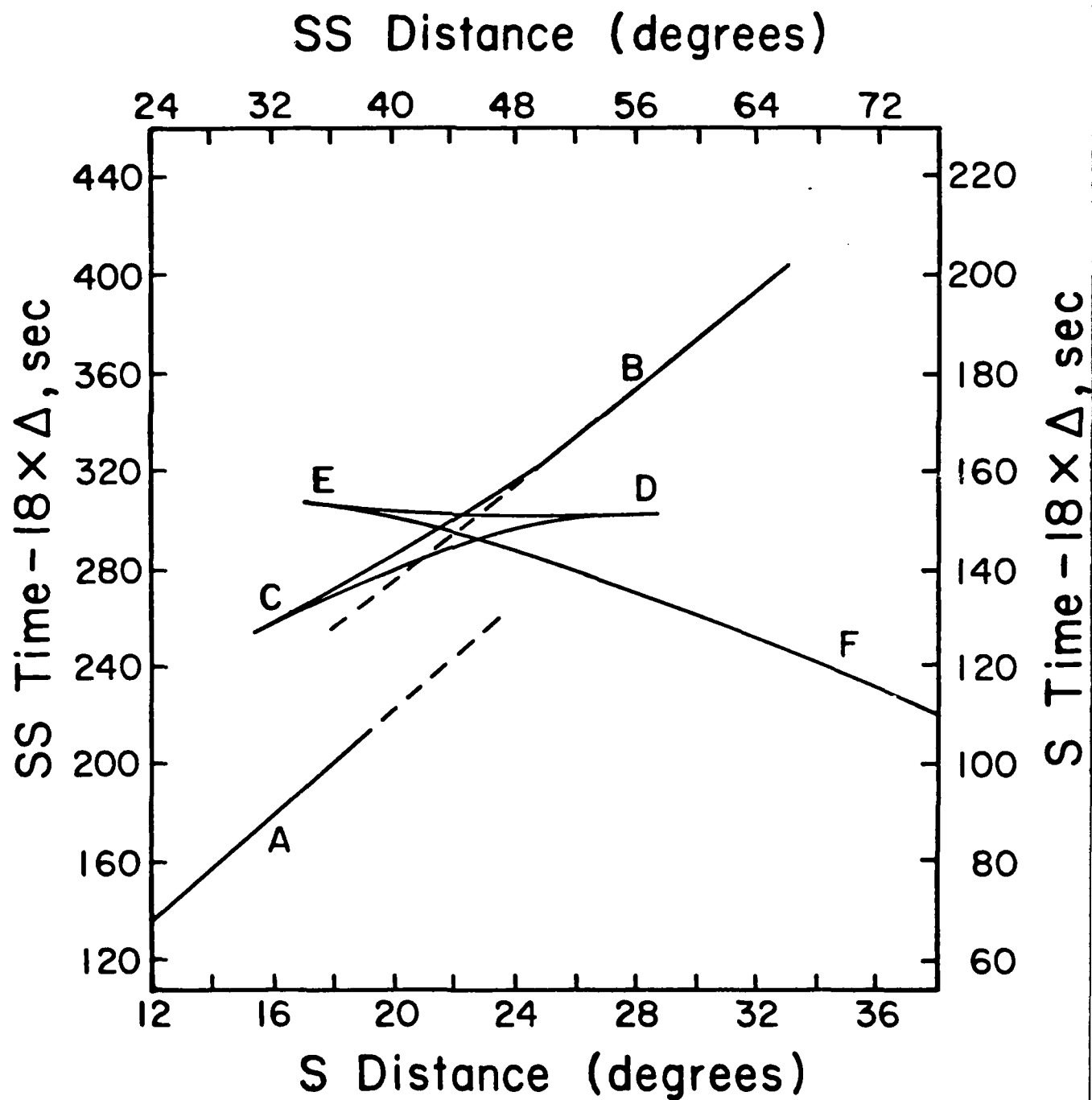


Fig. 8

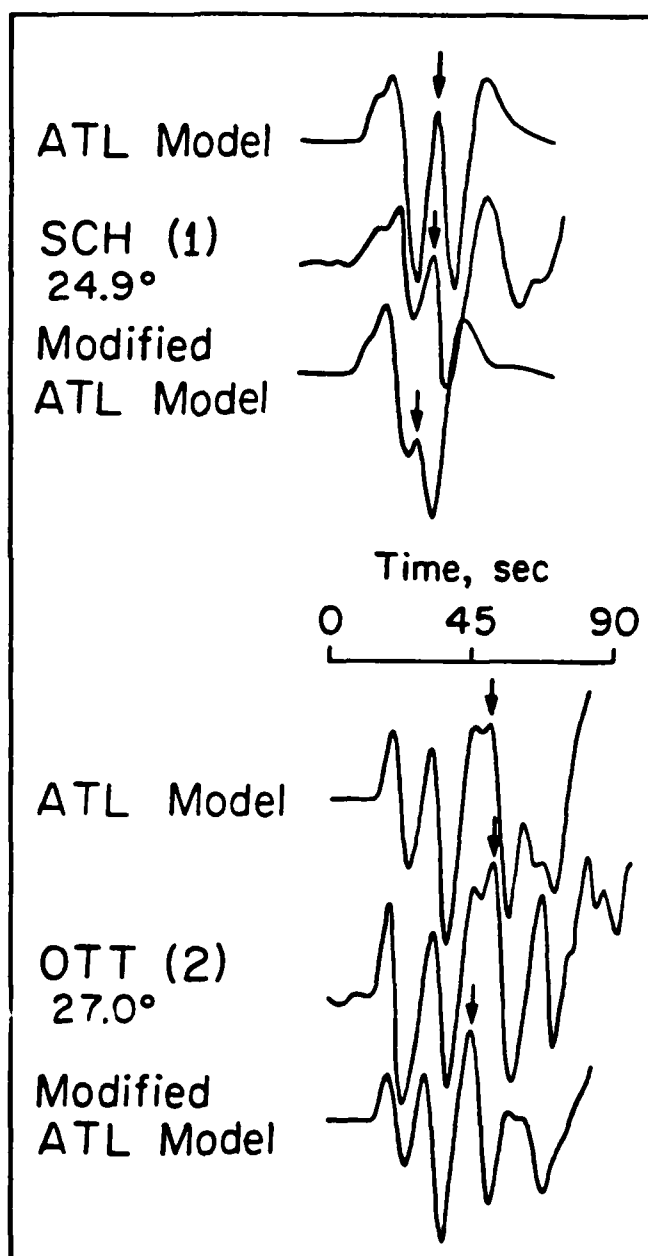


Fig. 9

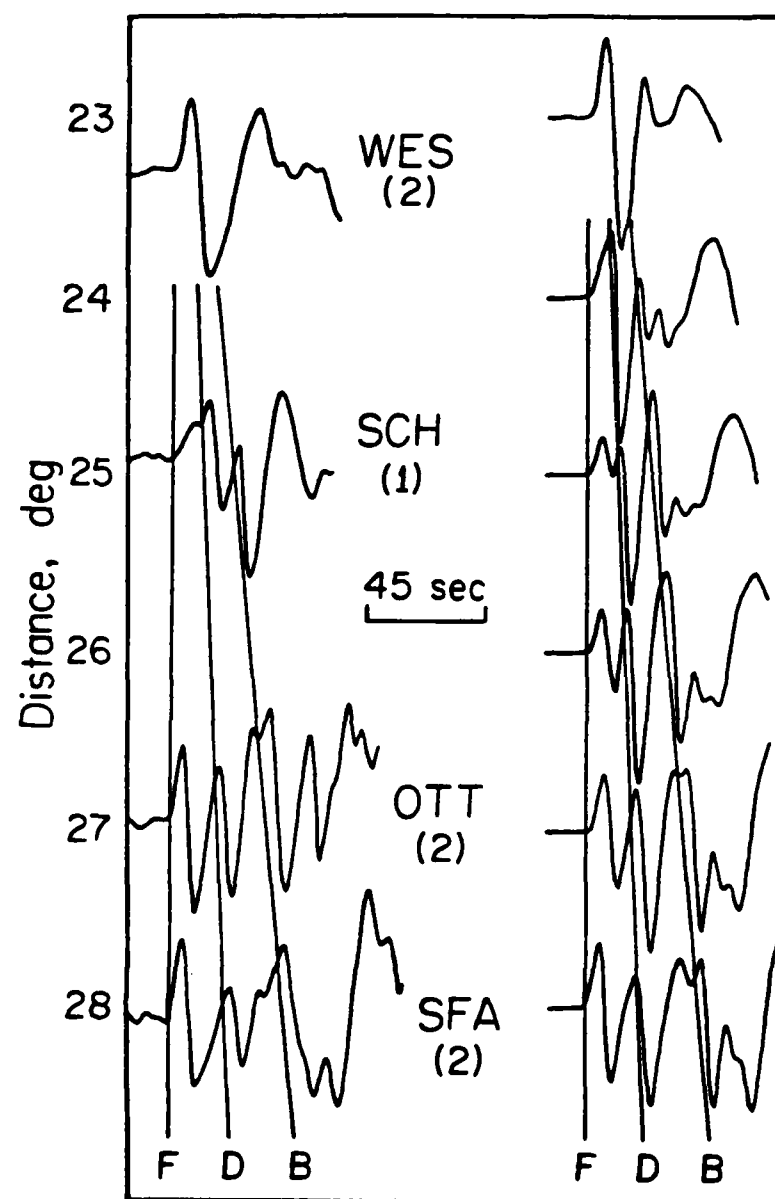
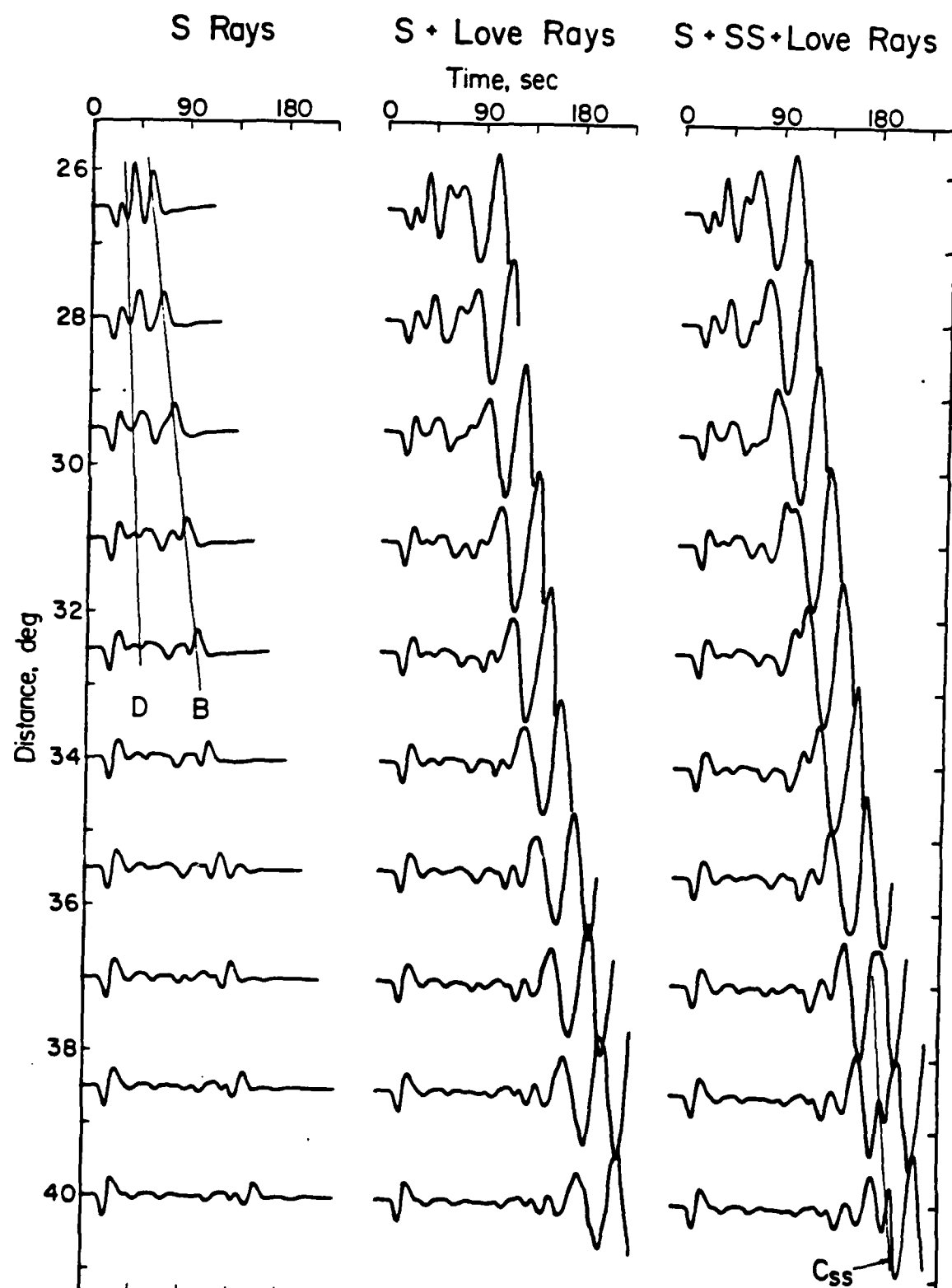


Fig. 10



**IV. Applications of the Transmitted Kirchhoff-Helmholtz Method
to Transmitted Body Waves and Possible Structural Effects at NTS**

Patricia Scott
and
Donald V. Helmberger

ABSTRACT

We extend the Kirchhoff-Helmholtz integral method to calculate acoustic potentials which transmit through three dimensional warped boundaries. We specify the potentials on an arbitrary surface with Snell's law and plane-wave transmission coefficients and numerically integrate their contributions at a receiver via the scalar integral representation theorem. The method is appropriate for modeling precritical transmitted potentials. Results from test models compare well with optical solutions for transmissions through a flat interface. We model the effect of several idealised crust-mantle boundary structures on teleseismic P-waves generated by explosion sources. The structures are all upwarps and are designed to produce travel time residuals as a function of delta and azimuth which have the same magnitude as residuals observed for NTS tests within Pahute Mesa. These structures consistently cause complicated low amplitude waveforms which arrive early and simple high amplitude waveforms which arrive late. Thus they cause systematic amplitude variations with azimuth, delta, and source location. The magnitude of this variation is less than or equal to $2\frac{1}{2}$. This factor is somewhat less than the observed ab amplitude variation with azimuth of Pahute Mesa tests; however it is approximately the same magnitude as the observed ab variation at a given station as a function of test location within the mesa.

I. Introduction

Despite dramatic improvements in the level of sophistication of data analysis, seismologists still cannot deterministically predict many observed amplitude and travel time anomalies of body waves. One hypothesis to explain these anomalies is the presence of non-planar velocity discontinuities such as sedimentary basins, mountains, and faults near the source or receiver. In order for us to assess the importance of this hypothesis, we need a technique for predicting the impact of near source and/or near receiver structural complexity on far-field waves. In this paper, we present such a method based on the numerical evaluation of the Kirchhoff-Helmholtz integral with use of modified tangent plane boundary conditions. This method calculates the response of a wave which is transmitted through a warped boundary between two acoustic media. It contrasts from Scott and Helmberger (1983) where the reflections from a warped boundary are calculated. In this paper we briefly describe the formalism of Kirchhoff-Helmholtz method for the transmitted case. Then, as an example of the method, we model the observed azimuthal amplitude and travel time anomalies of short period P waves from NTS blasts as a result of a geologic structure at the Moho.

II. Formalism

The method in this work is based on the numerical evaluation of the Kirchhoff-Helmholtz integral equation. The formalism differs slightly from that presented in Scott and Helmberger (1983). In that paper we discussed the reflected wave solution; however, here, we state the Kirchhoff-Helmholtz solution for a transmitted potential. We also qualitatively discuss the assumptions

involved in its use.

We wish to calculate a transmitted potential φ_2 at point \underline{x} in a homogeneous body V_2 resulting from an incident source potential located at point \underline{x}_0 in a homogeneous body V_1 . The boundary between the two bodies is ∂V . The sound speeds and densities of V_1 and V_2 are α_1 and α_2 and ρ_1 and ρ_2 respectively. From the scalar integral representation theorem, we write the solution for φ_2 at a point \underline{x} off the boundary ∂V , within V_2 , and at a time t as

$$\varphi_2(\underline{x}, t) = \int_{\partial V} [G_2(\underline{x}, \underline{x}', t) * \nabla \Phi(\underline{x}', t) - \Phi(\underline{x}', t) * \nabla G_2(\underline{x}, \underline{x}', t)] \cdot \underline{n}_2(\underline{x}') dS. \quad (1)$$

Here $*$ denotes convolution and \cdot denotes a vector dot product. G_2 is the fundamental singular solution of the scalar wave equation.

$$\frac{1}{\alpha_2^2} \frac{\partial^2 G_2}{\partial t^2} - \nabla^2 G_2 = \delta(t - t_0) \delta(\underline{x} - \underline{x}_0) \quad (2)$$

In addition \underline{n}_2 is the outward pointing normal of V_2 . Φ and $\nabla \Phi \cdot \underline{n}_2$ are the potential and its normal derivative on the surface ∂V in V_2 . We display the geometry in Figure 1(a) for this problem.

Equation (1) is exact for the initial conditions that $\varphi_2(\underline{x}, 0)$ and $\dot{\varphi}_2(\underline{x}, 0)$ equal zero throughout V_2 . The derivation can be found in Mao and Pao (1971) or Stratton (1941). To obtain equation (1), one requires that ∂V is a reasonably smooth surface.

We now specify G_2 and Φ . For a homogeneous medium, it is sufficient to use

$$G_2(\underline{x}, \underline{x}', t) = \frac{\delta(t - \tau_2)}{4\pi |\underline{x} - \underline{x}'|}; \quad \tau_2 = \frac{|\underline{x} - \underline{x}'|}{\alpha_2}. \quad (3)$$

If the incident field in V_1 results from an isotropic point source at \underline{x}_0 , then ϕ is approximated by

$$\phi = \frac{Tf(t-\tau_1)}{|\underline{x}-\underline{x}_0|}; \quad \tau_1 = \frac{|\underline{x}-\underline{x}_0|}{\alpha_1}. \quad (4)$$

Here T is the acoustic plane wave transmission coefficient for a flat interface and is dependent on the local incidence angle at each point. $f(t)$ is the time function of the incident source function. The function in equation (4) approximates ϕ well if the incident source field is of sufficiently high frequency such that every point on the surface transmits the incident pulse as though there were an infinite plane tangent to the surface at that point. Then the amplitude and the phase on the surface can be described locally by plane wave transmission coefficients and Snell's law. The value of the potential at one point is independent of the values at other points. Hence the contributions of diffractions and multiple scattering to the potential are neglected.

We now estimate the normal derivatives $\frac{\partial \phi}{\partial n_2}$ and $\frac{\partial G_2}{\partial n_2}$.

$$\frac{\partial \phi}{\partial n_2} \cong \frac{-T\dot{f}(t-\tau_1)}{|\underline{x}-\underline{x}_0|} \frac{\partial \tau_1}{\partial n_2} \quad (5)$$

$$\frac{\partial G_2}{\partial n_2} \cong \frac{-\dot{\delta}(t-\tau_2)}{4\pi|\underline{x}-\underline{x}|} \frac{\partial \tau_2}{\partial n_2} \quad (6)$$

The dot over the functions in (5) and (6) signifies time derivative. We approximate the normal derivatives by assuming the amplitudes of G_2 and ϕ vary slowly on the surface relative to the phase. Hence we can discard the terms

$\frac{1}{4\pi} \delta(t-\tau_2) \frac{\partial}{\partial n_2} \left(\frac{1}{|\underline{x}-\underline{x}|} \right)$ and $f(t-\tau_1) \frac{\partial}{\partial n_2} \left(\frac{T}{|\underline{x}-\underline{x}_0|} \right)$. Substitution of equations

(3), (4), (5) and (6) into equation (1) yields

$$\varphi_2 = \frac{1}{4\pi} \int_{\partial V} \frac{Tf(t-\tau_1-\tau_2)}{r_0 r} \left(\frac{\partial \tau_2}{\partial n_2} - \frac{\partial \tau_1}{\partial n_2} \right) dS \quad (7)$$

where $r = |\underline{x} - \underline{x}|$, the distance from the surface to the receiver, and $r_0 = |\underline{x} - \underline{x}_0|$, the distance from the source to the surface. We note that the discarded parts of normal derivatives are proportional to $\frac{1}{r_0 r^2}$ and $\frac{1}{r r_0^2}$. For problems computed in this study, the distance from the source to the surface averages 40 kilometers and the distance from the surface to the receiver averages 20,000 kilometers. The $\frac{1}{r_0 r^2}$ and $\frac{1}{r r_0^2}$ terms are 6.25×10^{-13} and 3.1×10^{-9} , respectively, and are small relative to the term $\frac{1}{r_0 r}$ in equation (7), which is 1.25×10^{-7} . We therefore discard these terms with confidence.

To estimate $\frac{\partial \tau_1}{\partial n_2}$ and $\frac{\partial \tau_2}{\partial n_2}$, we recall that the gradient of the phase is parallel to the normal of the wavefront and has units of slowness. Thus,

$$\frac{\partial \tau_1}{\partial n_2} = \frac{\cos \theta_1}{\alpha_1} \quad (8)$$

$$\frac{\partial \tau_2}{\partial n_2} = \frac{\cos \theta_2}{\alpha_2} \quad (9)$$

where $\cos \theta_1$ is the cosine of the angle between the normal to the refracted wavefront and the normal to the surface \underline{n}_2 . It is equal to

$$\cos \theta_1 = \left(1 - \frac{\alpha_2^2}{\alpha_1^2} \sin^2 \theta_i \right)^{1/2} \quad (10)$$

where θ_i is the local incident angle calculated by

$$\cos\theta_i = \frac{(\underline{x} - \underline{x}_o) \cdot \underline{n}_2}{r_o} \quad (11)$$

$\cos\theta_2$ is the cosine of the angle between the normal \underline{n}_2 and a ray connecting the surface and the receiver. Thus

$$\cos\theta_2 = \frac{(\underline{x} - \underline{x}) \cdot \underline{n}_2}{r} \quad (12)$$

Figure 1(b) shows a detailed picture of these angles. Substitution of the cosine factors (10) and (12) yields

$$\varphi_2 = \frac{1}{4\pi} \int_{\partial V} T \dot{f}(t - \tau_1 - \tau_2) \left(\frac{\cos\theta_2}{r_o r \alpha_2} - \frac{\cos\theta_1}{r_o r \alpha_1} \right) dS. \quad (13)$$

The method for the calculation of equation (13) is discussed in Scott and Helmberger (1983). We simply calculate the integral as a summation of single point evaluations of the integrand. This method of integration requires that the elements which comprise the surface be small in length compared to the incident source wavelength. As in Scott and Helmberger (1983) we obtain the numerical ramp response from this integration and convolve it with the analytical third derivative of a Haskell isotropic source. Thus we obtain $\dot{\varphi}_2$, the time derivative of the potential.

These calculations are appropriate for precritical transmissions in a linear acoustic media. We do not allow the transmission coefficient to be complex. When the incident angle θ_i exceeds the critical angle, ϕ equals zero. This boundary value is consistent with geometric ray theory, but is not a realistic

shadowing function. Rather we expect Φ and $\frac{\partial \Phi}{\partial n_2}$ to vary smoothly across the shadow boundary if the surface is reasonably smooth. However, we argue that, under the circumstances considered here, the postcritical incidence portions of the integral contribute to the summed response of the transmitted potential at times much later than the specular portions and, therefore, are unimportant.

As a check of the method, we compute the transmitted response of a wave propagating through a planar boundary separating two volumes of different sound speeds. We then compare the numerical maximum amplitude with that obtained from the following first motion formula:

$$\varphi_t = TLf\left(t - \frac{r_s}{\alpha_1} - \frac{r}{\alpha_2}\right). \quad (14)$$

Here L is the spreading coefficient (Langston, 1977; Hong, 1978)

$$L = \left\{ \left(\frac{z_1}{\eta_{v1}} + \frac{z_2}{\eta_{v2}} \right) \left(\frac{z_1}{v_1^2 \eta_{v1}} + \frac{z_2 \eta_{v1}^2}{v_2^2 \eta_{v2}^3} \right) \right\}^{\frac{1}{2}} \quad (15)$$

where z_1 and z_2 are the vertical distances of the source and receiver respectively from the boundary. η_{vi} is

$$\eta_{vi} = \left(\frac{1}{\alpha_i^2} - p_o^2 \right)^{\frac{1}{2}} \quad (16)$$

where p_o is the ray parameter.

Figure 2 shows examples of this comparison. We have computed transmitted potentials for an incident isotropic source which is the first derivative of a Haskell source with parameters ($B=2$, $K=10$). The velocity and density model used for the comparison calculations are shown in the top of Figure 2(b).

We show two Kirchhoff synthetics in Figure 2(a) to demonstrate the nature of truncation phases which can contaminate the synthetics. These phases arrive approximately $3\frac{1}{2}$ seconds after the first arrival in both synthetic A and synthetic B and they are artifacts of the technique. In synthetic A, the phase is a result of the finiteness of the grid. A diagram to the left of the synthetic shows this effect. The grid is a square with a length of 150 kilometers. The source is 500 kilometers above the center of the grid and the receiver is 1000 kilometers below the source. From this diagram, we observe that the edge interferes at a time $t_2 = \frac{r_{s2}}{\alpha_1} + \frac{r_2}{\alpha_2}$. The geometric ray arrives at a time $t_1 = \frac{r_{s1}}{\alpha_1} + \frac{r_1}{\alpha_2}$. Hence the truncation phase arrives 3.6 seconds later than the first arrival in synthetic A.

In synthetic B, the phase is a result of the shadowing function. We use the same grid to calculate synthetic B as for synthetic A; however the source is 167 kilometers above the interface. For this velocity model, the local angle between the incident ray and the normal to the surface exceeds critical when the distance from the center of the grid exceeds 50 kilometers. ϕ on the surface is 0 beyond this distance. This abrupt change in boundary conditions introduces a truncation phase into the synthetic. From the diagram to the left of synthetic, we see that this phase arrives 4 seconds later than the geometric arrival. The truncation phase in synthetic A caused by grid finiteness does not constitute a problem. If it contaminates the phase of interest, we can enlarge the grid appropriately. However, the truncation phase in synthetic B caused by the boundary conditions fundamentally restricts the source-receiver geometries we can investigate.

Figure 2(b) shows a profile of Kirchhoff synthetics for a source 500 kilometers above the interface and five receivers 500 kilometers below the interface. The horizontal distance, x , of the receivers ranges from 0 kilometers, directly underneath the source, to 755 kilometers. The two columns next to the synthetics contain the numerical peak amplitudes and the predicted amplitude from equation (15). The agreement is good. We cannot calculate a response past $x = 755$ kilometers because a truncation phase resulting from the boundary conditions on the interface starts to interfere with the direct arrival. We must always take care to avoid such contamination.

III. NTS Structure (An Example of Near-Source Effects)

We now apply the method by modeling the effects of idealised Moho structures on transmitted teleseismic P waves generated by nuclear tests in Pahute Mesa, Nevada Test Site. We wish to ascertain whether focusing-defocusing by structure on the Moho explains the unusual behavior of amplitudes from these tests.

We review these anomalous observations of short period P waves from Pahute Mesa. Figure 3 is a plot of 1200 ab amplitude measurements from 25 tests within Pahute Mesa as a function of station location from Lay et al., (1983a). The ab amplitudes are measured from the first peak to the first trough. They are corrected for geometric spreading, the instrument gain at 1 second and event size, following a procedure developed by Butler (1984). The amplitudes are relative to a master event which minimises the overall scatter of the data.

AD-A148 589

DETAILED OCEANIC CRUSTAL MODELING(U) CALIFORNIA INST OF 2/2
TECH PASADENA SEISMOLOGICAL LAB D V HELMBERGER
87 NOV 84 N00014-76-C-1070

UNCLASSIFIED

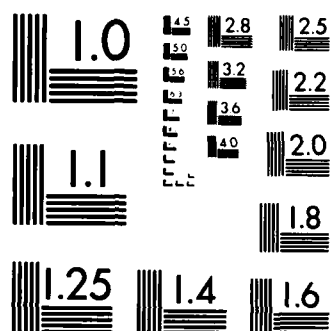
F/G 8/10

NL

END

FILMED

DTIC



MICROCOPY RESOLUTION TEST CHART
NATIONAL BUREAU OF STANDARDS-1963-A

The data has two important features. First, the relative amplitudes range from .13 at station TRI to 5.1 at station SHK. This variation is nearly a factor of 40. Most stations between the azimuths 0° and 60° have significantly lower amplitudes than those between 60° and 120° . Secondly, the relative amplitudes at a given station vary by a factor of $2\frac{1}{2}$ as a function of event location within the mesa. The latter variation clearly originates from a near-source mechanism because the events are separated by, at most, 15 kilometers.

If one calculates the mean relative amplitude at each station, then the overall amplitude variation with azimuth reduces to a factor of 12 (Lay et al., 1983a). The next two figures suggest that this large amplitude scatter is also caused by a near-source mechanism. Figure 4, from Lay et al., (1983a), shows the azimuthal pattern of relative amplitudes for GREELEY, an event within the mesa, and FAULTLESS, an event 100 kilometers outside the mesa. Although both events have comparable yields, their azimuthal patterns differ substantially. This difference is particularly obvious between 0° and 90° . Figure 5 displays plots from Lay et al., (1983b) which enhance the difference between patterns of events in the mesa and events outside the mesa. These plots are ratios of amplitudes of three events outside the mesa (FAULTLESS, PILEDRIVER, and BILBY) divided by the average mesa amplitudes. These ratios are an approximate measure of a near-source anomaly if the FAULTLESS, PILEDRIVER, and BILBY patterns are only influenced by path and receiver effects and are, therefore, constant as a function of azimuth. Furthermore, the path and receiver effects must be characterised by multiplicative factors. Because the ratio patterns for all three events are similar, these assumptions are probably true. Therefore the factor of 13 variation of these ratios between 0° and 120° is roughly an estimate

of the near-source anomaly at the mesa.

To see if this amplitude variation correlates with waveform changes, we plot in Figure 6 several seismograms at stations between 30° and 100° which recorded both FAULTLESS and GREELEY. The top and bottom seismograms are recordings of FAULTLESS and GREELEY, respectively, with their absolute ab amplitudes in microns, corrected for instrument gain only. There is no obvious waveform differences in the GREELEY records which correlate with the dramatic ab amplitude changes. Furthermore we do not see any obvious difference in frequency content and/or complexity between low stations and high stations for either event. However there are some systematic differences between GREELEY and FAULTLESS seismograms. A shoulder occurs 2 to 3 seconds after the first arrival on GREELEY records (e.g. STU, PTO, MAL, STJ, OTT, GEO, and ATL). Lay has also seen these arrivals for other mesa events (Lay et al., 1983b). No such arrival is apparent on the FAULTLESS seismograms. Also the width of the first pulse of GREELEY seismograms is narrower than those of FAULTLESS seismograms at a few stations (e.g. SJG, ATL, BLA, GEO, SCP, and STU). Both phenomena, though, occur throughout the azimuthal range and do not correlate with the ab amplitude changes.

The data demonstrates that near-source anomalies cause a variation of $2\frac{1}{2}$ of relative ab amplitudes at a given station as a function of event location within the mesa. Moreover, near-source anomalies also cause part of the large ab amplitude variation with azimuth (or station location) from mesa events. We cannot completely eliminate contamination of the azimuthal pattern by path and near-receiver effects. Certainly near-receiver effects can be as large as those observed for the Pahute mesa tests (Butler, 1984). Yet the similarity of

the ratio patterns of FAULTLESS, BILBY, and PILEDRIVER suggests that the pattern for mesa tests, seen in Figure 3, is dominated by a near-source mechanism. Finally the variation of relative ab amplitudes with azimuth does not correlate with any obvious waveform changes for a typical mesa event, GREELEY. There is no definitive evidence to determine whether ab variations correlate with travel-time residuals.

In this paper we assume that all the observed amplitude anomalies result from near-source mechanisms. We then test the hypothesis that structure on the Moho, consistent with travel-time residuals, focuses or defocuses P-waves enough to produce the magnitude of the amplitude anomaly. There are alternative near-source explanations for these anomalies. In addition, to the focusing-defocusing hypothesis, workers (Lay, et al., 1983; Wallace et al., 1983) postulate that the movement of faults associated with nuclear blasts causes a superposition of distributed or point double-couple sources with the isotropic bomb source. The amplitude anomalies are, then, the radiation pattern caused by a double-couple source. Longer period studies of Love/Rayleigh ratios, Pnl, P and S waves (Aki and Tsai, 1972; Wallace et al., 1983; Nuttli, 1969) generated by these blasts support the latter hypothesis. However, we speculate that, as the frequency content of the signal increases, the role of lateral near-source structure in distorting amplitudes becomes more important. From travel time residual studies (Minster et al., 1981; Spence, 1974) workers have deduced that there is a high velocity zone directly beneath the Silent Canyon Caldera in the mesa which extends down to 100 kilometers. Such a velocity structure may cause amplitudes which deviate from those predicted by a spherically symmetric Earth model.

To investigate how geology can affect amplitudes, we presume that the apparent velocity variations deduced from the travel time residuals are a manifestation of Moho topography. We exclude from consideration the impact of the Silent Canyon volcanics on transmitted P waves because both Spence and Minster correct the residuals statically for these low velocity rocks; thus the residual patterns are not a result of the caldera. In any case, we cannot readily model a feature so close to the source. If we place a strong velocity discontinuity, such as that between volcanic and granitic rocks, closer than 10 kilometers to the source, we generate a truncation phase which interferes with the transmitted P phase.

We describe the Earth with a two layer crust-mantle velocity model. The velocity of the upper layer is 6.5 km/sec and that of the lower layer is 8 km/sec. The depth of the interface is 45 kilometers. The receivers are located at distances such that the $\frac{1}{R}$ amplitude decay corresponds to spreading at teleseismic distances between 60° and 70° for a JB Earth (Langston and Helmberger, 1975).

The number of ways to distort the Moho is infinite. We, therefore, restrict ourselves to a few three dimensional topographies where the maximum height of the anomaly is 10 kilometers and the maximum width is approximately 25 kilometers. The choice of these values is based on both the Minster et al. (1981) and Spence (1974) studies. They find an advance of $\approx .25-.4$ seconds for nearly vertical rays from shots within the caldera. As these rays become shallow, this advance lessens or disappears completely. From crude calculations, we estimate that 10 kilometers of upward relief on the Moho will produce the required timing anomalies of these rays. Furthermore, we confine the relief laterally so

that rays exiting the mesa at shallow angles are unaffected by the structure. We recognize that these structures are extreme. However, if we cannot produce the observed amplitude anomalies with these topographies, we can discard structure on the Moho as the dominant cause of these anomalies.

Of the infinite number of structures, we arbitrarily select four examples with height $c = 10$ kilometers and width $w = 25$ kilometers. These topographies are described by simple analytical formulas and are convenient to use. The topographies with their labels are as follows:

$$\begin{aligned} \text{Upwarp : } Z &= Z_{con} + \frac{c}{2} (\cos(2\pi((r-w/2)/w)) - 1) \text{ if } r \leq \frac{w}{2} \\ Z &= Z_{con} \text{ if } r > \frac{w}{2} \end{aligned} \quad (17)$$

$$\text{Exponential : } Z = Z_{con} - ce^{-4.605r/\frac{w}{2}} \quad (17a)$$

$$\begin{aligned} \text{Plug : } Z &= Z_{con} - c \text{ if } r \leq \frac{w}{2} \\ Z &= Z_{con} + \frac{c}{2} (\cos(2\pi((r-\frac{w}{2}-5)/w)) - 1) \text{ if } \frac{w}{2} < r \leq \frac{w}{2} + 5 \\ Z &= Z_{con} \text{ if } r > \frac{w}{2} + 5 \end{aligned} \quad (17b)$$

$$\text{Sinc : } Z = Z_{con} - c \text{ sinc} \left[\frac{21.991r}{w} \right] \quad (17c)$$

Here $r = \sqrt{(x-x_c)^2 + (y-y_c)^2}$ and is the horizontal distance of each point on the surface from the midpoints of the grid (x_c, y_c) . Z_{con} is the baseline level of the Moho and is 45 kilometers for all the calculations. The values of the constants in the exponential and the sinc bumps confine the anomaly's width to approximately 25 kilometers. A schematic cross section of each topography is shown in Figure 7. All the structures are symmetric with azimuth.

Initially an isotropic source is directly above the center of the structure; thus, the transmitted potential is only a function of x and z . The source is 45 kilometers above the baseline of the Moho. The transmitted potential is calculated at receivers which are 20,000 kilometers below the source. The horizontal distance of the receivers from the center of the topography ranges from 0 to 7,000 kilometers. Figure 7 shows the transmitted potential and the peak amplitude as a function of x in increments of 1,000 kilometers for each of the four topographies. In addition, the responses for a wave which transmits through a planar boundary are displayed in the first column. The corresponding take-off angle for the flat boundary synthetics are to the left of the column. By comparing these synthetics with those in the other columns, we can determine how much distortion of the waveform is caused by each structure. The synthetics in Figures 7 and 10 do not include a Q and instrument operator or a reflected pP phase. Although these effects are important, we want to examine amplitude and waveform distortions caused by structure with a simple input pulse. The ringing caused by an instrument or pP may mask the presence of multiple arrivals caused by the topography.

All the structures cause intriguing changes in the waveforms and arrival times of the synthetics. The waveform features originate from timing changes caused by each topography. Each point of the Kirchhoff synthetic originates from elements which are illuminated by the source and, in turn, illuminate the receiver at a total travel time, $\sigma = \tau_1 + \tau_2$. We can associate, with each element of the grid, a value of total travel time, $\sigma(x, y)$. The total travel time function on the surface depends on the source location, the receiver location, and the surface geometry. Figure 8 shows examples of this function. Here we calculate

$\sigma(x,y)$ for elements which make up a flat interface B(a), an upwarped interface B(b), a plug B(c), and a sinc function B(d). In each example the source is directly above the center of the structure and is 45 kilometers above the baseline of the interface. The receiver is 20,000 kilometers directly below the source. The contours of constant total travel time are projected onto the topography (top figure in B(a),(b),(c), and (d)). We also display these contours as a function of x and y (bottom figure in B(a),(b),(c), and (d)). The contours are circles because of the particular source-receiver geometry. For the sake of brevity, we only show that portion of the grid which contributes to the initial second of each Kirchhoff synthetic. The synthetics which correspond to these total travel time functions are also shown (middle figure in B(a),(b),(c), and (d)). These figures show how structure on the interface distorts the total travel time contours and, as a result, produces multiple arrivals in the synthetic.

We examine this effect in detail. The contours are in intervals of .125 seconds as are the tick marks below the synthetics in Figure 8. The geometric arrival time occurs at the center of the contour plot. Thus, by counting the contours, we can estimate the cumulative area of the surface which contributes to the synthetic at a given time. We deduce, from Figure 8, that, approximately,

$$A(t) \propto \left. \frac{dS}{dt} \right|_t \quad (18)$$

$A(t)$ is the amplitude of the response at time t . S is the total area of the surface which contributes to the response at time t . For example, the initial .375 seconds of the synthetic from a flat interface results from a rapid increase in the cumulative area of the surface which is illuminated between $t=.125$ and $t=.25$ seconds. After $t=.25$ seconds, the area of the surface is illuminated at a

constant rate. Thus, the resultant synthetic can be viewed as a convolution of the source time function with a step function which starts between $t=.125$ and $.25$ seconds.

We quantify this statement by following an approach developed by Hilterman (1975) and Haddon and Buchen (1981). The symmetry of the source-receiver geometry and the surface geometry allows us to recast the integral (13) as a one dimensional integration with respect to total travel time, σ . If the transmission coefficient varies slowly over the surface, then

$$\varphi_2 \cong \frac{T}{4\pi} f^* \left(\frac{\dot{\Omega}_2}{\alpha_2} - \frac{\dot{\Omega}_1}{\alpha_2} \right) \quad (19)$$

where

$$d\Omega_1 = \frac{\cos\theta_1}{r_s r} dS$$

and

$$d\Omega_2 = \frac{\cos\theta_2}{r_r r} dS$$

$\dot{\Omega}_1$ and $\dot{\Omega}_2$ are the time derivatives of modified solid angles. Ω_1 is a modified solid angle with vertex at the source subtended by the surface S , and Ω_2 as a modified solid angle with vertex at the receiver subtended by S .

We now examine the origins of the multiple arrivals in the potentials which propagate through interfaces with structure. For example, the amplitude and frequency content of synthetics from the upwarp (column 3 of Figure 7) are controlled by the interference of two pulses. The travel time contours in Figure

8(b) for the upwarp differ considerably from those of a flat interface 8(a). Far less of the upwarped surface is illuminated within .25 seconds of the geometric arrival time. Furthermore, the upwarp topography causes subtle changes of the width between travel time contours. There are two locations where this change occurs: 1) at the top of the upwarp and 2) at the edge of the upwarp. The first pulse in this synthetic originates from the elements in the first location while the second pulse originates from the second location. Because the ring of elements which contribute to the second pulse has a larger area than that of elements which contribute to the first pulse, the second pulse is larger than the first pulse.

As the receivers move away from the center, the maximum amplitudes decrease as a result of the interference of the two pulses. We destroy the symmetry of the surface illumination by moving the receivers horizontally. The illumination of elements, which initially was simultaneous, now occurs at slightly different times and causes destructive interference; this destructive interference causes a reduction in peak amplitudes and the broadening of the pulse widths for both phases. Moreover, as the receiver moves out laterally, the planar part of the boundary becomes more important in controlling the amplitude of the transmitted pulse. Hence the amplitudes, travel times, and the waveforms of distorted pulses approaches those of a pulse which has propagated through a flat boundary. This phenomena is present in almost all the top synthetics in Figure 7.

Other intriguing features are present in the synthetics shown in Figure 7. The potentials transmitted through the sinc and exponential bumps shown in columns 3 and 5 have an apparent delay which is not seen in the other

synthetics. These two topographies drop in height near the peak more rapidly than does the upwarp topography. Consequently, fewer elements are illuminated and contribute to the transmitted potential at times near the geometric arrival time. This is illustrated for the sinc topography in Figure 8(d). Hence, the amplitude near the geometric arrival time is lower than amplitudes at later times.

The opposite is true for the synthetics of waves which are transmitted through a plug. They are displayed in column 4 of Figure 7. The topography and travel time contours for the bottom synthetic from this column are shown in Figure 8(c). This figure shows that more elements are illuminated and contribute to the response near the geometric arrival time for this topography than for the upwarp, sinc, and exponential topographies. The resultant synthetic is made up of two pulses of equal size. Each pulse has the amplitude and shape of a wave which has transmitted through a planar interface. The plug is essentially comprised of two planar interfaces, one at $z = 45$ kilometers and the other at $z = 35$ kilometers. The edges of the plug have been tapered to avoid a shadowing problem. While the difference in the interface depths does not alter the amplitudes of the pulses, it does change the arrival times. This slight separation in arrival time causes the observed interference pattern. As the receiver moves out laterally, the timing between the two pulses changes. The pulse width of the first arrival narrows while the width of the second one broadens. By transmitting a wave through such a structure, we vary the maximum amplitude of the synthetics by a factor of $2\frac{1}{2}$.

We confirm that these structures are approximately producing the correct travel time anomalies. We plot the residuals, in addition to the peak amplitudes

of the synthetics, as a function of distance to discern any systematic relationship between the two parameters. We also plot the amplitude of the first pulse if the synthetic is made up of multiple arrivals. This amplitude is measured from the start of the synthetic to the first peak. The plots are displayed in Figure 9. The travel time "residuals" are defined by the difference between the arrival times of transmissions through a bumpy surface and the times of transmissions through a flat surface. Where there is an apparent delay in the synthetics such as in those from the exponential and sinc bumps, we measure the arrival time at the start of the upswing. The amplitudes are uncorrected for geometric spreading. The change of amplitude from spreading, seen in the synthetics in column 1, is negligible in the distance range of interest; hence no correction is necessary.

The "residuals" in Figure 9 produced by these structures behave in a predictable fashion. The transmitted potentials which propagate vertically to stations between 0 to 4,000 kilometers experience the most advance. The exceptions to this behavior are residuals from the sinc and exponential synthetics. We know there is some energy arriving at these nearly vertical stations with .3 second advance from the previous discussion. However, because the energy is so small relative to later pulses, these synthetics appear to have delays.

When the paths of the potentials become shallower, we see that the advance disappears. The planar part of the interface begins affecting the travel times and waveforms. The arrival times of the transmissions through the bumps approach those of transmissions through a flat interface. The exception to this pattern is the residuals of the plug synthetics. These synthetics have an advance of .3 seconds which is constant as a function of horizontal distance. This behavior results from the constant height of the plug across the entire

width of the bump.

What is the relationship between the travel time anomalies and the amplitude anomalies? We predict that as the magnitude of the travel time anomalies decreases the magnitude of the amplitude anomalies decreases also. The amplitudes, as well as the arrival times, will be controlled by the planar part of the surface. This relationship is observable in Figure 9. The amplitudes, except in one case, start to approach the value of .002 at distances ranging from 5,000 to 7,000 kilometers. The exception is the maximum and first pulse amplitudes of the synthetics from the plug topography. These values appear to systematically decrease with distance. However these values do approach the planar amplitudes at distances beyond 7000 kilometers.

Furthermore, waves which arrive earlier than is predicted by planar calculations also have lower amplitudes than is predicted. Contrarily, the synthetics from the sinc topography arrive late and have anomalously high amplitudes. Indeed, the pattern of residual variation is precisely mimicked by the pattern of amplitude variation for this structure. The mimicking of amplitude and travel time anomalies also occurs for synthetics from the exponential bumps.

This mimicking does not occur for synthetics from the upwarp and plug topographies. Each of these synthetics consists of multiple arrivals. Thus, if we take the maximum amplitude as a measure of amplitude anomaly and compare with travel time anomalies, we do not see an obvious correlation between the two parameters. The travel time is perturbed by a relatively small part of the surface. The maximum amplitude is perturbed by a much larger part of the surface. It is a less local property of the topography. If a broader band source time function interacts with the surface, the amplitude anomaly would change

but not the travel time anomaly. To improve the correlation, we measure the amplitude of the first pulse of the synthetic if it is different from the maximum amplitude. These values are shown in Figure 9 by the open circles and triangles for the upwarp and plug synthetics. We do not improve the visual correlation significantly.

The modeling of a symmetric structure demonstrates that such a structure on the Moho, consistent with travel time residuals, causes a factor of $2\frac{1}{2}$ in maximum amplitude variation as a function of distance. The variation of amplitudes of first pulses is somewhat less. Neither variation is as large as the observations of amplitude changes between stations for a given test at NTS. Furthermore, where there is a large amplitude variation, there is significant waveform distortion of the synthetics. Also, the bumps generally cause low amplitudes. We note that the mesa data set has both anomalously high and low amplitudes. The low amplitude synthetics arrive early. However, any relationship between amplitude anomalies and travel time anomalies is dependent on frequency because the effect of a structure on a wave is dependent on frequency.

The modeling to this point produces anomalies which are dependent only on distance because the structures are symmetric. We now introduce asymmetry into the problem by allowing the source to move off the center of a symmetric upwarp. We do these calculations because observed travel time and amplitude anomalies are presented as a function of azimuth. Yet we do not know if these anomalies arise from azimuthal or delta heterogeneities. Additionally, there is an observed variation of amplitude at a given station with a change in source position in the mesa. If we change the source position across a sample structure, can we reproduce the factor of $2\frac{1}{2}$ seen in Figure 3? We also wish to

examine whether there is any systematic relationship between amplitude and travel time anomalies as a function of azimuth as we have done previously with these parameters as a function of distance.

The modeling experiment is similar to the previous one. The receivers are 1000 to 7000 kilometers horizontally away from the center of the topography and 20,000 kilometers below the source. The sources are 45 kilometers above the baseline of the Moho. To produce the azimuthal anomalies in the synthetics, we move the source off the center of the upwarp in one direction in increments of two kilometers. The responses are calculated for seven distances at five different azimuths. We select the topography upwarp for this experiment. The choice of topography is somewhat arbitrary; however, we make this particular choice because this topography causes substantial variation in amplitudes as a function of distance. If this topography fails to produce much azimuthal variation, then the other topographies will fail to do so, also.

Figure 10 shows our results. A cross section of the source-receiver configuration and the geometry of the upwarp is in the center of the figure. In addition, a topographic map of the center portion of the grid is displayed. The contours are in kilometers and the maximum height of the bump is 10 kilometers. The topography map also shows the source locations and the azimuthal lines along which the calculations are done. The resulting waveforms and maximum amplitudes surround these diagrams. Each group of 28 waveforms is calculated for the corresponding azimuth. The groups are made up of four columns of synthetics corresponding to calculations done with the source location designated at the top of each column. Sources A, B, C, and D are, respectively, 2, 4, 6 and 8 kilometers from the center. The rows correspond to calculations done at

the horizontal distances next to the row. In Figures 11, 12, and 13 we plot the travel time residuals, peak amplitudes, and first pulse amplitudes obtained from these synthetics as a function of azimuth for each distance.

There is a change in overall complexity of the synthetics as a function of azimuth. The waveforms from the group at $\theta = 0^\circ$ are simple and impulsive with relatively high amplitudes. Only the stations at 1,000 or 2,000 kilometers have multiple arrivals. As we rotate counter-clockwise around the structure, a greater number of the synthetics in each group have multiple arrivals, and consequently, low amplitudes. Synthetics at $\theta = 135^\circ$ and 180° all have multiple arrivals. The reason for this trend is the same as in the previous modeling study. As the sources move in the direction of a line along $\theta = 0^\circ$, a greater proportion of the elements which constitute the planar part of the grid contribute to the potentials calculated in the direction of this line. Hence, synthetics of this line become more impulsive as the source migrates from position A to position D. In contrast the synthetics at $\theta = 135^\circ$ and 180° remain complex. The elements which contribute to these potentials are largely from the non-planar part of the boundary.

We examine the maximum amplitudes, first pulse amplitudes, and travel time residuals in Figures 11, 12, and 13 for systematics as a function of distance or azimuth. The behavior of maximum amplitude with distance and azimuth is the most variable of the three parameters. The maximum amplitudes as a function of azimuth do not correlate very well with the travel time residuals. The rapid change of this parameter with azimuth and source position reflects the sensitivity of maximum amplitudes to slight changes in relative timing between the two arrivals which make up the synthetics. The least variation of maximum

amplitudes with distance and azimuth occurs at synthetics calculated with source position A, the closest source to the center of the symmetric source. We increase this variation with azimuth and distance when we remove the source further away from the center to positions B, C, and D.

The maximum amplitudes at $\theta = 135^\circ$ for source positions B, C, and D are lower than the amplitudes at other azimuths. This trend is a result of 1) the degree to which the planar part of the grid contributes to the response and 2) the degree of symmetry of the source and receiver locations with respect to the structure. Stations along $\theta = 0^\circ$ and $\theta = 180^\circ$ are in positions of symmetry with respect to the sources. Elements on either side of a line which divides the grid contribute simultaneously to the responses at these stations and, consequently, cause higher maximum amplitudes. Stations along $\theta = 90^\circ$ and $\theta = 45^\circ$ are not symmetrically positioned with respect to the source; however, the planar part of boundary largely contributes to these responses; thus, they have high maximum amplitudes. But receivers along $\theta = 135^\circ$ are placed asymmetrically which causes elements to illuminate at different times; in addition, these elements are largely in the perturbed part of the boundary. These two factors combine to produce the overall lower maximum amplitudes of receivers at $\theta = 135^\circ$.

Although we do not discern any relationship between the maximum amplitudes and the travel time residuals as a function of azimuth, we see a correlation between the first pulse amplitudes and the travel time residuals. Synthetics which have a constant first amplitude as a function of azimuth also have approximately constant travel time residuals. When the travel time advances increase as a function of azimuth, the first amplitudes decrease with azimuth. Thus, early synthetics have lower first amplitudes than the later synthetics. The

trend of early arrivals with low amplitudes and late arrivals with high amplitudes holds true for all azimuths, distances, and source positions.

The travel time residuals decrease as a function of distance at all azimuths except for $\theta = 135^\circ$ and $\theta = 180^\circ$ for sources C and D. At these azimuths, the residuals increase as the distance increases. Clearly if we pull the source off the center far enough, the shallower rays will interact with the upwarped part of the topography while the steeper rays interact with the flat part of the grid.

As the source moves off the center, the range of variation of first amplitudes and travel time residuals as a function of azimuth exceeds the range of these parameters as a function of distance; that is, the trends of these parameters are stronger in azimuth than in distance. Thus, stronger variation of travel time and amplitude anomaly with azimuth than with distance may be an indicator of lateral variation with azimuth, as well as with distance, despite an uneven station distribution of the existing data set.

What conclusions can be drawn from this modeling experiment? Firstly, we create a variation of $2\frac{1}{2}$ of first amplitudes as a function of azimuth and source position. The change of amplitude with source position is largest at $\theta = 0^\circ$ and 45° and is the least at $\theta = 180^\circ$. However, the variation at 0° and 45° is created at the cost of considerable distortion of the waveform. This feature of low amplitude waveforms with complex or broadened pulses and high amplitudes waveforms with simple narrow pulses is not apparent in the mesa data set.

Secondly, we create a trend in the first pulse amplitudes with azimuth. Specifically we cause high amplitudes at $\theta = 0^\circ$, 135° , and 180° . If the source moves far enough away from upwarp, it causes no amplitude anomalies. However structure can produce a systematic azimuthal trend in amplitudes. But we

must be cautious about pushing this interpretation too far. The azimuthal trend is an artifact of the moveout of the source in one direction with respect to the lines of receivers. If we were to distribute sources all over the upwarp and then calculate the averages of the first amplitudes at each azimuth for all the sources, we would undoubtedly eliminate any trend with azimuth. Thus, the stability of the amplitude pattern of all mesa events with azimuth location is not easily explained by structure on the Moho or any unusual velocity plug unless the sources are fortuitously located to one side of the heterogeneity.

Thirdly, we see a visual correlation between travel time residuals and amplitudes of first pulses, but do not see any between residuals and peak amplitudes. This correlation may be diagnostic of structure as opposed to tectonic release.

Discussion and Conclusions

The previous two modeling experiments show that a structure on the Moho which causes travel time residuals compatible with the Minster et al., (1981) and the Spence (1974) studies can produce variations of $2\frac{1}{2}\%$ of amplitudes as a function of delta, azimuth, and source position. The variation is created at the cost of considerable distortion of the waveform. Furthermore the travel time residuals correlate with first pulse amplitudes but not with peak amplitudes. To see whether these initial results are relevant to the Pahute Mesa waveform data, we must now include a pP phase, a Q operator and a short period instrument operator in a few Kirchhoff synthetics.

We choose two sets of five Kirchhoff-Helmholtz synthetics calculated at 4000 kilometers previously for the azimuthal study. The two sets correspond to the source positions A and D at five azimuths. This choice represents two extremes

of source positions relative to a structure and may give us a reasonable idea of what to expect in amplitude and waveform variation as test sites move within the mesa.

We put pP into the Kirchhoff-Helmholtz synthetics by convolving these synthetics with a boxcar function of unit height and a width corresponding to the pP - P lag time. This convolution yields the impulse response of P and pP if the incident source is a modified Haskell function rather than its time derivative. We justify this simple model of pP by assuming that the reflection coefficient of this phase is -1 . Lay et al. (1983a) estimates the reflection coefficient as $.96$ for pP . We further argue that pP interacts with the same part of the surface as does P . This assumption is good for the shallow depths of the mesa tests which range from $.5$ to 1.4 kilometers. The width of the boxcar is $.85$ seconds; this estimate of the pP - P lag time is taken from Lay et al. (1983). A short period instrument and a Futterman Q operator is also convolved into these synthetics. We use a Haskell function with parameters ($B = 2, K = 10$) while Lay et al. (1983a) use slightly different values ($B = 1, K = 8$).

Figure 14 displays the results of the convolutions. The first column contains the initial Kirchhoff-Helmholtz synthetics with peak amplitudes taken from Figure 10. The second column show these synthetics convolved with a WWSSN short period instrument and a boxcar. We introduce additional complexity into the waveform but do not change the range of peak amplitudes significantly when we include an instrument and pP . The complexity of the waveform caused by structure is masked by the dominant interference between P and pP .

We next convolve these synthetics with Futterman Q operators with a t^* of $.5$ and 1 . The waveforms and their ab amplitudes are displayed in columns 3 and

4. The ab amplitudes are plotted as function of azimuth for both sources and t^* values in Figure 15. We remove the complexity of the waveform for both sources with the two t^* values. However there are some observable differences in the first and third peaks of the waveforms as a function of azimuth. The first peak widens as azimuth increases. The third peak becomes smaller and disappears altogether. Moreover, Figure 15 shows a variation of ab amplitudes with azimuth of $2\frac{1}{2}$ for source D if t^* is .5. However, when t^* is 1, this variation reduces to a factor of 1.7. We also obtain a variation of $2\frac{1}{2}$ of ab amplitudes with respect to source position if t^* is .5. This occurs at $\theta = 0^\circ$ and $\theta = 45^\circ$; however the difference between ab amplitudes for the two sources decreases as the azimuth increases.

Thus we cannot predict the observed ab amplitude variation with azimuth or station location if we use a structure on the Moho 10 kilometers high and approximately 25 kilometers wide. If the factors of 12 or 40, seen in Figures 3, 4, and 5, are measures of a purely near-source phenomena, then one requires a structure several hundred kilometers in scale on a boundary to match these factors. This structure would distort the waveform considerably. Yet there is no obvious evidence in the observed seismograms for a correlation between low amplitudes and complicated and/or broadened waveforms or high amplitudes and simple, impulsive waveforms. We speculate that, rather than a large structure on a single boundary, a small velocity or density perturbation along a several hundred kilometer ray path may produce the desired amplitude change. However we cannot test this speculation with our method.

On the other hand, we predict a factor of $2\frac{1}{2}$ in ab variation with source location if t^* is .5. This variation is not accompanied by any significant

waveform distortion. Although we only produce a factor of $2\frac{1}{2}$ at two azimuths, this is an artifact of the source moveout across the structure. If sources were uniformly distributed over the structure, we would cause this same magnitude of variation at all the azimuths. Furthermore, no source would be systematically higher in ab amplitudes than another source at all the azimuths. Unfortunately Figure 3 does not show systematics with respect to source location. The data should be examined for such trends.

Also the travel time residuals do not correlate with the ab patterns. The convolution with two t^* values demonstrates the frequency dependence of the phenomena. If t^* is larger than 1, we will produce a flat pattern of ab amplitudes with azimuth but the travel time residuals will not change. Thus we do not expect a systematic relationship between travel time and amplitude anomalies because the ab amplitudes are sensitive to Q but the travel times are relatively stable. This is an unfortunate result because such a correlation would be diagnostic of structure as opposed to tectonic release. As yet, there has been no study which definitively demonstrates a relationship. In addition the data sets of amplitude and travel time measurements do not have a one-to-one correspondence. Lay et al. (1983a) measure the ab amplitudes off of short period WWSSN instruments while Minster et al. (1981) and Spence (1974) use culled travel time measurements from the ISC catalogs. We clearly need a study which compares the travel time and amplitude from the same seismogram.

The largest overall variation in ab amplitude with azimuth in Figure 15 occurs because of differences in t^* values. Yet there are no noticeable changes in the waveform. Thus the ab amplitudes are far more sensitive than waveforms to Q differences. Perhaps, a lateral variation of Q with path can produce the

extreme scatter of ab amplitudes for both tests inside and outside the mesa. However it cannot explain the differences in patterns between these different test site areas. If the near-mesa anomalies are, indeed, at least a factor of 10, then structure on the Moho which is compatible with travel time residuals cannot produce these large variations of amplitude with azimuth. However such a structure could explain the observed variation of ab amplitudes with source position at a given station.

References

- Aki, K. and Y.-B. Tsai (1972), "Mechanism of Love-wave excitation by explosive sources", *J. Geophys. Res.*, 77, 1452-1475.
- Butler, R. (1984), "Azimuth, Energy, Q and Temperatures: Variation on P wave amplitudes in the United States", *Review of Geophysics and Space Physics*, 22, 1-36.
- Haddon, R. and P. Buchen (1981), "Use of the Kirchhoff's formula for body wave calculations in the Earth", *Geophys. J. R. astr. Soc.*, 67, 587-599.
- Hilterman, F. (1975), "Amplitudes of seismic waves - A quick look", *Geophys.*, 40, 745-762.
- Hong, T. L. (1978), *Elastic Wave Propagation in Irregular Structures*, (Thesis, California Institute of Technology).
- Langston, C. and D. V. Helmberger (1975), "A procedure for modelling shallow dislocation sources", *Geophys. J. R. astr. Soc.*, 42, 117-130.
- Langston, C. (1977), "The effect of planar dipping structure on source and receiver responses for constant ray parameter", *Bull. Seism. Soc. Am.*, 67, 1029-1050.
- Lay, T., T. C. Wallace, and D. V. Helmberger (1983a), "The effects of tectonic release on short-period P waves from NTS explosions", *Bull. Seism. Soc. Am.*, 74, 819-842.
- Lay, T., L. J. Burdick, D. V. Helmberger, and C. G. Arvesen (1983b), "Estimating seismic yield and defining distinct test sites using complete waveform information", Woodward-Clyde Report, WCCP-R-84-01.
- Minster, J. B., J. M. Savino, W. L. Rodi, T. H. Jordan, and J. F. Masso (1981), "Three-Dimensional velocity structure of the crust and upper mantle beneath the Nevada test site", Systems, Science, and Software Report, SSS-R-81-5138.
- Nuttli, O. W. (1969), "Travel times and amplitudes of S waves from nuclear explosions in Nevada", *Bull. Seism. Soc. Am.*, 59, 385-398.
- Scott, P., and D. V. Helmberger (1983), "Applications of the Kirchhoff-Helmholtz integral to problems in seismology", *Geophys. J. R. astr. Soc.*, 72, 237-254.
- Spence, W. (1974), "P-wave residual differences and inferences on an upper mantle source for the Silent Canyon volcanic centre, Southern Great Basin, Nevada", *Geophys. J. R. astr. Soc.*, 38, 505-523.
- Stratton, J. A. (1941), *Electromagnetic Theory*, First Edition, McGraw-Hill Book Company, Inc., New York
- Wallace, T. C., D. V. Helmberger, and G. R. Engen (1983), "Evidence of tectonic release from underground nuclear explosions in long-period P waves",

Bull. Seism. Soc. Am., 73, 593-813.

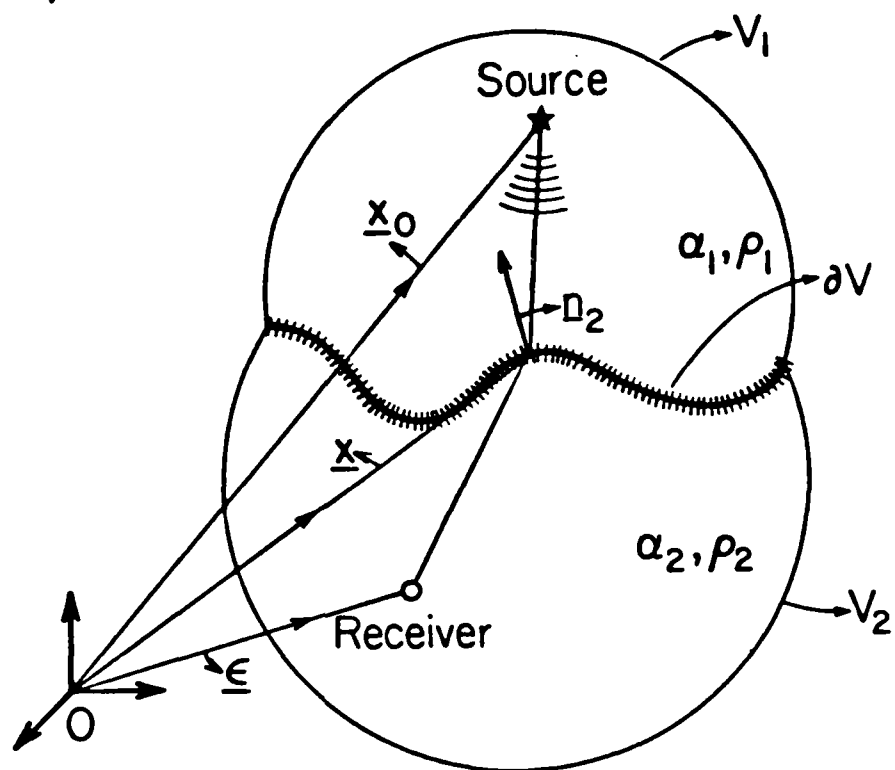
Figure Captions

- 1a. The geometry of the Kirchhoff-Helmholtz calculations for transmission across two acoustic media with sound speeds α_1 and α_2 and densities ρ_1 and ρ_2 . The source is in V_1 at \underline{x}_0 and the receiver is in V_2 at \underline{x} .
- 1b. A close up of a piece of the boundary which displays the angles.
- 2a. Two synthetics and the grid geometry used to compute them. Synthetic A is contaminated by a truncation phase which originates from the edge of the grid. Synthetic B is contaminated by a phase which originates from the abrupt change in boundary conditions. The grid next to synthetic B is gray when $\varphi = 0$ on the boundary.
- 2b. A comparison between Kirchhoff-Helmholtz and first motion solutions. The input source is the first derivative of a modified Haskell function with parameters ($B=2, K=10$). The maximum dimensionless amplitude of the source input function is 45.1 .
3. The short period P wave ab amplitude data set for 25 Pahute Mesa events plotted as a function of station location. The amplitudes are corrected for event size, geometric spreading and instrument gain at 1 second and are plotted relative to a master event (from Lay et al., 1983a).
4. The relative ab amplitudes of GREELEY and FAULTLESS as a function of station location (from Lay et al., 1983a).
5. Ratios of relative ab amplitudes of FAULTLESS, PILEDRIIVER, and BILBY divided by the average relative ab amplitudes of the mesa events (from Lay et al., 1983b).
6. Seismograms from FAULTLESS (top record) and GREELEY (bottom record) displayed in order of increasing azimuth in the range of 30° to 100° . Also shown are the absolute ab amplitudes in millimicrons, corrected only for instrument gain at 1 second.
7. Transmitted potentials from sources 35 kilometers above the center of the structure. The cross sections of the structures upwarp, exponential, plug and sinc are above the synthetics. For comparison potentials which propagate through a flat boundary are shown in the first column. The potentials are from receivers which are 20,000 kilometers below the source and which vary from 0 to 7000 kilometers horizontally away from the source. All amplitudes are

multiplied by .01.

8. Travel time contours for a source 35 kilometers directly above the structure and receivers 20,000 kilometers directly below the source. The four structures are a) a plane, b) an upwarp, c) a plug, and d) a sinc function. The contours are projected onto the topographies and flat grids. The synthetics which correspond to each travel time projection are in between the two projections. The contour interval is .125 seconds as are the tick marks of the synthetics. The geometric arrival time is the center of the contours.
9. Plots of peak amplitudes, amplitudes of first pulses, and travel time residuals as a function of distance from synthetics in Figure 7. The different symbols correspond to different topographies and are at the bottom of the figure. Where first pulse amplitudes are different from peak amplitudes, the values of first pulse amplitudes are plotted with open symbols and the peak amplitudes are plotted with closed symbols. The dotted line corresponds to the peak amplitudes from synthetics which propagate through a planar interface.
10. Synthetics from the topography upwarp calculated for four source positions, five azimuths and seven distances. The topography map and cross section with source positions are in the center. The contour interval is 1 kilometer. The distances, angles, and azimuths of the receivers are also shown.
11. Travel time residuals for source locations A, B, C, and D plotted as a function of azimuth and distance.
12. Peak amplitudes for source locations A, B, C, and D plotted as a function of azimuth and distance.
13. Amplitudes of the first pulse for source locations A, B, C, and D plotted as a function of azimuth and distance.
14. Kirchhoff-Helmholtz responses (first column) convolved with a boxcar of width .85 seconds and a short period WWSSN instrument (second column) and a Q operator with t^* values of .5 (third column) and 1 (fourth column). Responses are from a distance of 4000 kilometers, azimuth range of 0° to 180° and source locations A and D.
15. ab amplitudes from synthetics in Figure 14 plotted as a function of azimuth for both source locations A and D and both t^* values.

a)



b)

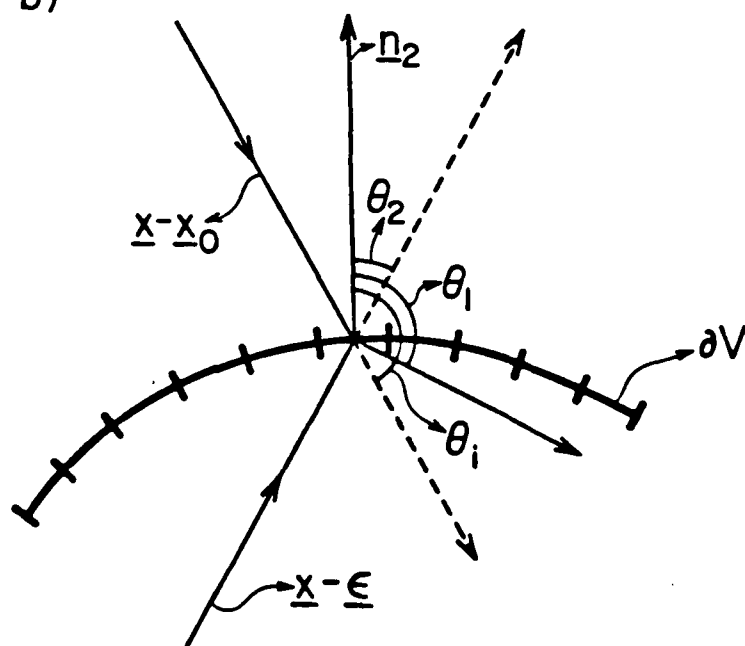


Fig 1

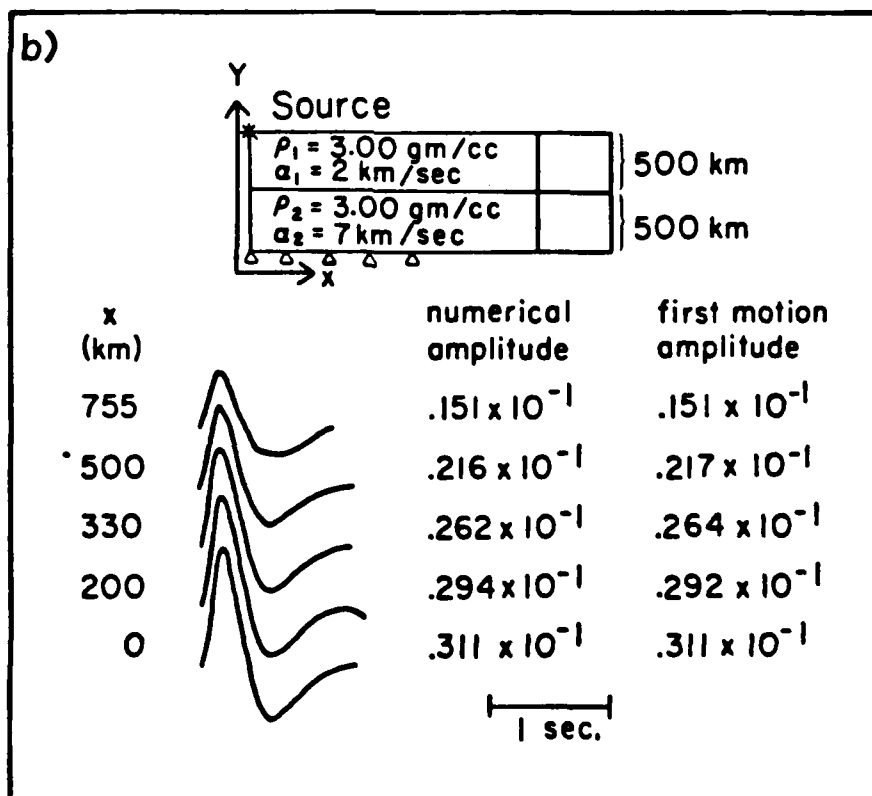
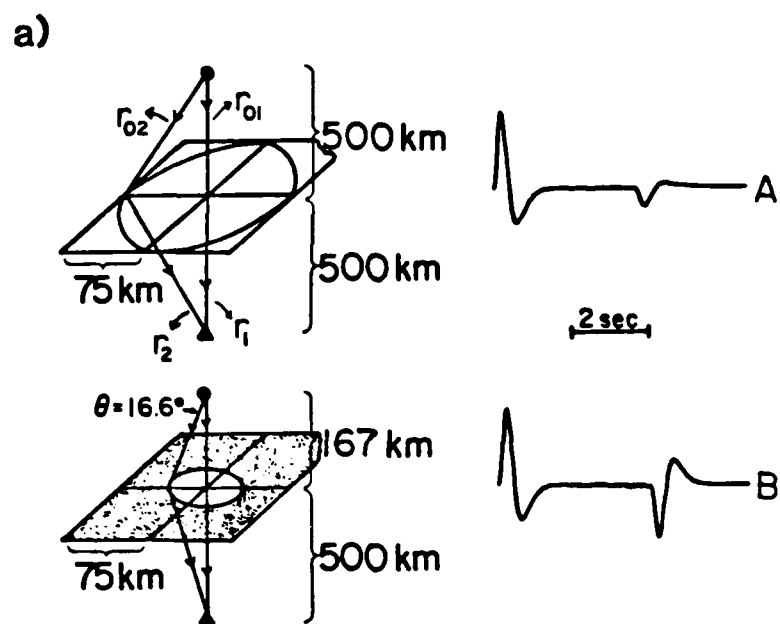


Fig 2

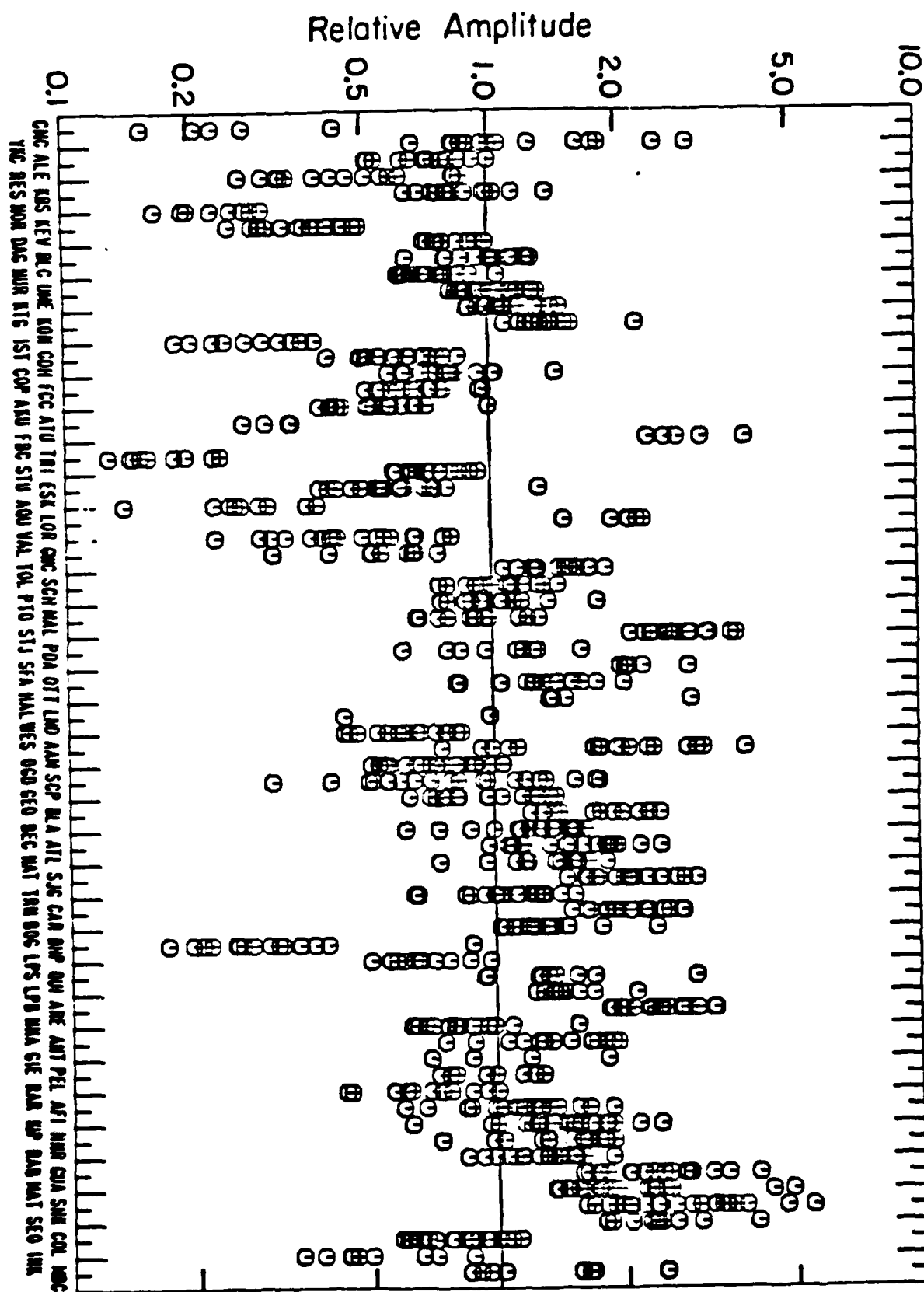


Fig 3

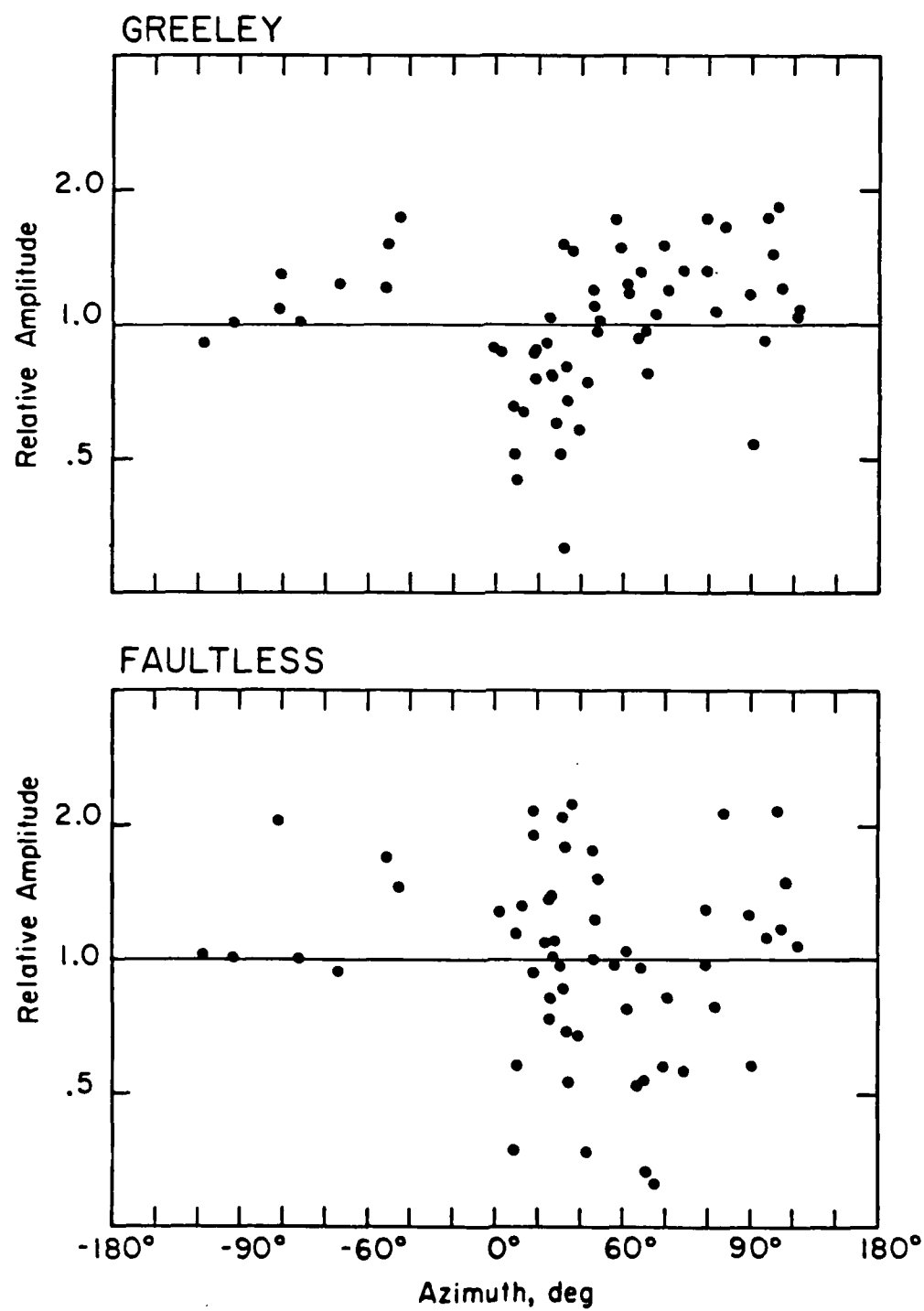


Fig. 4

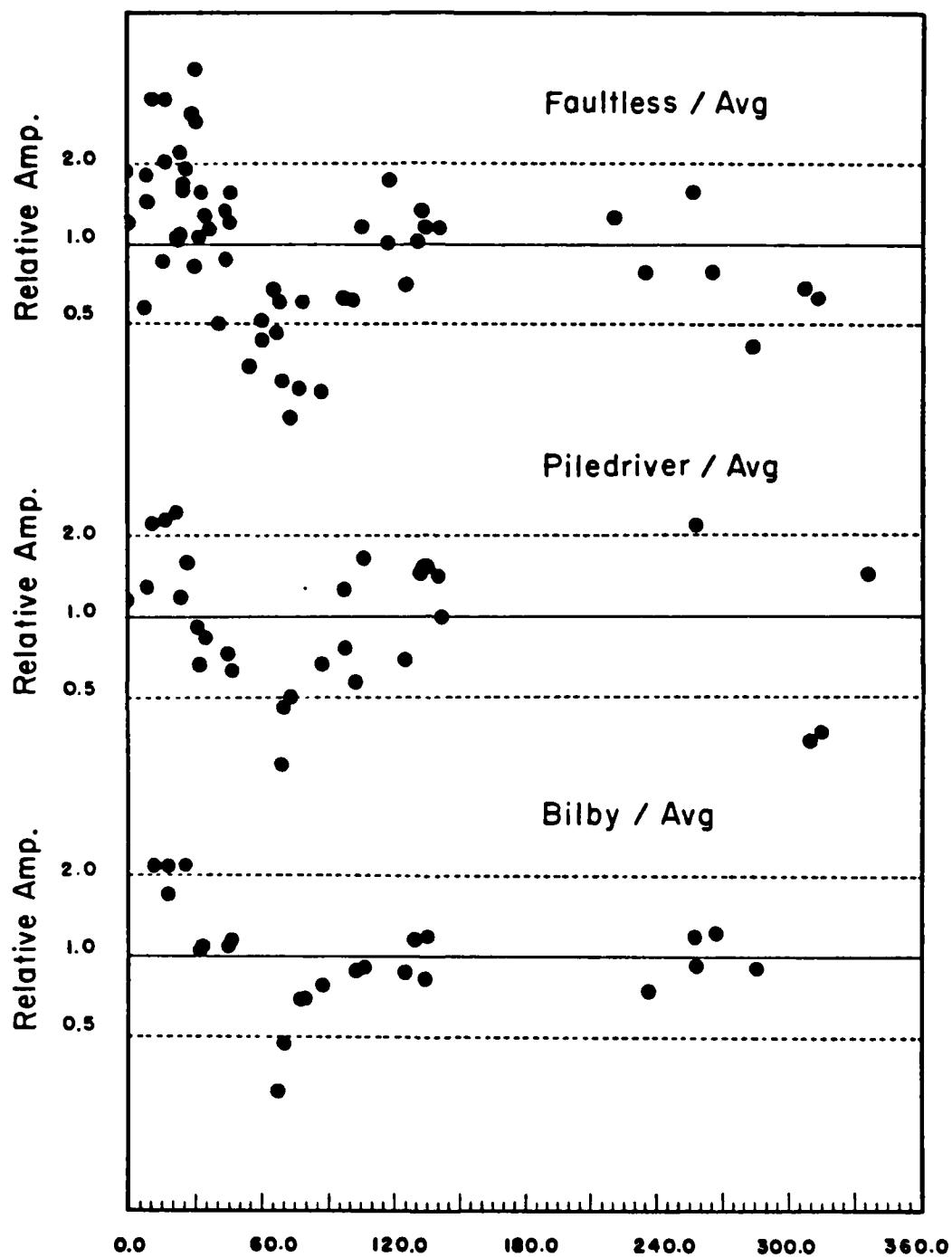


Fig. 5

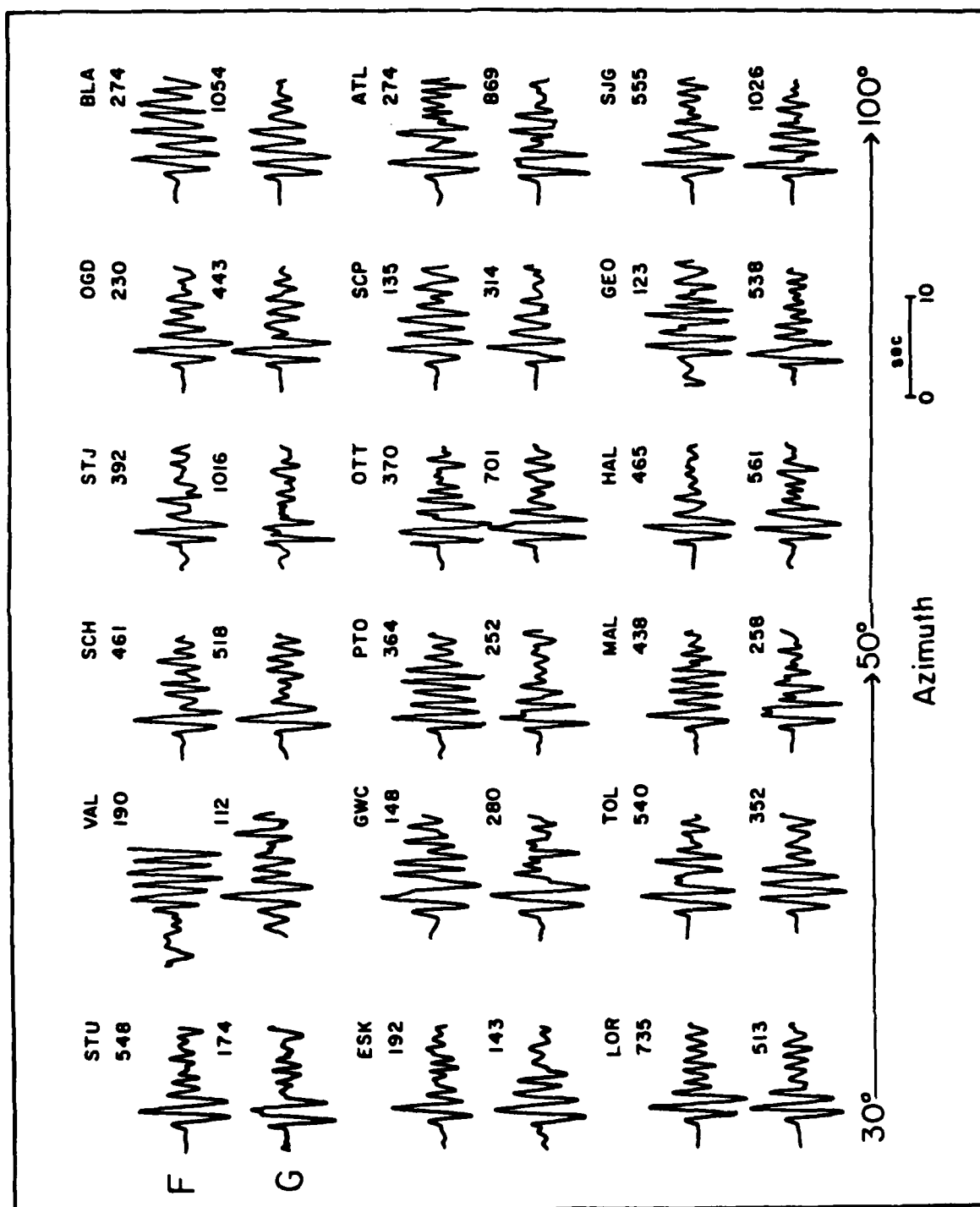


Fig. 6

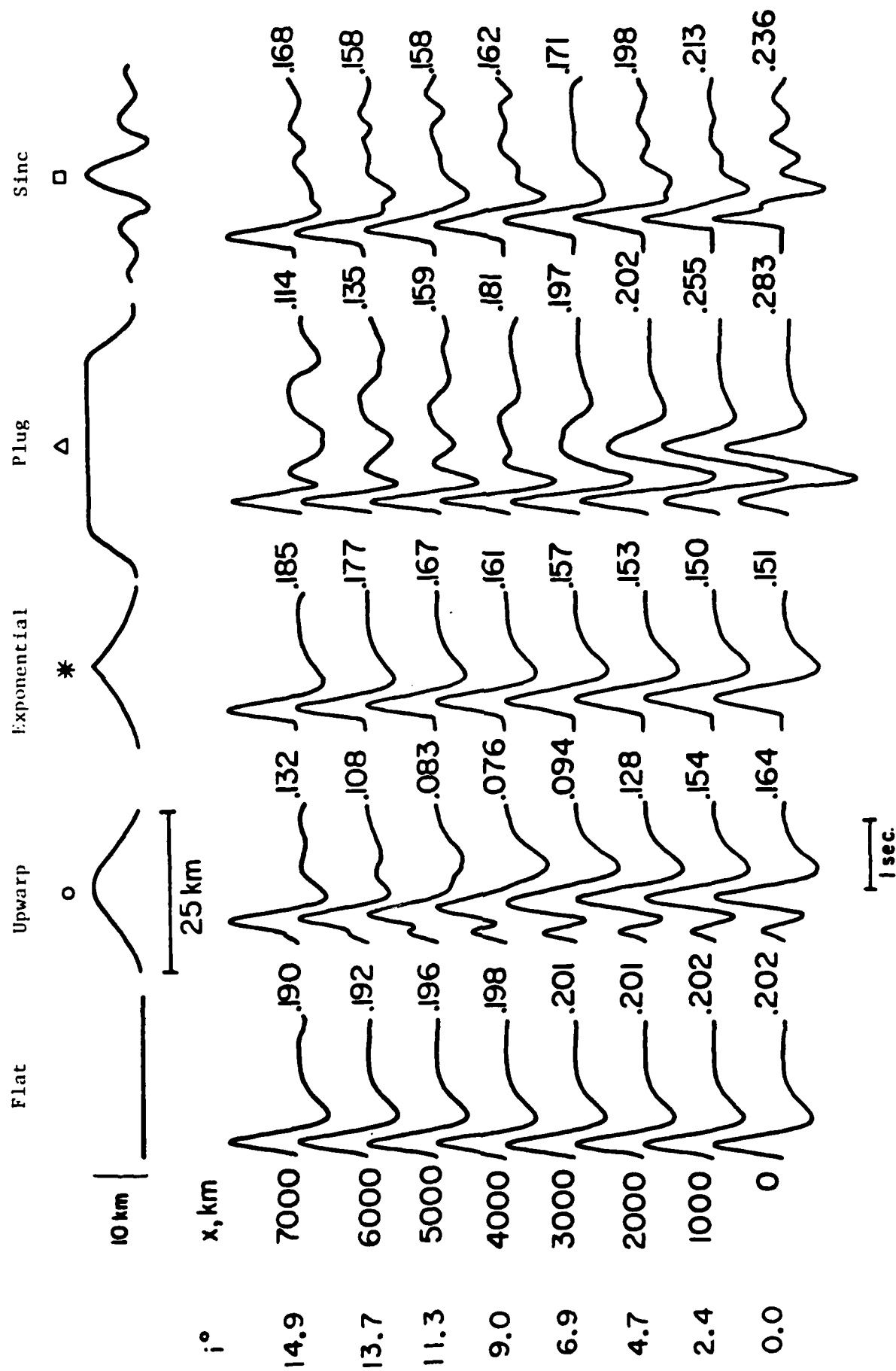


Fig. 7

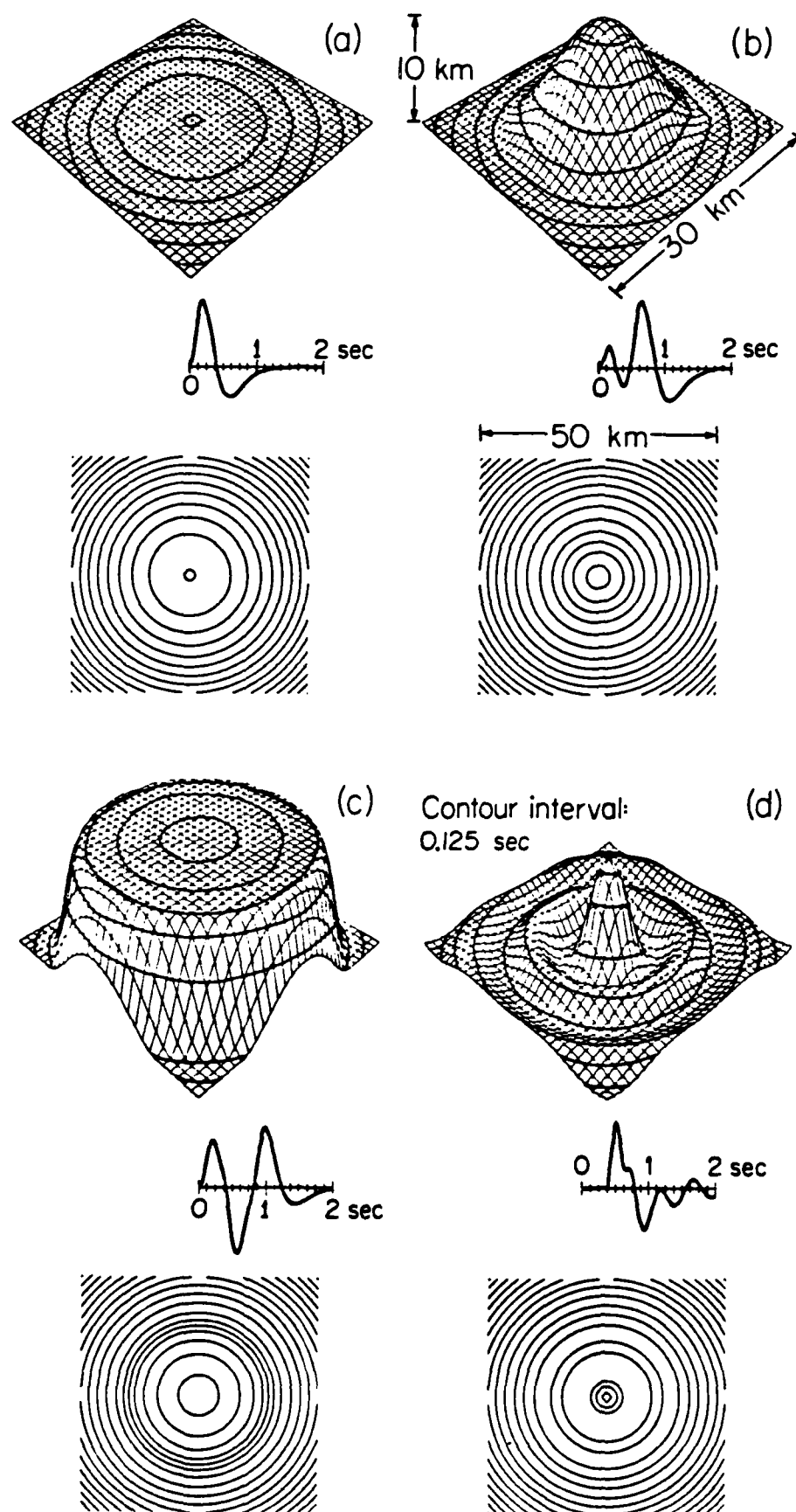


Fig. 8

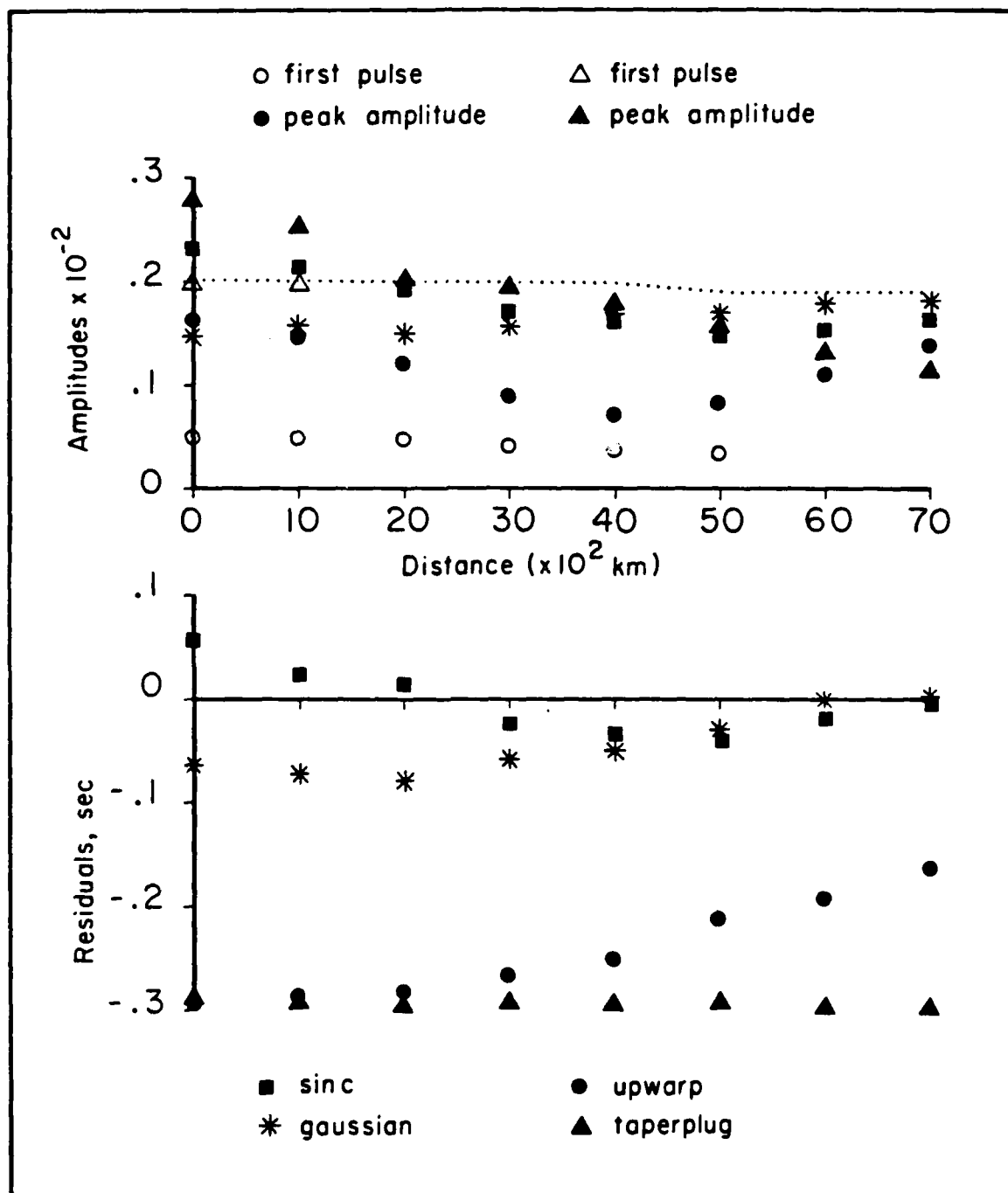


Fig 9

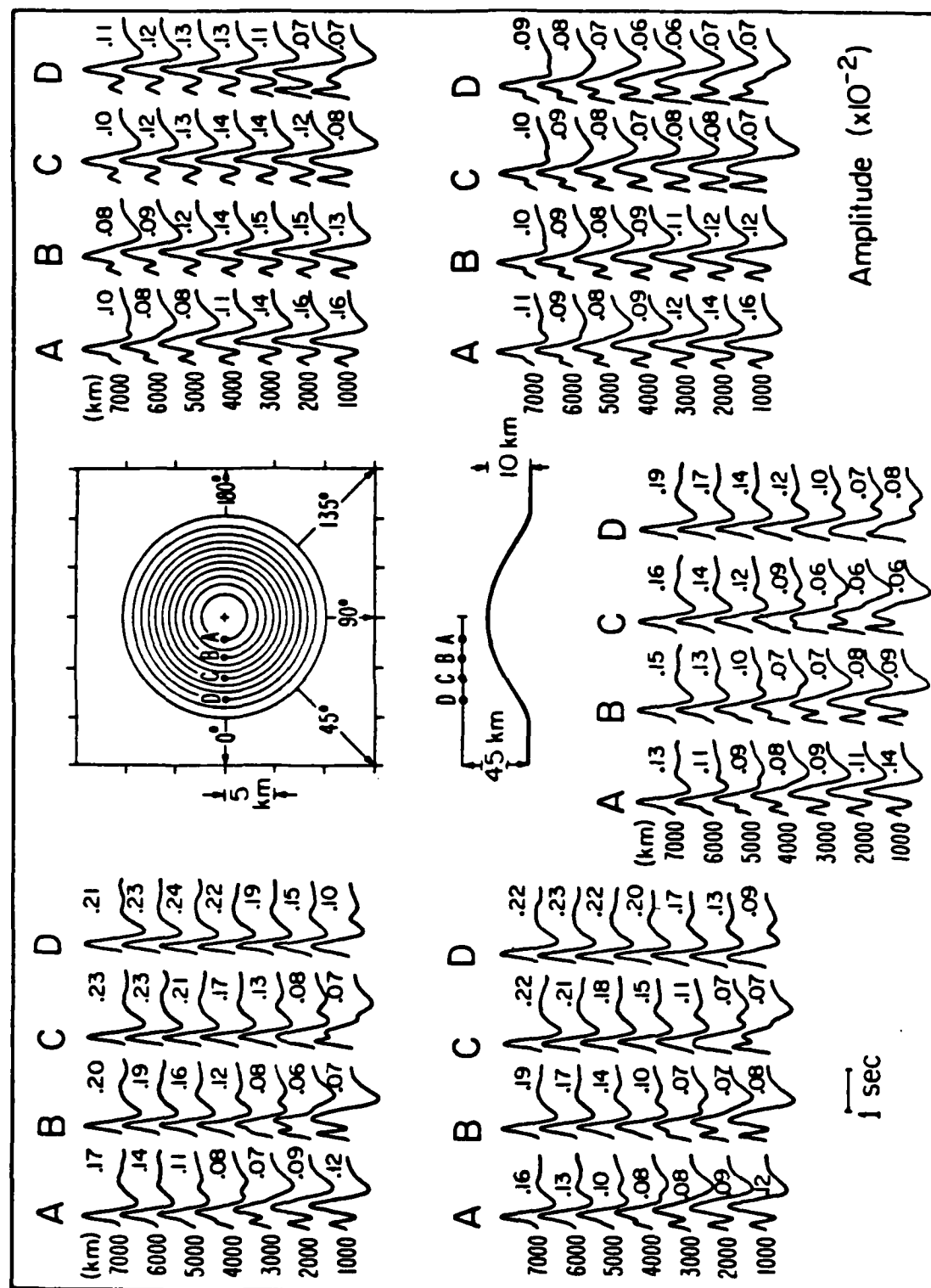


Fig. 10

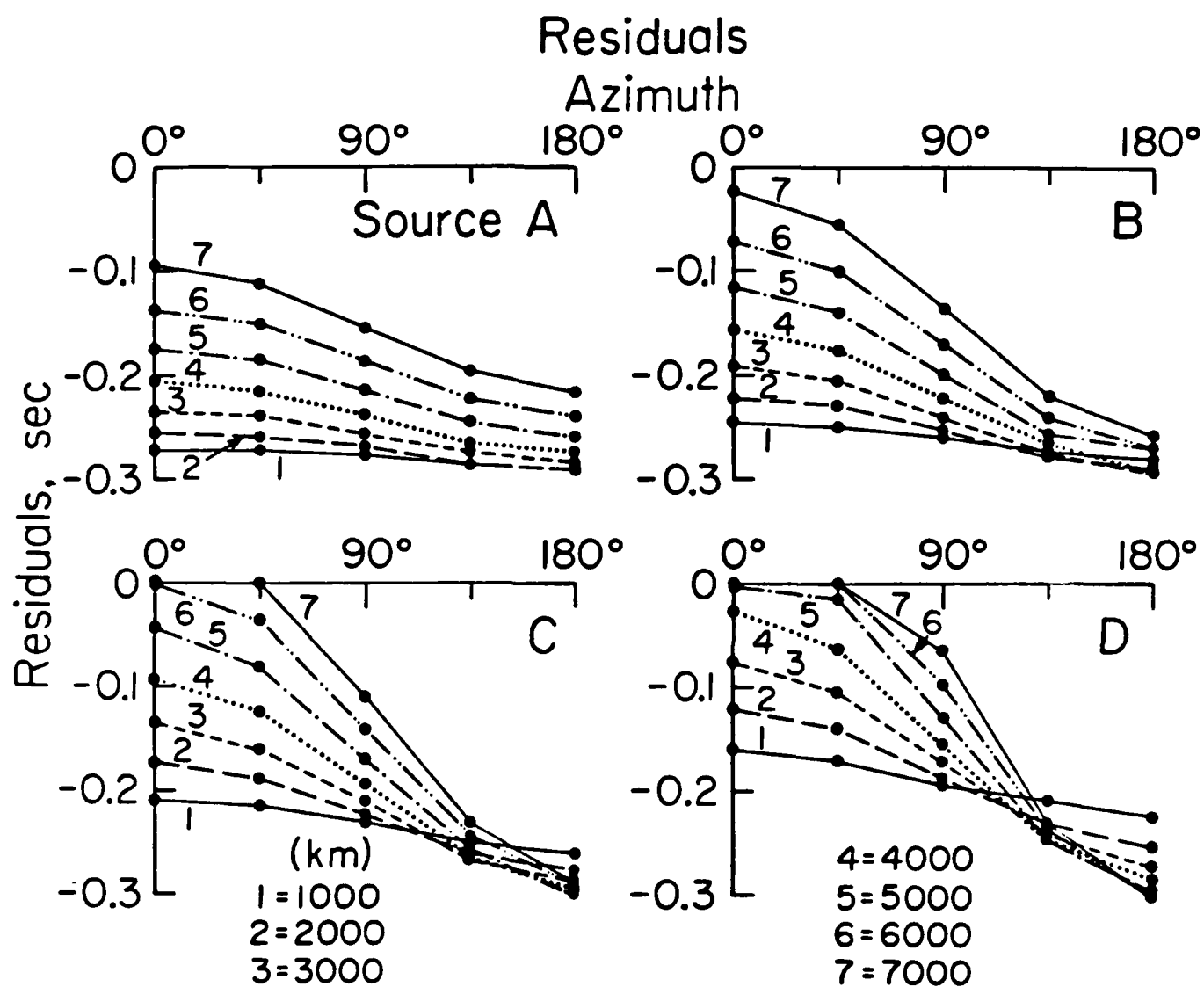


Fig. 11

Amplitudes of First Arrival

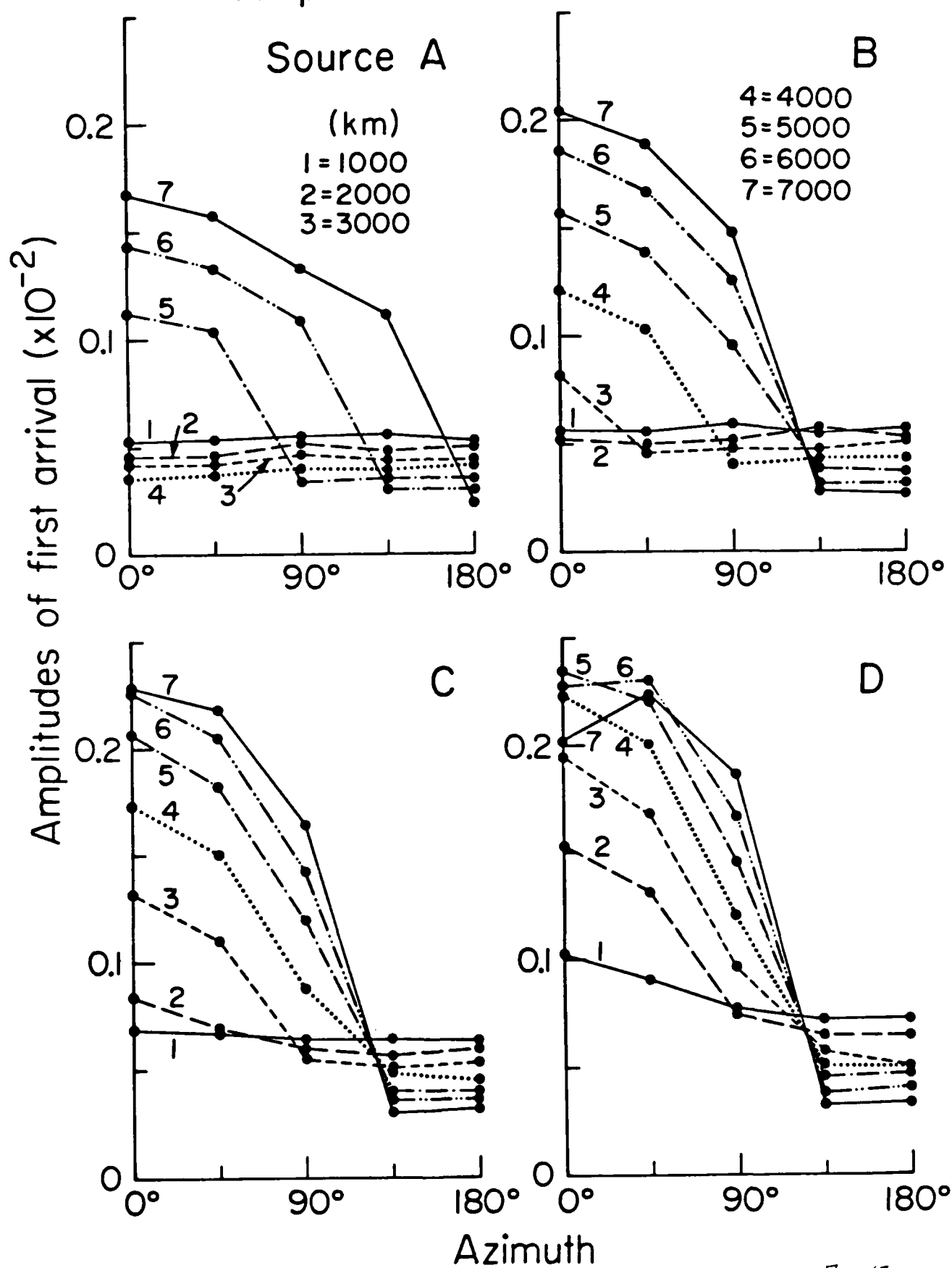


Fig 13

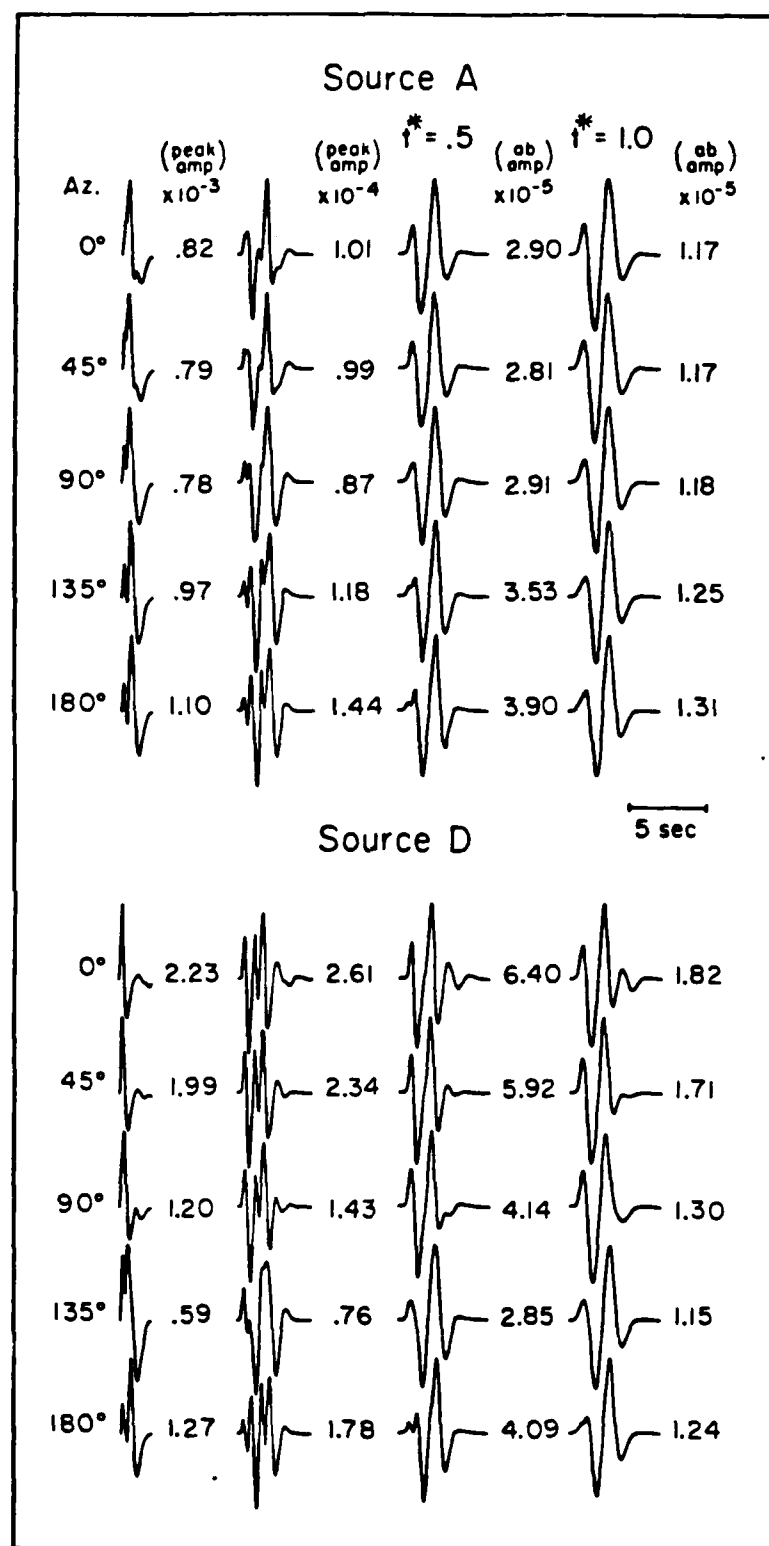


Fig. 14

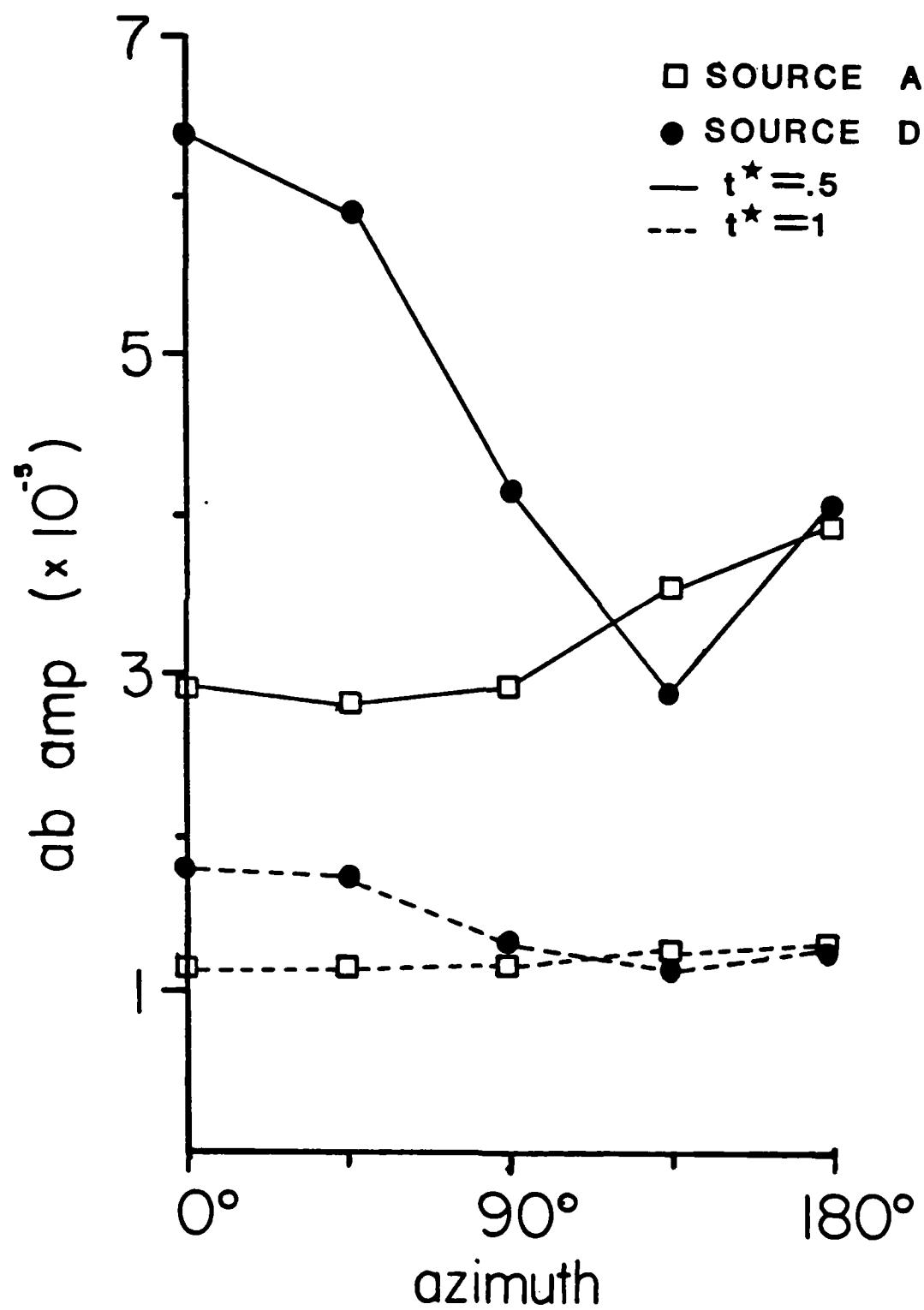


Fig. 15

REPORT DOCUMENTATION PAGE

1a. REPORT SECURITY CLASSIFICATION		1b. RESTRICTIVE MARKINGS	
2a. SECURITY CLASSIFICATION AUTHORITY		3. DISTRIBUTION/AVAILABILITY OF REPORT Seismological Laboratory California Institute of Technology Pasadena, CA 91125	
2b. DECLASSIFICATION/DOWNGRADING SCHEDULE		5. MONITORING ORGANIZATION REPORT NUMBER(S)	
4. PERFORMING ORGANIZATION REPORT NUMBER(S) N00014-76-C-1070		7a. NAME OF MONITORING ORGANIZATION Office of Naval Research Resident Representative	
6a. NAME OF PERFORMING ORGANIZATION California Institute of Technology	6b. OFFICE SYMBOL (If applicable)	7b. ADDRESS (City, State and ZIP Code) 1030 E. Green St. Pasadena, CA 91106	
8a. NAME OF FUNDING/SPONSORING ORGANIZATION Office of Naval Research	8b. OFFICE SYMBOL (If applicable)	9. PROCUREMENT INSTRUMENT IDENTIFICATION NUMBER NR 083-399	
8c. ADDRESS (City, State and ZIP Code) 800 N. Quincy St. Arlington, VA 22217		10. SOURCE OF FUNDING NOS.	
11. TITLE (Include Security Classification) Detailed Oceanic Crustal Modeling		PROGRAM ELEMENT NO.	PROJECT NO.
12. PERSONAL AUTHOR(S) Dr. D. V. Helmlberger		TASK NO.	WORK UNIT NO.
13a. TYPE OF REPORT Final Report	13b. TIME COVERED FROM 2/1/81 TO 5/31/84	14. DATE OF REPORT (Yr., Mo., Day) 1984 November 7	
15. PAGE COUNT			
16. SUPPLEMENTARY NOTATION			
17. COSATI CODES		18. SUBJECT TERMS (Continue on reverse if necessary and identify by block number)	
FIELD	GROUP	SUB. GR.	
19. ABSTRACT (Continue on reverse if necessary and identify by block number)			
<p>The research performed under this contract can be divided into 3 main topics: changes in existing methods, Cagniard de-Hoop and WKBJ, which enable construction of synthetics for mixed path situations; use of long period SH waves with source in the Northwest Atlantic and receivers on the northeast coast of North America to derive an oceanic upper mantle shear velocity model; and a technique based on evaluating the Kirchhoff-Helmholtz integral for predicting the effect of near source or near receiver structure complexity on far field p waves.</p> <p>In Section II we assess the fact that recent models of upper mantle structure based on long period body waves (WWSSN) suggest large horizontal gradients, especially in shear velocities. Some changes in existing methods</p>			
20. DISTRIBUTION/AVAILABILITY OF ABSTRACT UNCLASSIFIED/UNLIMITED <input type="checkbox"/> SAME AS RPT <input type="checkbox"/> DTIC USERS <input type="checkbox"/>		21. ABSTRACT SECURITY CLASSIFICATION	
22. NAME OF RESPONSIBLE INDIVIDUAL Dr. D. V. Helmlberger		22b. TELEPHONE NUMBER (Include Area Code) (818) 356-6998	22c. OFFICE SYMBOL

are required to construct synthetics for mixed path situations. This is accomplished by allowing locally dipping structure and making some modifications to generalized ray theory. Local ray parameters are expressed in terms of a global reference which allows a de-Hoop contour to be constructed for each generalized ray with the usual application of the Cagniard de-Hoop technique. Several useful approximations of ray expansions and WKBJ theory are presented. Comparisons of the synthetics produced by these two basic techniques with known solutions demonstrates their reliability and limitations.

In Section III, we have modeled the SH motion from earthquakes in the northwest Atlantic ocean to derive an oceanic upper mantle shear velocity model. The signals were recorded on long-period WWSSN and Canadian network stations on the east coast of North America. This data indicates a fast (4.75 km/sec) lid of about 100 km thickness in the older western Atlantic. Given the lid structure, the waveforms and traveltimes from the more distant data put tight constraints on the shear velocities at greater depths. The velocity below 200 km was found to be indistinguishable from a model of the East Pacific Rise (Grand and HelMBERGER, 1983) found using the same technique. We find the Canadian shield to be faster than both the old northwestern Atlantic and the young East Pacific Rise to about 400 km depth. No variations below 400 km are necessary to explain the data.

In Section IV, we extend the Kirchhoff-Helmholtz integral method to calculate acoustic potentials which transmit through three dimensional warped boundaries. We specify the potentials on an arbitrary surface with Snell's law and plane-wave transmission coefficients and numerically integrate their contributions at a receiver via the scalar integral representation theorem. The method is appropriate for modeling precritical transmitted potentials. Results from test models compare well with optical solutions for transmissions through a flat interface.

END

FILMED

1-85

DTIC